The evolution of dark halo substructure

by

Stuart P. D. Gill

A Dissertation
Presented in fulfillment of the requirements
for the degree of
Doctor of Philosophy
at Swinburne University Of Technology

July 2005

Abstract

In this dissertation we analyse the dark matter substructure dynamics within a series of high-resolution cosmological galaxy clusters simulations generated with the N-body code `MLAPM`.

Two new halo finding algorithms were designed to aid in this analysis. The first of these was the "`MLAPM`-halo-finder" (`MHF`), built upon the adaptive grid structure of `MLAPM`. The second was the "`MLAPM`-halo-tracker" (`MHT`), an extension of `MHF` which allowed the tracking of orbital characteristics of gravitationally bound objects through any given cosmological N-body-simulation. Using these codes we followed the time evolution of hundreds of satellite galaxies within the simulated clusters.

These clusters were chosen to sample a variety of formation histories, ages, and triaxialities; despite their obvious differences, we find striking similarities within the associated substructure populations. Namely, the radial distribution of these substructure satellites follows a "universal" radial distribution irrespective of the host halo's environment and formation history. Further, this universal substructure profile is anti-biased with respect to the underlying dark matter profile. All satellite orbits follow nearly the same eccentricity distribution with a correlation between eccentricity and pericentre. The destruction rate of the substructure population is nearly independent of the mass, age, and triaxiality of the host halo. There are, however, subtle differences in the velocity anisotropy of the satellite distribution. We find that the local velocity bias at all radii is greater than unity for all halos and this increases as we move closer to the halo centre, where it varies from 1.1 to 1.4. For the global velocity bias we find a small but slightly positive bias, although when we restrict the global velocity bias calculation to satellites that have had at least one orbit, the bias is essentially removed.

Following this general analysis we focused on three specific questions regarding the evolution of substructures within dark matter halos.

Observations of the Virgo and Coma clusters have shown that their galaxies align

with the principal axis of the cluster. Further, a recent statistical analysis of some 300 Abell clusters confirm this alignment, linking it to the dynamical state of the cluster. Within our simulations the apocentres of the satellite orbits are preferentially found within a cone of opening angle $\sim 40^\circ$ around the major axis of the host halo, in accordance with the observed anisotropy found in galaxy clusters. We do, however, note that a link to the dynamical age of the cluster is not well established. Further analysis connects this distribution to the infall pattern of satellites along the filaments, rather than some "dynamical selection" during their life within the host's virial radius.

We then focused our attention on the outskirts of clusters investigating the so-called "backsplash population", i.e. satellite galaxies that once were inside the virial radius of the host but now reside beyond it. We find that this population is significant in number and needs to be appreciated when interpreting empirical galaxy morphology-environmental relationships and decoupling the degeneracy between nature and nurture. Specifically, we find that approximately half of the galaxies with current clustercentric distance in the interval $1 - 2$ virial radii of the host are backsplash galaxies which once penetrated deep into the cluster potential, with 90% of these entering to within 50% of the virial radius. These galaxies have undergone significant tidal disruption, losing on average 40% of their mass. This results in a mass function for the backsplash population different to those galaxies infalling for the first time. We further show that these two populations are kinematically distinct and should be observable spectroscopically.

Finally we present a detailed study of the real and integrals-of-motion space distributions of a disrupting satellite obtained from one of our self-consistent high-resolution cosmological simulations. The satellite has been re-simulated using various analytical halo potentials and we find that its debris appears as a coherent structure in integrals-of-motion space in all models ("live" and analytical potential) although the distribution is significantly smeared for the live host halo. The primary mechanism for the dispersion is the mass growth of the host. However, when quantitatively comparing the effects of "live" and time-varying host potentials we conclude that not all of the dispersion can be accounted for by the steady growth of the host's mass. We ascribe the remaining differences to additional effects in the "live" halo such as non-sphericity of the host and interactions with other satellites, which have not been modelled analytically.

Acknowledgements

I would like to thank my supervisors Brad Gibson and Alexander Knebe, for their inspirational energy and encouragement, guidance and genuine care. I appreciate the freedom and trust you have given me, and your generosity of spirit. I feel blessed to have been your student.

Thanks to Nicki, my darling wife. I am a better man because of you. Thank you for your love and support, for putting up with all my travel, and for watching me sleep in while you had to go to work.

To the Gill family. Mum and Dad, you have been such a beautiful selfless example; thankyou for all your support over the years. To my brother Peter. Thank you for your friendship and honesty. To my sister Natasha, my brother-in-law Rob, my nephew Josh, and the newest addition that I just found out about and am meant to keep secret ;) Nicki and I are so thankful for your love and care as a family.

There are also so many close friends to thank; Chris Brook, Craig West, Adam & Naomi, Darren & Emily, Mike & Brea, Ray Harris and all the Space Generation crew. Thank you all for providing a plethora of things to keep me distracted throughout my PhD, and for many good times.

Thnks to the following people who have been a great support to me in my research; Paul Bourke, Chris Brook, Craig West, Andrew Jameson, Chris Fluke, Willem van Straten, Chris Power, Rodrigo Ibata, Daisuke Kawata, Fabio Governato, James Murray, Tim Connors and Mike Beasley. Also James Binney, Mike Dopita, Geraint Lewis, Erica Ellingson, Bernard Vollmer, Michael Balogh, Gary Mamon and Janne Holopainen.

I would also like to extend a big thank you to everybody at the Swinburne Centre for Astrophysics and Supercomputing for assisting me whenever I was in need and in particular the administration staff at the centre; Liz, Asha, Michelle and Vicki.

I am grateful to the Department of Education and Science for their financial assistance in the form of an Australian Postgraduate Award, and to the Pratt foundation for the Richard Pratt Fellowship. Thanks also to the Astronomical Society of Australia, and especially to the Apple University Consortium who provided computer equipment and supported my attendance at the Apple WWDC.

Most importantly I would like to thank my Lord and saviour, for the peace and knowledge of His love throughout this time.

Declaration

This thesis contains no material that has been accepted for the award of any other degree or diploma. To the best of my knowledge, this thesis contains no material previously published or written by another author, except where due reference is made in the text of the thesis.

Science is a collaborative pursuit, and the studies presented in this thesis are very much part of a team effort. The collaborators listed below have great experience and knowledge, and were all integral in obtaining the presented results.

Chapter 2 was partially published in the following two papers; S.P.D. Gill, A. Knebe, B.K. Gibson, 2004, "The evolution of substructure I: finding the substructure", MNRAS, 351, 399, 2004 and S.P.D. Gill, A. Knebe, B.K. Gibson, "The evolution of substructure II: linking the dynamics to environment", MNRAS, 351, 410, 2004.

Chapter 3 was previously published as S.P.D. Gill, A. Knebe, B.K. Gibson, 2004, "The evolution of substructure I: finding the substructure", MNRAS, 351, 399. Although additional text has been added to update the development halo finder. Further, additional figures have been added to increase claraity.

Chapter 4 was previously published as S.P.D. Gill, A. Knebe, B.K. Gibson, 2004, "The evolution of substructure II: linking the dynamics to environment", MNRAS, 351, 410 and S.P.D. Gill, A. Knebe, B.K. Gibson, 2004, "The dynamics of cluster substructure", IAU Conference Proceedings, 195, 280, 2004.

Chapter 5 was previously published as A. Knebe, S.P.D. Gill, B.K. Gibson, R. Ibata, G. Lewis, 2004, "Anisotropy in satellite distribution", MNRAS, 603, 7. Additional text has been added along with minor restucturing to the body. We also include an update on the field since the publication of this paper.

Chapter 6 was previously published as S.P.D. Gill, A. Knebe, B.K. Gibson, 2005, "The evolution of substructure III: the outskirts of clusters", MNRAS, 356, 1327. The results section has been expanded slightly to include additional figures.

Chapter 7 was previously published as A. Knebe, S.P.D. Gill, D. Kawata, B.K. Gibson, 2004, "Mapping Substructure in Dark Matter Halos", MNRAS, 357, L35.

Some additional text, figures and tables have been added to increase claraity and deepth.

Appendix A was previously published in S.P.D. Gill, A. Knebe, B.K. Gibson, 2004, "The evolution of substructure II: linking the dynamics to environment", MNRAS, 351, 410.

Minor alterations and redistributions have been made to these studies in order to maintain consistency throughout the thesis.

Stuart P. D. Gill

22 July 2005

Contents

List of Figures

List of Tables

"Is this magic? you ask, and I reply with a cry of despair that it is worse, it is science. You who study the star clusters, the galaxies, the planets and their moons, you who treat the earth and date its rocks, you who sift the sand of the desert and plumb the depths of the ocean for the blind creatures living there ... I invite you, I challenge you, to come with me, as Dante went with Virgil, I am your guide to the infernal shambles of human reason, the shattered, unassembleable fractions of consciousness ... the dreck of the real, our wrecked romance with God. This new hell is where our inquiry begins."

E. L. Doctorow - City of God

Chapter 1

Introduction

"It seems to me that if the matter of our sun and planets and all the matter in the Universe were evenly scattered throughout all the heavens, and every particle had an innate gravity towards all the rest... some of it would convene into one mass and some into another, so as to matter an infinite number of great masses, scattered at great distances from one another throughout all that infinite space."

- Newton (1692)

Throughout this thesis we will use numerical simulations to gain a better understanding of (cosmic) structure formation within the Universe. In particular we aim to shed light on unanswered questions concerning the dynamics of cluster galaxies.

1.1 Motivation

Cosmology and Structure Formation

The formation of structure within the Universe is one of the central questions of modern astrophysics. How did the stars, globular clusters, galaxies and clusters come into being and how are they distributed throughout the Universe? As an illustration of such cosmic structures in the top panel of Figure 1.1 we see the distribution of

galaxies from the 2dF Galaxy Redshift Survey (Colless et al. 2001). This positioning of galaxies is clearly not random. Rather, the structure has a spongy/foamy appearance. In this arrangement of galaxies there are regions with very few galaxies (voids), and conversely there are filamentary structures consisting of many galaxies. At the intersection of these filaments we find the largest gravitationally bound objects in the Universe; galaxy clusters, which are collections of hundreds or even thousands of galaxies. One such galaxy cluster Abel 1689 can be seen in the bottom of Figure 1.1.

The creation of structures in the Universe is a complicated process, requiring many carefully measured ingredients, such as the right amount of matter and also the type of matter is it baryonic or non-baryonic? Further, if a portion is non-baryonic what is the nature of that matter? Does it interact? Is it hot, cold or both? What is the geometry of the Universe? At what rate does the Universe expand and does that expansion accelerate? How homogeneous and isotropic is the Universe?

Recently through observation, significant progress has been made in answering many of these questions and providing us with a compelling model for structure formation. Arguably the most notable of these was the discovery of the *cosmic microwave background* (CMB) (Penzias & Wilson 1965; de Bernardis et al. 2000; Stompor et al. 2001; Spergel et al. 2003). The CMB is a remarkably uniform distribution of microwave electromagnetic radiation looking back through the Universe to when it was initially opaque. Imprinted on this uniform distribution are small temperature fluctuations thought to have originated from inhomogeneities in the distribution of matter on the surface of last scattering. From these temperature variations we can place tight constrains on cosmological parameters including the composition and density of the Universe. Further, it is these inhomogeneities that are understood to have seeded structure formation The large galaxy redshift surveys, such as the 2df galaxy redshift survey (Colless et al. 2001; Peacock et al. 2001) and the Sloan Digital Sky Survey (York et al. 2000), have also been very significant, placing complimentary constrain on the model through galaxy-clustering statistics.

The accuracy of these recent observations have allowed the establishment of the so-called cosmological "concordance model". This ΛCDM model consists of Cold Dark Matter (CDM) in a flat, Lambda (Λ) dominated Universe comprised of 28% dark matter, 68% dark energy, and luminous baryonic matter (i.e. galaxies, stars, gas, and dust) at a mere 4% (cf. Spergel et al. 2003).

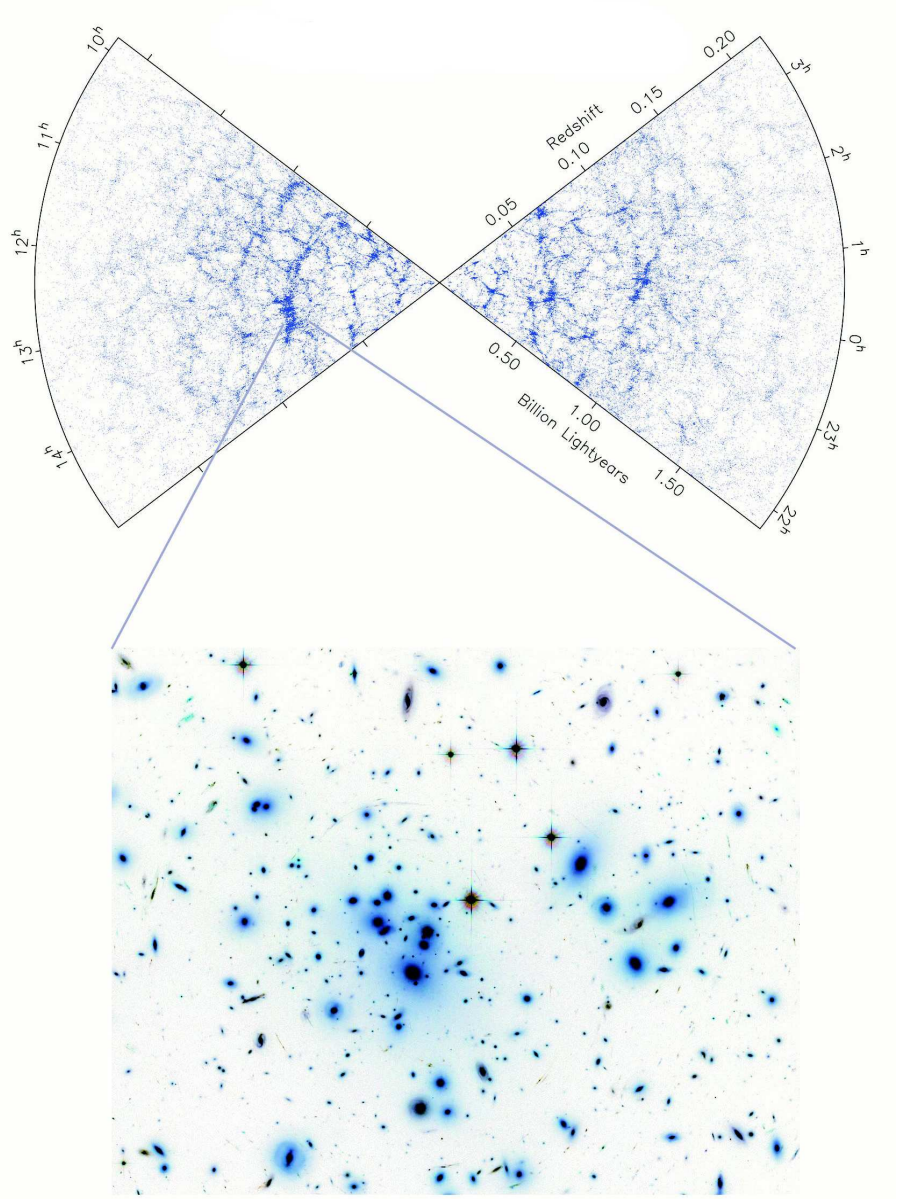

Figure 1.1: Large Scale Structure - Galaxy Clusters

The top image shows a galaxy distribution map from the 2dF Galaxy Redshift Survey (100k galaxy data release) (Colless et al. 2003). In the regions of high galaxy density such as intersecting filaments we find galaxy clusters. The galaxy cluster Abel 1689 taken with the Hubble Space Telescope is an example of a cluster that would be found at such a region. [Note: this is not the correct position of Abel 1689 in the 2dF survey but rather an illustration.]

This ΛCDM model has proven to be consistent with an impressive array of observations, including the age of the oldest stars (e.g. Chaboyer et al. 1998), the extragalactic distance scale as measured by distant Cepheids (e.g. Gibson et al. 2000), the baryonic mass fraction of galaxy clusters (e.g. White et al. 1993) and the luminosity distances of Type Ia supernovae which were used to measure an acceleration of the expanding Universe (Garnavich et al. 1998; Riess et al. 1998).

Within this ΛCDM concordance model we now have a compelling theoretical framework from which we can understand the formation of cosmological structure. Within the otherwise homogeneous and isotropic very early Universe existed small density fluctuations (imprinted during an earlier epoch of inflation and seen in the CMB). The small wavelength density perturbations grew first through gravitational instability. Eventually the gravitational attraction of the material became stronger than the expansion of the Universe, and the surrounding material began to collapse. That collapse eventually led to the formation of gravitationally bound virialised dark matter halos.

These objects further accreted more material and merged together forming progressively larger and larger objects corresponding to larger and larger wavelength perturbations in the primordial density field (White & Reese 1978; Davis et al. 1985). This ordering of structure formation is called hierarchical structure formation because the structure is formed from bottom-up rather than a monolithic collapse of the material i.e. from the top-down, although both bottom-up and top-down structure formation do occur in the Universe.

Galaxies, galaxy clusters (and super clusters) are all understood to have formed hierarchically. For example galaxy clusters are believed to have formed through the accretion of galaxies. On a very basic level one can view galaxies, galaxy clusters and super clusters as a progression of scale and dynamic evolution.

Thus the dynamical properties of the accreting sub-halos at all scales not only reflect the formation of the underlying host but also give us insight into the formation of objects at other scales. Hence, it is imperative to understand the orbital evolution of these objects and how they deviate from the background dark matter distribution. The first part of this thesis introduces the tools for doing so, and investigates the general properties of accreting objects in galaxy clusters. In the second part of the thesis we examine more specific problems regarding galaxy cluster formation.

Numerical Methods

Cosmological simulations have become an important tool in understanding the formation of structure within the Universe. Modelling this structure formation numerically is important because early in the Universe's history, the evolution of structure becomes non-linear.

Within the ΛCDM paradigm the dominant component of matter involved in structure formation is dark matter. To first order modelling the dark matter (within the ΛCDM cosmological context) can therefore capture structure formation in the Universe.

The simulations used in this thesis were cosmological dark matter simulations. Within these simulations the dark matter is modelled as a collisionless fluid that interacts via gravity alone. In practice the phase space of this collisionless fluid is sampled by N-bodies allowing for a computationally reducible problem and then evolved by solving Poisson's equation. Further details for this can be found in Chapter 2. An example of a cosmological simulation can be seen in Figure 1.2. Starting from an isotropic and homogeneous Universe (upper left), we move to the highly clustered Universe of today, with it's filaments and clusters (cf. Figure 1.1).

Dark matter cosmological simulations have had considerable success in modelling large-scale-structure in the Universe bridging the gap between the picture of the early Universe (CMB) and today. Examples of which include the prediction of the abundance of massive galaxy clusters (e.g. Eke, Cole & Frenk 1996), and the magnitude of large-scale flows of galaxies (e.g. Strauss & Willick 1995; Zaroubi et al. 1997).

While we possess some confidence in the basic model of structure formation on the largest scale, there still remain a number of discrepancies on smaller scales (i.e. $< Mpc$).

The most high profile and contentious of these is the inner density profile of galaxies. Within cosmological simulations the density profiles of virialized CDM halos (Navarro et al. 1996, 1997, 2004; Power et al. 2002) (which are equated with galaxies) are too steep with respect to what is inferred from rotation curves of dwarf spiral and low surface brightness galaxies (McGaugh & De Block 1998).

Second, CDM predicts one-to-two orders of magnitude more satellite galaxies orbiting their host halos. For example, we would expect significantly more dwarf galaxies than are observed in systems such as the Local Group (Moore et al. 1999;

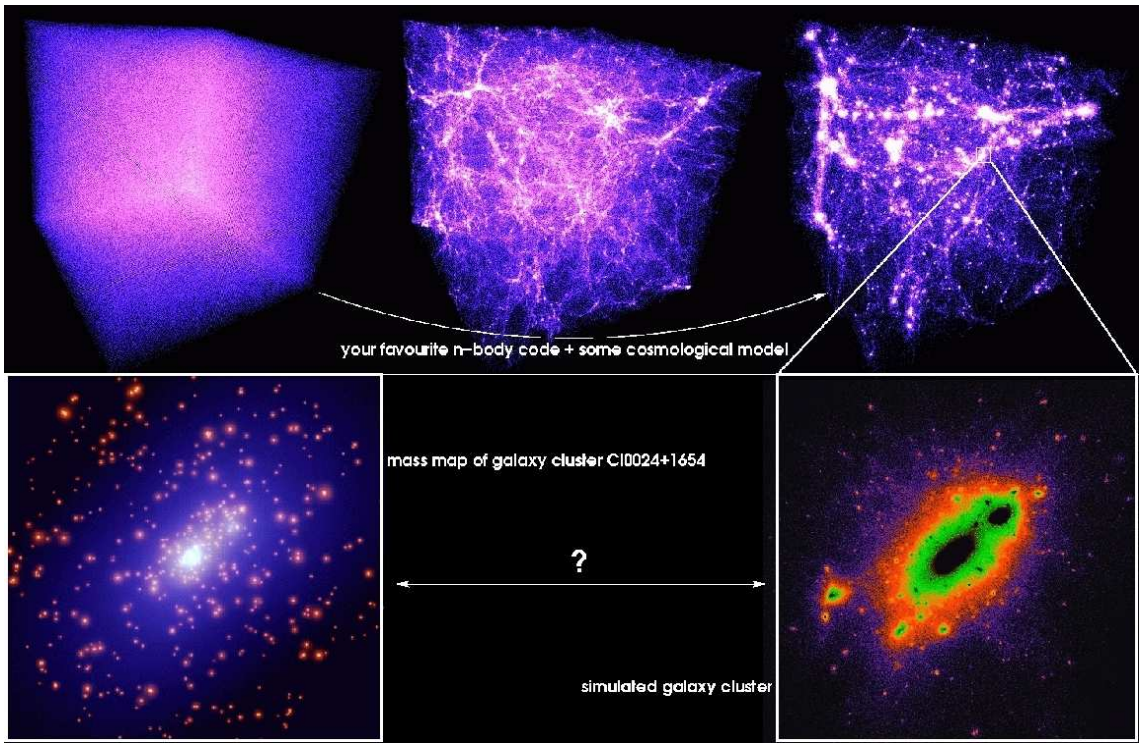

Figure 1.2: Numerical Simulations of the Universe
In the top row, we see a numerical simulation of the formation of large scale structure in a ΛCDM Universe. The simulation begins on the upper left with an isotropic and homogeneous Universe and evolves to the highly clustered Universe of today on the upper right with its filaments and clusters. The simulation box shows a region of 100 Mpc. Zooming into a 2 Mpc region, we find a simulated galaxy cluster (bottom right). This simulated cluster is seen to resemble the observed cluster C10024+1654, whose map is constructed from an analysis of gravitational lensing (bottom left). *Credit: Knebe A. and Kneib J.P*

Klypin et al. 1999a, Ghigna et al. 1998). A considerable amount of work has been done to reconcile this discrepancy, with some suggesting suppressed star formation is due to the removal of gas from the small protogalaxies by the ionising radiation from the first stars and quasars (Bullock et al. 2000; Tully et al. 2002; Somerville 2002) thus leaving most of the satellites completely (or almost completely) dark. Others suggest that the form of dark matter is incorrect appealing to Warm Dark Matter (Knebe et al. 2002; Bode, Ostriker & Turok 2001; Colin et al. 2000).

Recent results from (strong) lensing statistics suggest that the predicted excess of substructure is in fact required to reconcile some observations with theory (Dahle et al. 2003, Dalal & Kochanek 2002), although this conclusion has not been universally accepted (Sand et al. 2003; Schechter & Wambsganss 2002; Evans & Witt 2003). If, however, the lensing detection of halo substructure *is* correct and the overabundant satellite population really does exist, it is imperative to understand the orbital evolution of these objects and their deviation from the background dark matter distribution.

While there has been intense interest, from both a theoretical and an observational perspective, in placing limits on the central dark matter density in galaxies and understanding the abundances of satellite galaxies, comparatively little attention has been paid to the study of the evolution of the spatial and kinematical properties of these satellite galaxy populations. This thesis aims to fill that void.

1.2 Outline of the thesis

As we have already stated, the overarching goal of this thesis to better understand structure formation within the ΛCDM Universe. Using numerical simulations within that theoretical framework it is our aim to shed light on unanswered questions concerning the evolution and fate of cluster galaxies.

Due to the hierarchical nature of structure formation the dynamical properties of the accreting sub-halos at all scales reflect the formation of the underlying host. Therefore, to better understand the formation of clusters and the evolution of their galaxies it is important to understand the orbital evolution of these objects and how they deviate from the background dark matter distribution. The first part of this thesis introduces the necessary analysis tools and investigates the general properties of these accreting objects in galaxy clusters. The second part of this thesis applies

these ideas and techniques to specific questions regarding the dynamics of galaxies in clusters.

Each of the components of this thesis is based upon the series of N-body simulations detailed in Chapter 2.

Part One

Chapter 2: Simulations

In this chapter we introduce the primary cosmological simulation code used throughout the thesis, `MLAPM` (Knebe, Green & Binney 2001). We then detail the series of high-resolution ΛCDM cosmological simulations produced by `MLAPM`. These simulations focus on the formation and evolution of eight dark matter galaxy clusters, each with order a million particles within the virial radius. In addition to high mass and spatial resolution, these simulations also possess numerous data outputs, which enable us to follow the evolution of each individual sub-halo as they fall into the global potential of the cluster. Such a data set is ideal to address the central questions in the thesis. This chapter concludes with a description of the canonical properties of the host halos (galaxy clusters) and various other global quantities such as triaxiality.

Chapter 3: Finding dark matter halos

To take advantage of sophisticated N-body codes and to optimise their predictive power one needs an equally sophisticated halo finder. In Chapter 3 we introduce our new "`MLAPM`-halo-finder" (`MHF`) which is based on the adaptive grid structure of `MLAPM`. We then extend the `MHF` code in order to track the orbital evolution of gravitationally bound objects through any given cosmological N-body-simulation - our so-called "`MLAPM`-halo-tracker" (`MHT`).

Chapter 4: The dynamics of substructure

In this chapter we use these newly developed tools to follow the explicit time evolution of hundreds of dark matter sub-halos within cosmologically self-consistent simulations. Using these tracked sub-halos we investigate a number of phenomenon, including the following: orbit distributions, satellite disruption rate and various velocity distributions relating their physical and dynamical properties to the differing

halo environmental conditions.

Part Two

Chapter 5: Anisotropy of substructure orbits

Nearby clusters such as Virgo and Coma possess galaxy distributions, which tend to be aligned with the principal axis of the cluster itself. This has also been confirmed by a recent statistical analysis of some 300 Abell clusters where the effect has been linked to the dynamical state of the cluster (Plionis et al. 2002). In this chapter we analyse our cluster simulations looking for this same alignment signal in the orbits of the sub-halos.

Chapter 6: Outskirts of dark matter halos

It has been known for some time that galaxy properties in clusters are substantially different from those of galaxies in the field (Hubble & Humason 1931; Oemler 1974; Dressler 1980). However, the origins of these morphology-density relationships are still not fully understood, with several large and small-scale mechanisms proposed to explain their existence. To complement our earlier investigations on the dynamics of sub-halos within the virial radii of the host halos, in this chapter we investigate the galaxy populations in the outskirts of dark halos / galaxy clusters. In particular we focus on the so-called "backsplash population", i.e. satellite galaxies that once were inside the virial radius of the host but now reside beyond it.

Chapter 7: Mapping substructure debris

Since the discovery of stellar streams in the Milky Way (Ibata et al. 2001c, Helmi et al. 1999) and in M31 (Ibata et al. 2001a), and of streams and shells in clusters (Trentham & Mobasher 1998), they have become standard fixtures in our understanding of galaxy and cluster formation. These streams provide important observational support for the hierarchical build-up of galaxies and clusters and the Λ-dominated cold dark matter paradigm.

While previous studies focus on the disruption of satellite galaxies in static analytical potentials, this chapter investigates their disruption in increasingly complex potentials ultimately investigating the disruption of satellites within fully self-consistent high-resolution cosmological galaxy clusters. For each of the simulations

we investigate the real and integrals-of-motion space distributions of the satellite debris.

In the final chapter we outline the major conclusions of our research, and itemise future work to be done.

Chapter 2

Simulations

"In the Universe there is a perfect form for everything, and everything is a shadow of that perfect form."

- Plato

2.1 Introduction

The N-body simulations used throughout this thesis were carried out using the open source adaptive mesh refinement code `MLAPM` (Knebe, Green & Binney 2001). In this Chapter we will present a brief introduction to `MLAPM` and explain why it was an adequate choice of code for our studies. After introducing `MLAPM` we describe how we simulated the eight dark matter galaxy clusters used throughout this thesis. We conclude the chapter with a detailed look at these eight dark matter halos, categorising their differences/similarities.

2.2 MLAPM

`MLAPM` (Multi-Level Adaptive Particle Mesh) is an open source C-code[1]for simulating the formation of structures from collisionless dark matter within a cosmological framework. In the following section we will briefly review the fundamental components of `MLAPM`.

[1]`http://astronomy.swin.edu.au/MLAPM/`

At the heart of MLAPM is the calculation of the gravitational forces. On the domain grid (the cubic grid that covers the entire computational volume) MLAPM utilises a multi-grid method based upon algorithms presented in Brandt (1977) & Press et al. (1992) employing a finite-difference approximation to solve Possion's equation. Alternatively to this pure grid method for the solution of Possion's equation on the domain grid MLAPM also employs a Fast Fourier Transforms (FFT) method.

The limiting force resolution of the domain grid is conservatively estimated as being twice the grid spacing. However, structure formation in the Universe occurs over many orders of magnitude of scale, both in mass and space. To reach high mass resolution MLAPM allows multiple mass species of particles; to reach high force resolution, MLAPM refines its grids in high-density regions with an automated refinement algorithm.

These adaptive meshes are recursive: refined regions can themselves be refined, each subsequent refinement having cells that are half the size of the cells in the parent level. This creates a hierarchy of refinement meshes of different resolutions covering regions of interest. The refinement is done cell-by-cell (individual cells can be refined or de-refined) and meshes are not constrained to have a rectangular (or any other) shape. By having these nested grids we are able to increase the spatial resolution of our simulation only where we require it, hence saving CPU time.

As with the multi-grid method for solving the potential on the domain grid, the potential is solved on these arbitrarily shaped grids through a finite-difference method. The difference between the refinement grids and the domain grids being that instead of having a periodic boundary on the domain, the refinements are solving an independent boundary problem, where the solution on the boundary is fixed from the coarser parent grid.

An example of MLAPM in action is shown in Figure 2.1. The top left panel shows all particles in a slice of thickness 3 Mpc h^{-1} through the simulation box. The right panel indicates the adaptive grids used with that particle distribution. The bottom panels again show the particles' distribution and refinement grids, however, zoomed in on a 4 Mpc h^{-1} square region. In this region one can see the greater detail of the refinement structures.

The criterion for (de-)refining a cell relates the number of particles within that cell, the appropriate choice for this number having been described in detail by Knebe et al. (2001). However, around each high density region a "buffer-zone" of refined cells is created to ensure that the resolution of the grids changes gradually. In

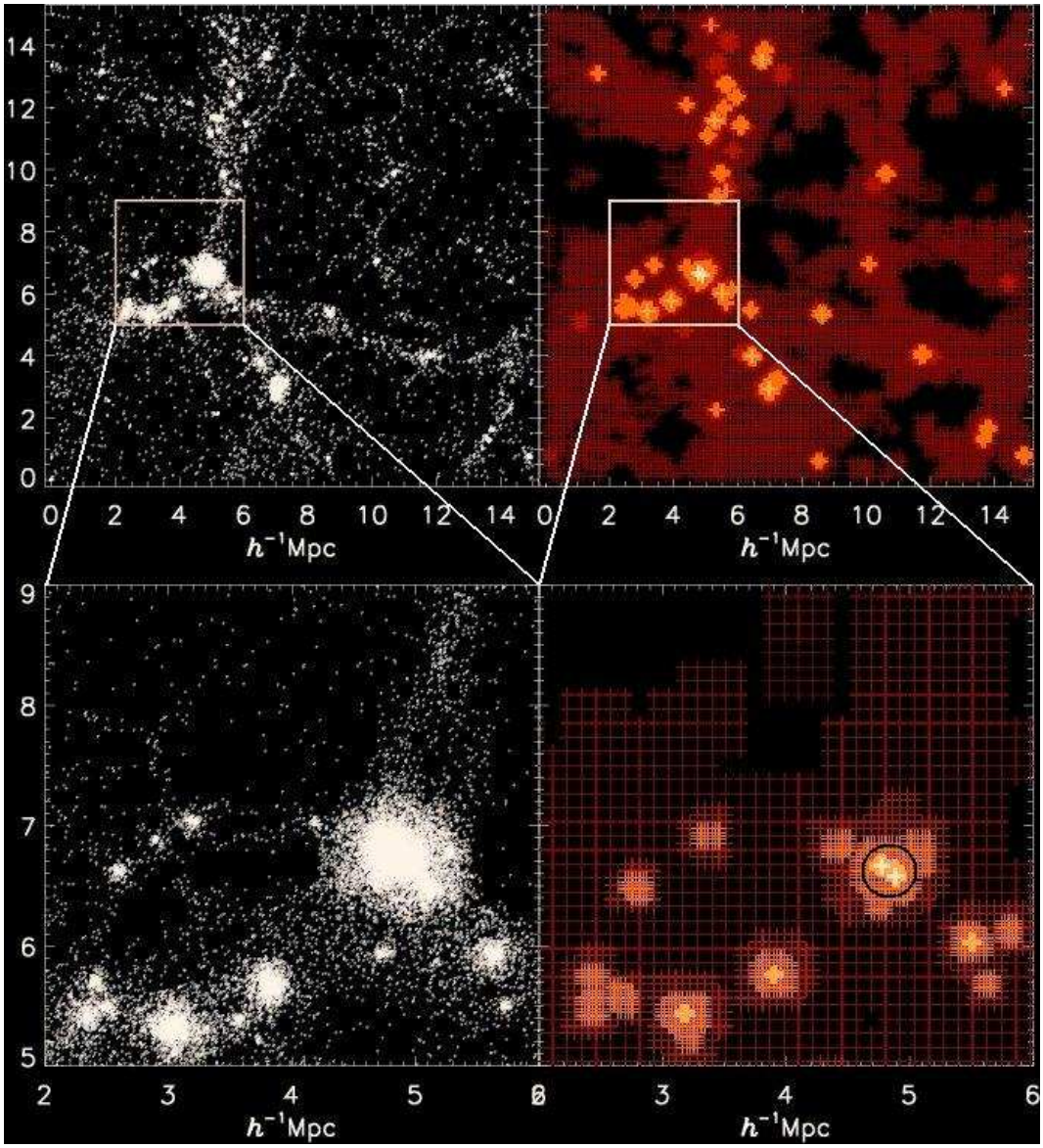

Figure 2.1: `MLAPM`**'s adaptive grids: Particle distribution (left) vs.** `MLAPM` **adaptive grids (right)**
The top left panel shows all particles in a slice of thickness 3 Mpc h^{-1} through the simulation box. The right panel indicates the adaptive grids used with that particle distribution. The bottom panels show the particle distribution and refinement grids, however, zoomed in on a 4 Mpc h^{-1} square region.

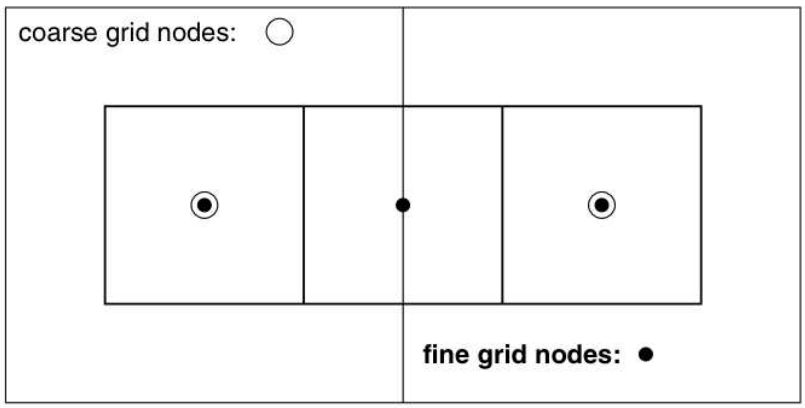

Figure 2.2: `MLAPM`**'s refinement nodes**
Unlike standard AMR codes `MLAPM`'s nodes are a combination of co-spatial nodes and nodes that cross the boundary of parent grids.

practice this means that a grid is refined if either it or one of its 26 neighbours exceeds the particle threshold.

One significant difference between `MLAPM`'s physical grid structure and the usual implementation of adaptive grids (i.e. ART: Kravtsov, Klypin & Khokhlov 1997; Kravtsov 1999) is the alignment of the refinement grids. The normative method symmetrically divides the parent node to create the daughter nodes, whereas some of `MLAPM`'s nodes are co-spatial, thus, we also have nodes that cross the boundary of parent grids (e.g. Figure 2.2).

As the grids align with the parent grids in this manner another constraint on the creation of refinements is that the edges of refinements be co-spatial. Note, these boundary refinements do not hold any particles, however hold the boundary conditions when solving Possion's equation.

One drawback of the refinement grid methods is the memory cost of the grid generation. To overcome this `MLAPM` employs a sophisticated grid structure that utilises the physical location of the information in memory to hold grid information. Further details are provided in Knebe et al. (2001).

On the finer refinement grids the forces are generally larger, thus the cell crossing-time for a particle is shorter. Hence, `MLAPM` uses multiple time-steps on different refinement levels where the time step for each level is a factor of two smaller than the time step on the previous level. `MLAPM` also includes an adaptive time stepping that adjusts the actual time step after every major step to restrict particle movement

across a cell to a particular fraction of the cell spacing. This improves the accuracy and reduces computational time.

2.3 Simulation Suite

Taking advantage of `MLAPM's` ability to efficiently simulate structure in dense environments through its adaptive grids, we have produced a series of high-resolution cosmological simulations that have focused on the formation and evolution of eight dark matter galaxy clusters, each containing of order a million particles.

To that end we first created a set of four independent initial conditions at redshift $z = 45$ in a standard ΛCDM cosmology ($\Omega_0 = 0.3, \Omega_\lambda = 0.7, \Omega_b h^2 = 0.04, h = 0.7, \sigma_8 = 0.9$). Next, 512^3 particles were placed in a box of side length $64h^{-1}$ Mpc giving a mass resolution of $m_p = 1.6 \times 10^8 h^{-1}$ $M_\odot$. For each of these initial conditions we iteratively collapsed the closest eight particles to one particle reducing our particle number to 128^3 particles. These lower mass resolution initial conditions were then evolved until $z = 0$.

At $z = 0$, eight clusters from our simulation suite were selected in the mass range 1–3$\times 10^{14} h^{-1}$ $M_\odot$, each sampling differing environmental conditions. Then, as described by Katz (1994) and Ghigna (1998), for each cluster the particles within three times the virial radius were tracked back to their initial positions of the starting redshift ($z = 45$). Those particles were then regenerated to their original mass resolution and positions, with the next layer of surrounding large particles regenerated only to one level (i.e. 8 times the original mass resolution), and the remaining particles were left 64 times more massive than the particles resident with the host cluster. This conservative criterion was selected in order to minimise contamination of the final high-resolution halos with massive particles.

One such simulated cluster can be seen in Figure 2.3. The top image showing the entire simulation box at $z = 0$ with the three different mass species independently coloured. Red representing the lowest resolution particles (i.e. 64 times m_p), the green the intermediate mass particles (i.e. 8 times m_p) and the blue the high-resolution particles (with mass = m_p). The lower image is a line-of-sight density projection of the high-resolution region of the galaxy cluster (showing one in every eight particles).

At the end of the high-resolution re-simulations the force resolution is again de-

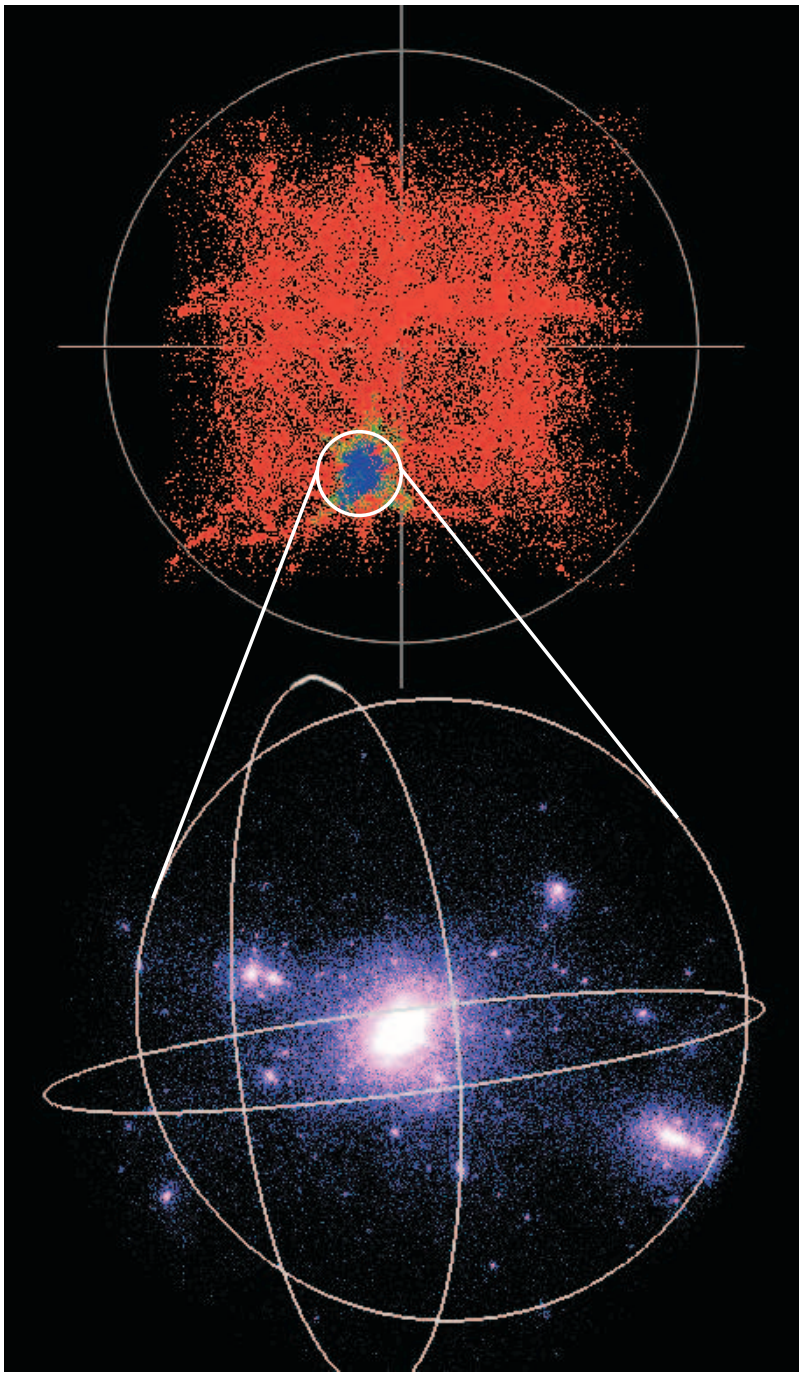

Figure 2.3: Re-simulated Dark Matter halo

This figure shows the re-simulated Dark Matter halo (blue) and the parent simulation that hosted the re-simulated halo. The parent simulation (at $z = 0$) has box size $64h^{-1}$ Mpc and three different mass species. The red particles representing the low-resolution simulation particles, the green particles the intermediate mass simulation particles and the blue particles the high-resolution simulation particles of the re-simulated halo. In the bottom panel (for the re-simulated halo) the line-of-sight density is shown for one in every eight high-resolution particles.

termined by the highest refinement level reached. The whole computational volume was covered by a regular domain grid consisting of 256^3 cells. We had two separate criteria for refinement, a domain cell was refined when there was more than one particle per cell; further, every subsequent refinement was refined when there were more than four particles per cell. Thus the finest grid at $z = 0$ consisted of 65,536 cells per side, giving a force resolution of $\sim 2h^{-1}$ kpc which allows us to resolve the host halos down to the central $\sim$0.25% of the virial radii of the host halos (see Table 2.5).

The halos chosen were selected to investigate the evolution of satellite galaxies and their debris in an unbiased sample of host halos, exploring the influence of environment upon the evolution of such systems.

To achieve this goal, excellent temporal resolution is required - as such we retained 17 outputs from $z = 2.5$ to $z = 0.5$, equally spaced with $\Delta t \approx 0.35$Gyrs, supplemented with an additional 30 outputs spanning $z = 0.5$ to $z = 0$ with $\Delta t \approx 0.17$Gyrs. As we show in the next chapter the average number of orbits completed for our satellites is, one-to-two. Therefore we have 10-20 outputs available to accurately define the orbit of a given satellite, which is more than adequate to trace a "live" orbit properly. We found that to sufficiently sample a live satellite orbit one needs at least eight time-steps (Gill et al. 2004b).

2.4 Host halos

2.4.1 Canonical Properties

A simple analysis of the simulation at redshift $z = 0$ provides us with the relevant information on the host halo. Defining the halo mass to be the total mass within the virial radius $R_{\rm vir}$, thus double counting the mass in the substructure and sub-substructure, the halo masses ranged between 1–3 $\times 10^{14}$ h^{-1} $\mathrm{M}_\odot$ at $z = 0$. The virial radii in turn were defined at the point where the mean averaged density of the host (measured in terms of the cosmological background density ρ_b) drops below $\Delta_{\rm vir} = 340$ with $M_{\rm vir}$ being the mass enclosed by that sphere. The formation redshift $z_{\rm form}$ is defined here as the redshift where the halo contained half of its present day mass (Lacey & Cole 1994). Applying this criterion to our data we find that the ages of our host halos range from 8.3 Gyrs to 3.4 Gyrs. In other words, while the masses of our systems are comparable, they are of different dynamical age. In Table 2.5, as

in all following figures, the halos are ordered 1-8 in age.

2.4.2 Triaxiality

Another property of the halos is their triaxiality (Dubinski & Carlberg 1991; Franx, Illingworth & Zeeuw 1991; Warren et al. 1992; Cole & Lacey 1996; Jing & Suto 2002; Bailin & Steinmetz 2004). To calculate the triaxiality of the host halos we utilise the adaptive grids of `MLAPM`.

Each refinement level of `MLAPM` can be viewed as a density cut or isodensity surface through the simulation. Identifying the isolated refinements associated with the host halo (see Figure 2.4) we calculate the inertia tensor, weighing the contribution of each grid cell by the density within the cell, then diagonalising the tensor. One obvious advantage of this method is that there are no assumptions regarding spherical symmetry - the grids are generated cell-by-cell and they are an arbitrary shape.

As the triaxiality of the host halos varies over its radius we chose the "core" region as defined by the 6^{th} refinement level in `MLAPM` to define triaxiality upon. According to the refinement criterion adopted in the simulations the 6^{th} level surrounds material about 3000 times denser than ρ_b or in other words 9 times denser than the material at the virial radius. The host halos are well described - at least in the range from $6h^{-1}$ kpc out to the virial radius - by the density profiles advocated by Navarro, Frenk & White (1997) with concentration parameters in the range $c = 5 - 7$. Therefore, a density of roughly $9 \times \rho(r_{\text{vir}})$ corresponds to about the half-mass radius of the host.

The eigenvalues λ_i where $i \; \epsilon\{1, 2, 3\}$ of the interia tensor can be related to the halo's axis e_i where $i \; \epsilon\{1, 2, 3\}$ via the simple relationship $e_i = \sqrt{N}\sqrt{\lambda_i}$. Using the eigenvalues we can construct the triaxiality parameter T (Franx, Illingworth & Zeeuw 1991) where:

$$T = \frac{(e_1^2 - e_2^2)}{(e_1^2 - e_3^2)} \tag{2.1}$$

Further, the eigenvectors $\vec{\lambda}_{1,2,3}$ (with $\vec{\lambda}_1$ being the major axis) of its inertia tensor define the orientation of the triaxial halo. This co-ordinate system will be used **later** to investigate properties of the sub-halos i.e. the alignment of the sub-halos with the triaxial host.

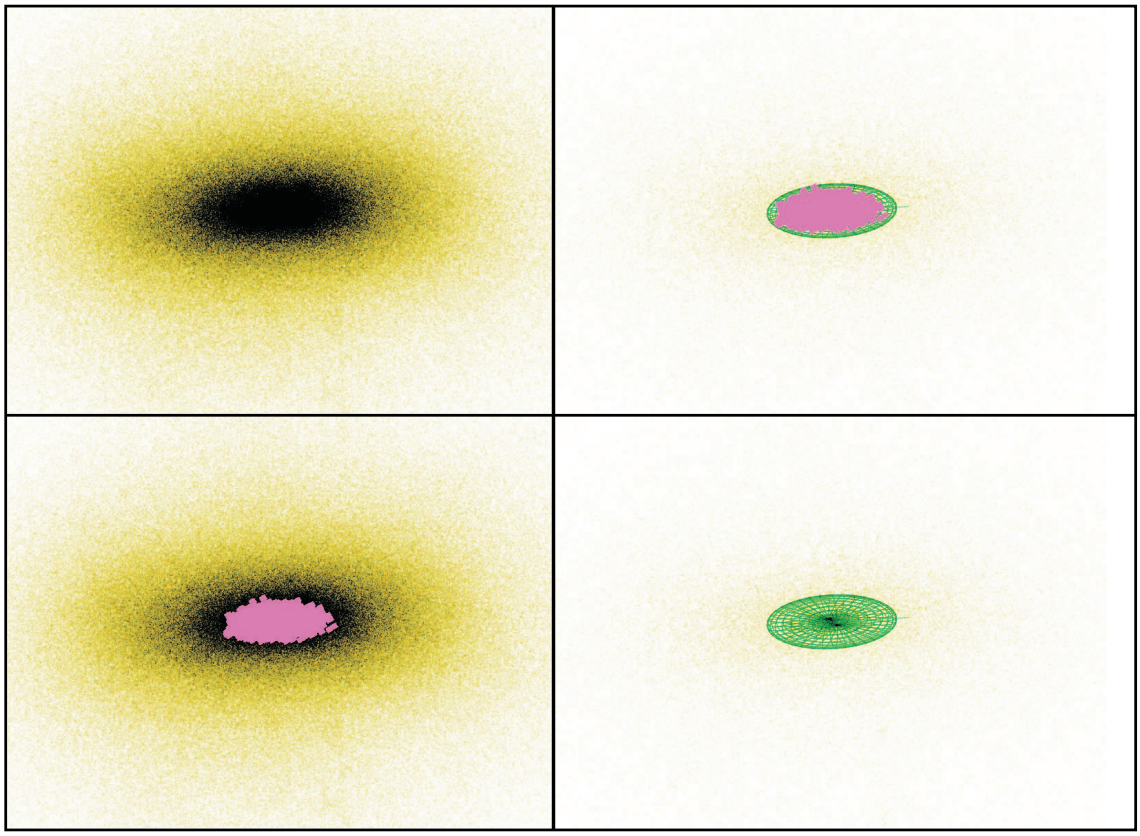

Figure 2.4: Dark matter host halo triaxiality
This series of four images demonstrates the calculation of dark halo triaxiality. The top left image simply shows the line-of-sight projected density of a dark matter halo (Halo #1), with the substructure removed. The bottom shows the same image, however, it also shows `MLAPM` refinement level # 6 in pink. The top right image show the dark halo again, however, only showing 1 in every 32 particles, along with the refinement and the inferred ellipticity shown by the green ellipse. This green ellipse is easier to see in the bottom right image when we remove the `MLAPM` refinements.

2.4.3 Formation History

As we are interested in investigating the influence of host halo formation history and environment on the orbital and internal properties of the satellites galaxies living within its virial radius, it is important to understand how the host halos actually formed.

As indicated by Tormen (1997) the formation of dark matter halos can be characterised by two different phases: one corresponding to a rapid increase in halo mass, representative of a major merger. We refer to this phase as a violent (**V**) period. The second phase is one of relaxation in which the halo processes the merger and settles toward virial equilibrium. A halo may continue to accrete smaller halos during this phase. We refer to this phase as a quiet (**Q**) period.

The history of each halo is briefly outlined below using the simplified keys V or Q to signify violent or quiet episodes. For example, halo #1 has a history "QVQQ", that is, a quiet period around the time of formation $z_{\rm form}$ followed by a violent period of merging of about the same length and completed by quiet evolution for the remainder of the evolution, which lasts for twice as long as either of the two earlier episodes. The coding chain splits the evolution since formation up into more-or-less equal segments, but has nothing to say about the absolute timescales, which differ widely from halo to halo. A qualitative summary of the eight halos follows:

Halo #1 (QVQQ)

A reasonably quiet history with no major violent encounters, save for a medium one at $z = 0.7$.

Halo #2 (QVQQ)

A generally quiet history with a medium size merger one quarter of the way through its evolution at $z = 0.53$, quickly settling for the rest of its formation.

Halo #3 (QVVVQ)

An initial short quiet period followed by a long and violent interaction that takes essentially the rest of its formation time to settle.

Halo #4 (VQQ)

An initially violent merger which quickly settles for the rest of its formation.

Halo #5 (V)

A very violent formation history with a strongly oscillating potential.

Halo #6 (V)

A steady, yet violent, formation history.

Halo #7 (V)
A formation history quite similar to that of halo #6.
Halo #8 (V)
A rapid formation history; constantly interacting with two other large halos. In this sense, a unique system.

While useful, such a qualitative description needs to be augmented with a quantitative one. In order to do so, we use the dispersion of the rate of relative mass change of the host halos:

$$\sigma^2_{\Delta M/M} = \frac{1}{N_{\rm out}} \sum_{i=2}^{N_{\rm out}} \left(\frac{\Delta M_i}{\Delta t_i M_i} - \langle \frac{\Delta M}{\Delta t M} \rangle_i \right)^2 , \tag{2.2}$$

where $N_{\rm out}$ is the number of available outputs from formation $z_{\rm form}$ to redshift $z = 0$, $\Delta M_i = M(z_i) - M(z_{i-1})$ the change in the mass of the host halo, and Δt_i the respective change in time. The mean growth rate at time i

$$\langle \frac{\Delta M}{\Delta t M} \rangle_i = \frac{1}{N_i} \sum_{j=1}^{N_i} \left(\frac{\Delta M_i}{\Delta t_i M_i} \right)_j \tag{2.3}$$

is calculated for each individual output as the average over all halos N_i available at that time step.

A large dispersion $\sigma_{\Delta M/M}$ indicates a violent formation history whereas low values correspond to quiescent formation histories. As we can see in Table 2.5, our qualitative classification scheme is confirmed by the $\sigma_{\Delta M/M}$ values.

2.5 Summary and Conclusion

In this chapter we were briefly introduced to the cosmological simulation code `MLAPM`. We then used that code to create a suite of eight simulated galaxy cluster dark matter halos based on the re-simulation technique outlined by Katz (1994) and Ghigna (1998). These cluster halos will become the base simulations used throughout the thesis to investigate the populations of sub-halos (galaxies in our case) that exist and are transformed within dark halos (clusters of galaxies for the simulations at hand).

The final part of this chapter is dedicated to analysing and describing the differences in the host halos. These host halos were chosen to sample a variety of

Table 2.1: Summary of the eight host dark matter halos. Distances are measured in h^{-1} Mpc, velocities in km s^{-1}, masses in $10^{14}h^{-1}$ M$_\odot$, and the age in Gyrs.

Halo	$R_{\rm vir}$	c	$V_{\rm circ}^{\rm max}$	$M_{\rm vir}$	$z_{\rm form}$	age	Triaxiality	$\sigma_{\Delta M/M}$	form. hist.
# 1	1.34	8.7	1125	2.87	1.16	8.30	0.67	0.10	QVQQ
# 2	1.06	9.6	894	1.42	0.96	7.55	0.87	0.10	QVQQ
# 3	1.08	5.9	875	1.48	0.87	7.16	0.83	0.10	QVVVQ
# 4	0.98	7.7	805	1.10	0.85	7.07	0.77	0.09	VQQ
# 5	1.35	6.0	1119	2.91	0.65	6.01	0.65	0.15	V
# 6	1.05	8.1	833	1.37	0.65	6.01	0.92	0.15	V
# 7	1.01	6.6	800	1.21	0.43	4.52	0.89	0.25	V
# 8	1.38	3.7	1041	3.08	0.30	3.42	0.90	0.22	V

triaxialities, formation times and mass/satellite accretion, despite being of comparable mass. The halos also had very different formation histories, from quiescent to violent. A summary of the eight host halos is presented in Table 2.5 where the halos are presented and numbered from oldest to youngest.

Chapter 3

Finding Dark Matter Halos

"What I find most disheartening is the thought that somewhere out there our galaxy has been deleted from somebody else's sample."

- Dr Alexander Boksenberg (1996)

3.1 Introduction

Over the last 30 years great progress has been made in the development of N-body codes that model the distribution of dissipationless dark matter. Algorithms have advanced considerably since the first N^2 particle-particle codes (Aarseth 1963; Peebles 1970; Groth et al. 1977); we have seen the development of the tree-based gravity solvers (Barnes & Hut 1986), mesh-based solvers (Klypin & Shandarin 1983), then the two combined (Efstathiou et al. 1985) and multiple strands of adaptive and deforming grid codes (Villumsen 1989; Suisalu & Saar 1995; Kravtsov, Klypin & Khokhlov 1997; Bryan & Norman 1998; Knebe, Green & Binney 2001). While they all push the limits of efficiency in computational resources, each code has its individual advantages and limitations. The result of such research has been highly reliable, cost effective codes. However, producing the data is only one step in the process; the ensembles of millions of (dissipationless) dark matter particles generated still require interpreting and then comparison to the real Universe. This necessitates access to analysis tools to map the phase-space which is being sampled by the particles onto "real" objects in the Universe; traditionally this has been accomplished through the use of "halo finders". Halo finders mine N-body data

to find locally over-dense gravitationally bound systems, which are then attributed to the dark halos we currently believe surround galaxies. Such tools have lead to critical insights into our understanding of the origin and evolution of structure and galaxies. To take advantage of sophisticated N-body codes and to optimise their predictive power one needs an equally sophisticated halo finder.

Over the years, halo-finding algorithms have paralleled the development of their partner N-body codes. We briefly outline the major halo finders currently in use:

The Friends-of-Friends (FOF) (Davis et al. 1985; Frenk et al. 1988) algorithm uses spatial information to locate halos. Specifying a linking length $b_{\rm link}$ the finder links all pairs of particles with separation equal to or less than $b_{\rm link}$ and calls these pairs "friends". Halos are defined by groups of friends (friends-of-friends) that have at least one of these friendship connections. Two such advantages of this algorithm are its ease of interpretation and its avoidance of assumption concerning the halo shape. The greatest disadvantage is its simple choice of linking length which can lead to a connection of two separate objects via so-called linking "bridges". Moreover, as structure formation is hierarchical, each halo contains substructure and thus the need for different linking lengths to identify "halos-within-halos". There have been many variants to this scheme which attempt to overcome some of these limitations (Suto, Cen & Ostriker 1992; Suginohara & Suto 1992; van Kampen 1995; Okamoto & Habe 1999; Klypin et al. 1999b).

DENMAX (Bertschinger & Gleb 1991; Gleb & Bertschinger 1994) and SKID (Weinberg, Hernquist & Katz 1997) are similar methods in that they both calculate a density field from the particle distribution, then gradually move the particles in the direction of the local density gradient ending with small groups of particles around each local density maximum. The FOF method is then used to associate these small groups with individual halos. A further check is employed to ensure that the grouped particles are gravitationally bound. The two methods differ through their calculation of the density field. DENMAX uses a grid while SKID applies an adaptive smoothing kernel similar to that employed in Smoothed Particle Hydrodynamics techniques (Lucy 1977; Gingold & Monaghan 1977; Monaghan 1992). The effectiveness of these methods is limited by the method used to determine the density field (Götz, Huchra & Brandenberger 1998).

A similar technique to the above is the Bound Density Maxima (BDM) method (Klypin & Holtzman 1997; Klypin et al. 1999b). In this scheme a smoothed density is derived by smearing out the particle distribution on a scale $r_{\rm smooth}$ of order the

force resolution of the N-body code used to generate the data. Randomly placed "seed spheres" with radius $r_{\rm smooth}$ are then shifted to their local centre-of-mass in an iterative procedure until convergence is reached. Hence, as with DENMAX and SKID, this process finds local maxima in the density field. Bullock et al. (2001) further refined the BDM technique by first generating a set of possible centres, ranking the particles with respect to their local density and then implementing modifications which allow for credible identification of halos-within-halos. The Bullock et al. (2001) adaptation to BDM is geared towards finding halo substructure.

When one is primarily concerned with distinct halos, all the mentioned methods perform exceedingly well. All efforts to refine and enhance those halo finding algorithms are due to the fact as we have seen in Chapter 1 that N-body codes overcame overmerging only recently (Klypin et al. 1999b) and are capable of finding satellites galaxies within dark matter host halos. It is therefore crucial to reliably identify "halos-within-halos". In fact, we saw that one of the remaining problems for simulations of CDM structure formation is that high-resolution simulations nowadays predict far greater substructure (in total) than observed (Klypin et al. 1999a; Moore et al. 1999).

Results from gravitational microlensing suggest that the majority of substructure which does exist has to be close to the inner regions (Dalal & Kochanel 2002) which thus far has not been confirmed by such simulations. There are recent claims that although the (numerical) overmerging problem has disappeared in the outer regions of the halo, the inner regions might still suffer from it (Taylor, Silk & Babul 2003). As these latter semi-analytic models do not suffer from such numerical problems, they find that such substructure does exist in the inner regions. The question though arises as to whether there still remains an overmerging problem in the simulations or if current halo finding algorithms actually do break down at those scales. As we will discuss later, it becomes more difficult to locate peaks in the central region (if at all present) of the host halo due to a simple lack of contrast to the dense background.

In this chapter we present a new method for identifying gravitationally bound objects within cosmological simulations using the adaptive meshes of `MLAPM`. This new code excels at finding "halos-within-halos" revealing more substructure in the inner regions of the host halo. In its native form, our new algorithm works naturally "on-the-fly", but it has also been constructed with the flexibility necessary to handle a single temporal output from any N-body code. Our analysis software is publicly

available and packaged with both the MLAPM distribution[1] and soon to be released AMIGA code (the successor of MLAPM). The outline of the chapter is as follows. In Section 3.2 we introduce the new halo finder "MLAPM-halo-finder" (MHF), describing its functionality, advantages, and limitations. Section 3.3 provides a brief analysis of the satellites found by MHF. In Section 3.4 we introduce the "MLAPM-halo-tracker" (MHT) which augments the halo finder by incorporating the ability to track the temporal evolution of satellites. Analysis of the halos tracked with MHT is described in Section 3.5. We next compare the two methods with other publicly available halo finding algorithms, such as FOF and SKID, in Section 3.6. In the second last section, Section 3.7 we describe the additional changes to MHF. We conclude with a summary and our conclusions in Section 3.8.

3.2 MHF: MLAPM's Halo Finder

The general goal of a halo finder is to identify gravitationally bound objects. As all halos are centred about local over-density peaks they are usually found simply by using the spatial information provided by the particle distribution. Thus, the halos are located as peaks in the density field of the simulation. To locate objects in this fashion, the halo finder is required in some way to reproduce the work of the N-body code in the calculation of the density field or the location of its peaks. When locating halos like this, the major limitation will always be the appropriate reconstruction of the density field. With that in mind we introduce MLAPM's-Halo-Finder, MHF (or simply Finder) hereafter.

MHF uses the adaptive grids of MLAPM to locate the satellites of the host halo. As previously mentioned in Section 2, MLAPM's adaptive refinement meshes follow the density distribution *by construction*. Grid structure naturally "surrounds" the satellites, as the satellites are simply manifestations of over-densities within (and exterior) to the underlying host halo, a view which can best be appreciated through inspection of Figure 3.1. In this figure, the refinement grids of MLAPM are superimposed over the projected density of the particle distribution. The top image is the 5^{th} refinement level, with the 6^{th} and 7^{th} levels shown below. We emphasise that the grids get successively smaller and are subsets of other grids on lower refinement levels. The advantage of reconstructing and using these grids to locate halos is that

[1] http://www.aip.de/People/AKnebe/MLAPM/

they naturally follow the density field with the *exact* accuracy of the N-body code. No scaling length is required, in contrast with techniques such as FOF. Therefore, MHF avoids one of the major complications inherent to most halo finding schemes as a natural consequence of its construction.

To locate appropriate halos within our simulation outputs we first build a list of "potential centres" for the halos. Using the full adaptive grid structure invoked by MLAPM, with the same refinement criterion as for the original runs, we restructure the hierarchy of nested isolated MLAPM grids into a "grid tree". This reconstruction is illustrated in Figure 3.2. Thus each of the branches of this tree is a Dark matter halo, with the densest cell in the end of a branch marking a prospective Dark Matter halo centre. This centre is then stored in a list of prospective halo centres.

Within a typical simulation (assuming a density cut at the virial density) one can imagine a number of grid trees populating the simulation. Each one of these trees would be a host halo with each branch being a sub-halo one of the branches is the host!. However, because of the arbitrary way the grids are created each branch can further, have branches thus we have sub-sub-halos. This embedded halo within halo is obviously only limited by the simulation resolution.

Assuming that each of these peaks in MLAPM's adaptive grids is the centre of a halo, we step out in (logarithmically spaced) radial bins until the density reaches $\rho_{\rm satellite}(r_{\rm vir}) = \Delta_{\rm vir}(z)\rho_b(\mathrm{z})$, where ρ_b is the universal background density, unless we reach a point $r_{\rm trunc}$ where an upturn in the radial density profile is detected. This rise is encountered for (almost) all satellites embedded within the background density of the host halo, a point that we will discuss in more detail in Section 3.3. The outer radius of the satellite is defined to be either $r_{\rm vir}$ or $r_{\rm trunc}$, whichever is smaller, and dubbed $r_{\rm MHF}$. Using all particles interior to $r_{\rm MHF}$ we calculate other canonical properties for each halo such as its mass, rotation curve, and velocity dispersion.

We now, however, need to prune the list of (still prospective) halos. The first step in this process is to check if there are any duplicate halos (One could imagine that we caught two halos in the very final stages of merging.) Thus for each satellite a set of "duplicate candidates" is constructed based on the criterion that their centres lie within each others' outer radii $r_{\rm MHF}$. Then, this list is then evaluated by comparing the internal properties of the candidates. A candidate was affirmed to be a duplicate once its mass, velocity dispersion, and centre of mass velocity vector agreed to within 80%. We then kept the halo with the higher central density and removed the other one from the satellite catalogue completely. This is a rare circumstance, yet one to

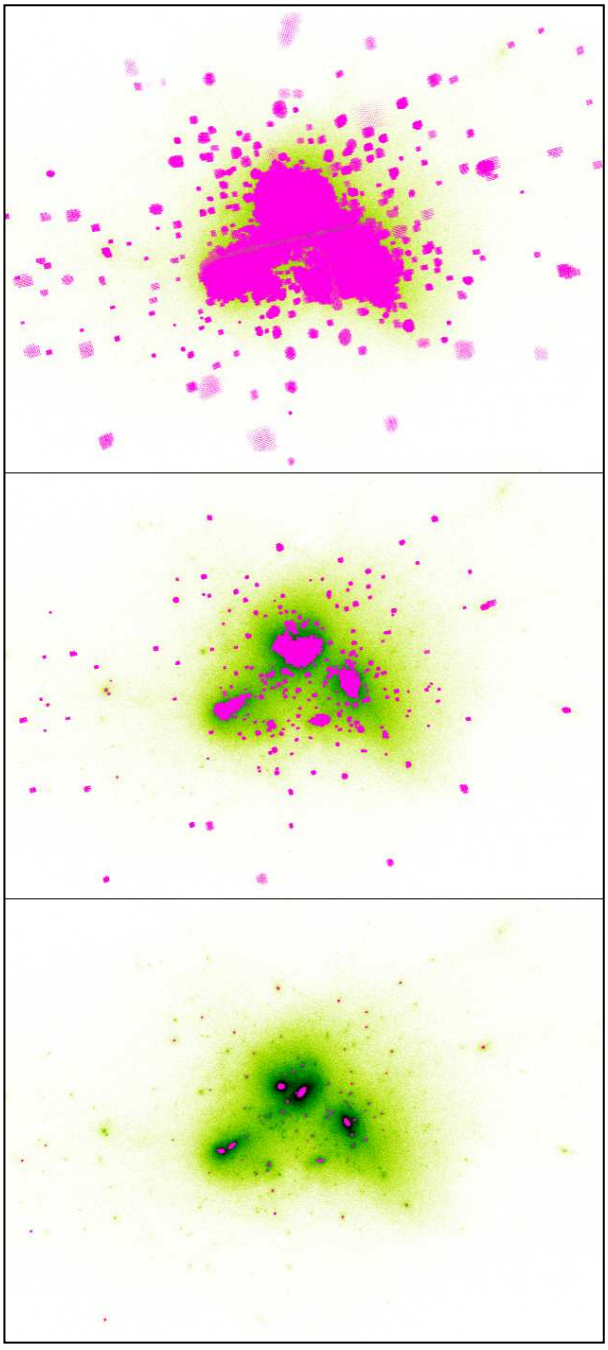

Figure 3.1: `MLAPM`**'s refinement grid structure**
This panel shows a series of 3 consecutive refinement levels of `MLAPM`'s grid structure starting at the 5th refinement level superimposed upon the density projection of the particle distribution.

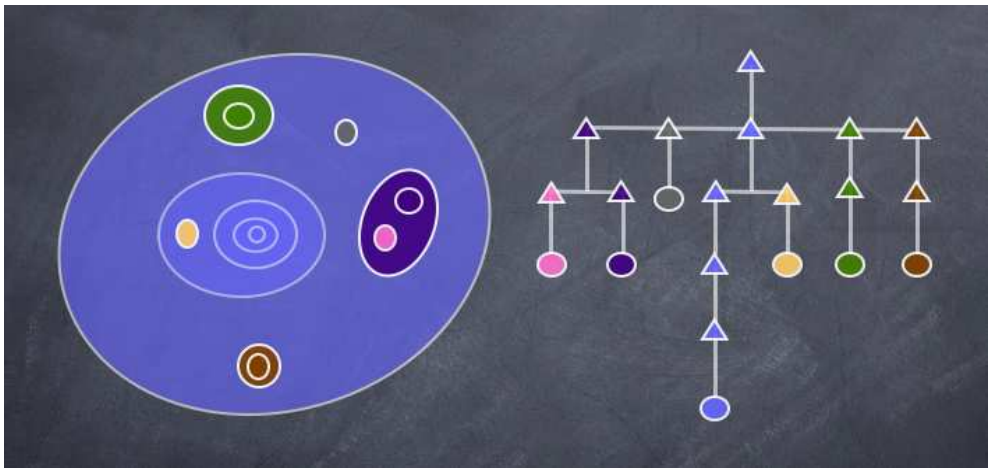

Figure 3.2: MHF's "grid tree" reconstruction
This figure illustrates the restructuring of the nested MLAPM grids into to the "grid tree". The left side represents an idealised refinement grid structure, while the right side shows the re-ordering of these grids into a "grid tree". Note that each branch of the grid tree represents a single dark matter halo within the simulation.

which we will return in Section 3.3.

With our nearly complete set of halos now in hand, we proceed to remove gravitationally unbound particles. This again is done in an iterative process. Starting with the MHF halo centre, we calculate the kinetic and potential energy for each individual particle in the respective reference frame and all particles faster than two times the escape velocity are removed from the halo. We then recalculate the centre, and proceed through the process again. This pruning is halted when a given halo holds fewer than the stated minimum number of particles or when no further particles need to be removed. This procedure also accounts for the rare instances that isolated grids were generated through numerical noise or coincidence (i.e. the crossing of two debris streams) since these halos are very small and contain unbound members.

We finish by recalculating the internal properties of the halos with the radial density profiles of the satellites fitted to the functional form proposed by Navarro, Frenk & White (1997). Note we use the cumulative rather than the differential density profile to increase our number statistics.

$$\rho^{\mathrm{cum}}(r) = \frac{M(<r)}{\frac{4\pi}{3}r^3} \propto \frac{1}{(r/r_s)(1+r/r_s)^2}. \tag{3.1}$$

in the range from $8h^{-1}$ kpc ($\approx 4\times$force resolution) to $r_{\texttt{MHF}}$. The scale radius r_s is used to define the concentration of the halo

$$c = r_{\rm vir}/r_s. \tag{3.2}$$

The procedure outlined above naturally deals with overlapping halos and substructure halos, respectively. But as mentioned before, for such objects the virial radius can not be determined properly as we will observe a rise in the radially binned density profile due to the overlap with another halo or the embedding into the host. In that case we set the outer radius of the (sub-)halo to be that point where the density profile rises and all canonical properties are derived using all (gravitationally bound!) particles interior to that radius. And the fit to an NFW profile Eq. (3.1) is only done out to that radius, too. The situation is different once both of the overlapping halo's centres are within each other's virial/upturn radius: we then checked, if those two objects are just duplicates by comparing their internal properties.

As stated in 2, it is our aim to investigate the evolution of satellite galaxies within their host halos. Thus, we restrict our satellites to having at least 50 high-resolution simulation particles, which corresponds to a mass-cut of $M_{\rm cut} \approx 10^{10}h^{-1}$ M$_\odot$. Moreover, each satellite must contain at least 50% percent of its mass in high-resolution particles. In practice, this latter constraint is not a critical one, relevant only for satellites well beyond twice the host halo's virial radius.

`MHF` is implemented into `MLAPM` in a way that provides the user simultaneously with a snapshot of the dark matter particles *and* halo catalogues at each required output. The most obvious advantages of having the analysis performed "on the fly" are the reduction in computer and human hours in the initial halo analysis stage. Embedding the halo analysis in the code also enables us to potentially analyse the data at unprecedented time resolution, if required.[2] However, `MHF` can also be used with any already existing single time-step snapshot and hence is not limited to data produced by `MLAPM`; it can also be used for any N-body output provided the latter is converted to `MLAPM`'s binary format using the tools included in the `MLAPM` distribution. However, to this date read routines for TIPSY and GADGET (version 1) and GADGET-2 formats are implemented within `MLAPM` and hence `MHF`.

[2] `MHF` can be switched on either to act only when writing an output file (`-DMHF`) or at each individual time step (`-DMHFstep`).

3.3 Analysis of MHF halos

MHF was applied to each of the 376 temporal outputs (47 outputs per each of the eight independent halos), providing us with a list of all satellites and their internal properties at each individual redshift under consideration. As stated earlier, the detailed analysis of the science associated with these satellites presented in proceeding chapters. We do however wish to highlight several key preliminary results here which relate specifically to the halo identification process.

In Figure 3.3 we plot the normalised number of satellites as a function of normalised radius. One, perhaps not surprising, aspect of Figure 3.3 is the similarity in the slopes. Although the number of satellites in each halo may vary, the relative radial distribution of the satellites is similar across halos. This is reminiscent of the universal density profile of dark matter halos, as described by Navarro, Frenk & White (1997). Although the radial distribution of the satellites remains consistent, there exists a range of substructure densities for the halos, as there is a spread in the number of satellites within each halo (recall Table 1). Therefore, we should be able to distinguish the effects of substructure density on the physical properties of the satellites.

The other striking feature of Figure 3.3 is the lack of satellites in the inner 15% of the virial radius. One might ask why this is the case. Does it indicate that satellites dynamically avoid the central region of the halo? Perhaps they simply do not spend much time there? Perhaps via physical means satellites that venture near the centre are either merged or experience such strong tidal forces that they are destroyed? Perhaps we are simply dominated by numerical effects and are witnessing the premature destruction of halos in dense environments. This latter problem - known as *overmerging* - affected low-resolution dissipationless simulations in the early 1990s, failing to produce galaxy-sized dark matter halos in clusters (e.g. Summers et al. 1995; van Kampen 1995; Moore et al. 1996). Traditionally, this was explained by the lack of dissipation in the simulations. With the inclusion of a baryonic component, denser objects could form and survive in the centres of these dense regions. However, with the onset of higher resolution simulations a converse effect was encountered - specifically, an *abundance* of substructure was found (Klypin et al. 1999b).

The explanation of overmerging (or substructure disruption) was accredited to numerical limitations in the simulations. van Kampen (1995) found that parti-

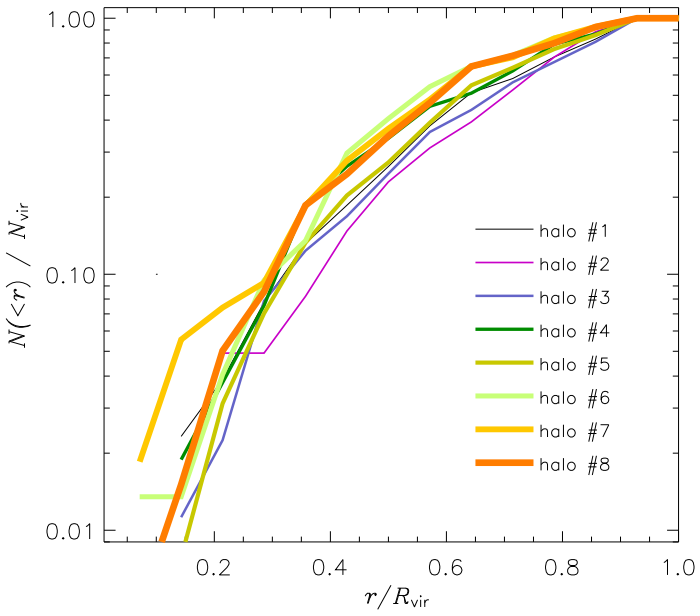

Figure 3.3: Radial distribution of satellites: `MHF`
Number of satellites (normalised) orbiting within the virial radius of the host halo at $z = 0$, as a function of radial distance r, normalised by the virial radius of the respective host $R_{\rm vir}$.

cle evaporation due to two-body effects is only important for low particle number halos (<30 particles). Moore et al. (1996) further investigated particle halo heating, which they concluded was negligible should sufficient mass resolution exist. Moore et al. also demonstrated the for satellites in a static host potential, if a simulation had insufficient spatial resolution, halos would have artificially large cores and hence undergo accelerated tidal disruption. They also found that halos become unstable and are erased when the tidal radius is smaller than approx 2-3 times the halo core radius (which itself can be related to the gravitational softening length). Klypin et al. (1999b) investigated the issue of "overmerging" in great detail using a variety of higher resolution simulations, concluding that the resolution required to avoid artificial destruction of galaxy-sized halos of mass $\approx 10^{11}h^{-1}$ $M_{\odot}$was ≤ 2 h^{-1} kpc (spatial) and $\leq 10^{9}h^{-1}$ $M_{\odot}$ (mass).

Since we appear to have sufficient numerical resolution and our data lies well within the limits of not being dominated by overmerging, one might query whether or not the lack of substructure in the inner region is due to a limitation of our halo finder. When defining the radius of our halos we could not for all halos follow the density profiles out to $r_{\rm vir}$ defined via $\rho_{\rm sat}(r_{\rm vir}) = \Delta_{\rm vir}\rho_b$; as noted earlier, it was necessary in many cases to define a truncation radius $r_{\rm trunc}$. The existence of $r_{\rm trunc}$ generally indicates that the satellite is embedded within the host's density field, as already noted by Bullock et al. (2001). Thus, as a satellite gets closer to the central density region of the host halo, its overdensity peak becomes less contrasted. It is intrinsically harder to find satellites with low central densities under the standard paradigm of halo finding, especially close to the cuspy centre of the embedding host. It is not at all obvious how to disentangle the particle distribution of the satellite and the host halo: this is a fundamental limit to finding halos in the traditional way of observing over-densities and requires further investigation. In the next section, however, we introduce a method of finding halos that eliminates the background halo and, hence, minimises this problem.

The MHF method fails in the inner regions for two reasons. Firstly, because it is hard to detect the upturn in the density field, substructure is eliminated through suspected duplication of a halo because the substructure's radius has been falsely tracked out to essentially the virial radius of the host, its own upturn radius has been missed. The second reason results from a fundamental flaw in MHF's methodology - that the smaller satellite grids merge with the host's refinement grid and hence do not produce an isolated refinement. Therefore we are losing potential centres,

a problem illustrated further in Figure 3.4. There, we show the inner $250h^{-1}$ kpc of halo #1, along with the grids for the 7^{th} refinement level of `MLAPM` (gray-shaded areas) with the central refinement about $60h^{-1}$ kpc in radius. The dark spheres indicate the positions of satellites located by `MHF`. Note that those dark spheres that do not encompass an isolated refinement grid would do so at one of the next coarser (or finer) levels. The light sphere at the border of the ellipsoidal host refinement also surrounds a satellite galaxy. However, this object was *not* picked up by the `Finder` but rather by the `Tracker` outlined in the next section. `MHF` was unable to identify this satellite as an individual object as its refinement grid has merged with the host's grid, thus not allowing an isolated refinement and a potential centre, respectively. The straight line pointing to this satellite is simply its orbital path.

The problem can be viewed differently in Figure 3.5. Here we plot the density of the host halo at the position of a satellite against the maximum, central density of the satellite itself for redshift $z = 0$. The results are presented for the `Finder` (crosses) as well as for the `Tracker` (diamonds) to be introduced in Section 3.4. The line running through the plot for each individual host halo marks the 1:1 correspondence: satellites that fall onto (or even above) this line have central densities equal to (or smaller than) the host environment they are embedded within. We do observe a general (and reasonable) trend for satellites to have higher central densities than their dark matter vicinity. However, the figure also proves that the `Tracker` tends to also find satellites less contrasted and closer to the 1:1 relation, respectively. When interpreting Figure 3.5, and especially comparing the `Finder` to the `Tracker` results, one needs to bear two things in mind: firstly, there are many more `Tracker`-satellites obscuring a one-to-one comparison with `Finder`, and secondly, `Finder` relies on $r_{\texttt{MHF}}$ as the final point of the profile whereas `Tracker` has the ability to properly measure $r_{\rm vir}$. Minor differences in binning can also lead to very small changes in the central density calculation.

3.4 MHT: MLAPM's Halo Tracker

Conventional halo finders have a rich history in identifying isolated systems. In this regard, `MHF` might be viewed as simply an alternative approach to an already reasonably well-understood problem. To be fair though, `MHF` does push the conventional paradigm of simply using the three dimensional spatial data to locate the halos to

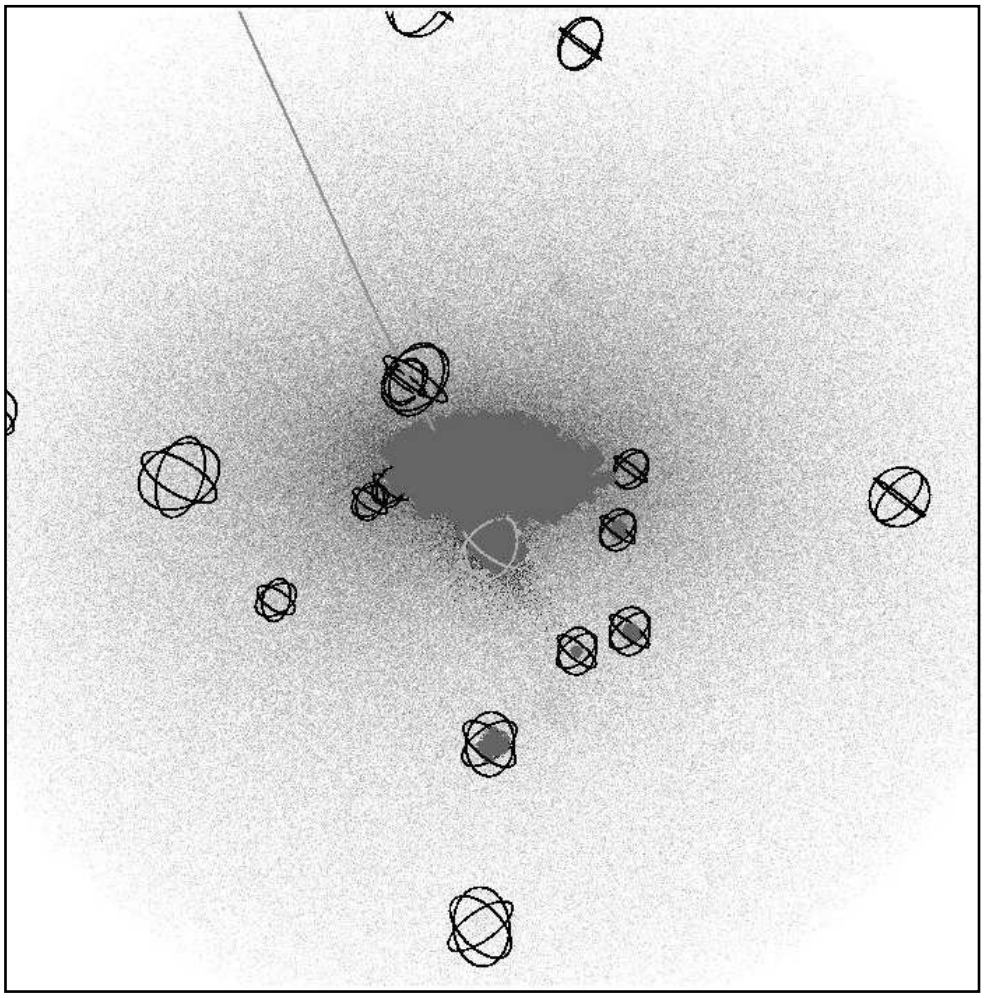

Figure 3.4: Limitaions of the MHF paradigm

The inner 250 h^{-1} kpc of halo #1 with the particles' line of sight density shown. We show the grids of the 7^{th} refinement level of MLAPM, with the central refinement about $60h^{-1}$ kpc in radius. The dark spheres represent the satellites located by MHF. The light sphere surrounds a satellite galaxy not found by MHF. The apparent sizes of the spheres are simply a visualisation effect as spheres farther away from the virtual observer appear smaller.

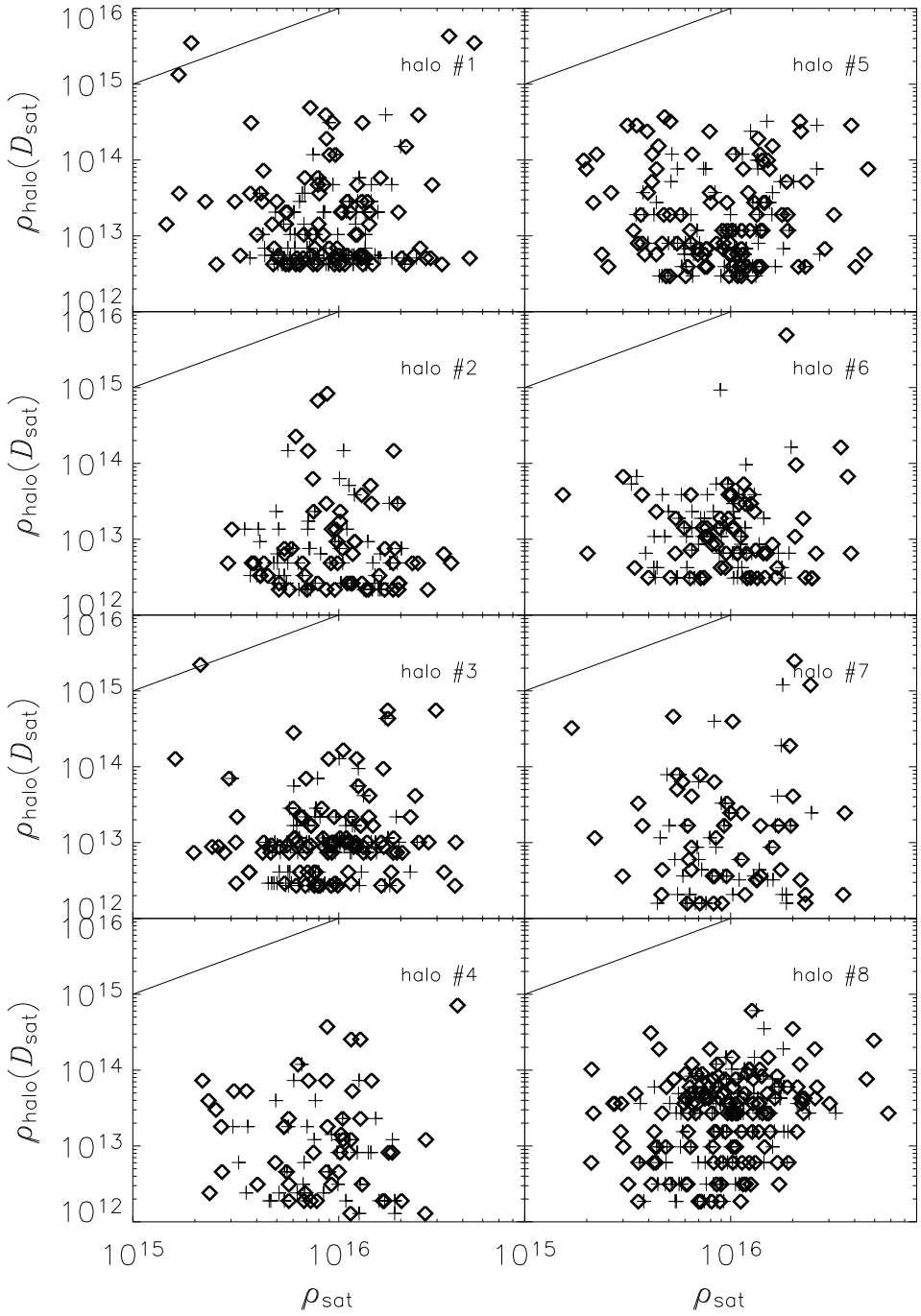

Figure 3.5: The density of the host halos verses the central density of the satellites. The density of the host halos at the radial distance $D_{\rm sat}$ of the satellite versus the central density of the satellites. The crosses represent the satellites found by `Finder` while the diamonds are the satellites found by `Tracker`.

the limit, locating the halos with (nearly) the exact accuracy of the N-body code. Having this ability, MHF becomes the ideal halo finder to locate substructure for MLAPM and no doubt an excellent halo finder for other codes. Although, as we have seen in Section 3.3, apart from numerical limitations in N-body codes (e.g. over-merging) there still remain limitations to our current halo finders. These limitations become a problem in the simulations when considering the substructure of any dense system, for example galaxy clusters and galaxies. Therefore, to successfully find the substructure we need to change the paradigm used to find it.

To successfully make this change we must first understand the environment in which we are finding the substructure and then exploit its characteristics. One characteristic is that most halos conserve their identities, that is substructure halos rarely undergo mergers in halos because of their high relative velocities (Ghigna et al. 1998; Okamoto & Habe 1999). Further, halos in dense environments undergo tidal stripping and substructure interactions, no longer accreting material, but being stripped of it. Thus in such environments it is sufficient to trace the particles of the satellite once the satellite has entered the host's virial radius. In this section we introduce MLAPM's-Halo-Tracer, MHT (or simply Tracker) hereafter.

MHT takes an arbitrary output of our new MLAPM-based halo finder MHF, and correlates the particles for an arbitrary number of time steps using all simulation outputs from that initial output until redshift $z = 0$. In our particular investigation it was appropriate to define that initial arbitrary output to be the formation time $z_{\rm form}$ of the host halo or the time when the host halo contained half of its present mass (Lacey & Cole 1994). We then followed all the satellites that were within two times the virial radius of the host halo at this formation time. Although, we miss a few satellites due to MHF's identification limitations in the inner 10-15% of the halo, from this time on MHT precisely follows the orbits of our initial set of satellites irrespective how close they come to the host's centre. An example of MHT in action can be seen in Figure 3.6 and in Figure 3.7.

In Figure 3.6 we see a tracked satellite galaxy (dark matter substructure). The line represents the satellite's orbit going from yellow (past) to magenta (now). From this figure we can see that the satellite initially fell into the host halo and has since undergone two full orbits and is coming back for a third. When we started tracking the satellite it was a gravitationally bound collection of particles, however, during its orbit the satellite has undergone significant tidal stripping, as is indicated by the stream of red particles. One interesting aside is that unlike the disruption of

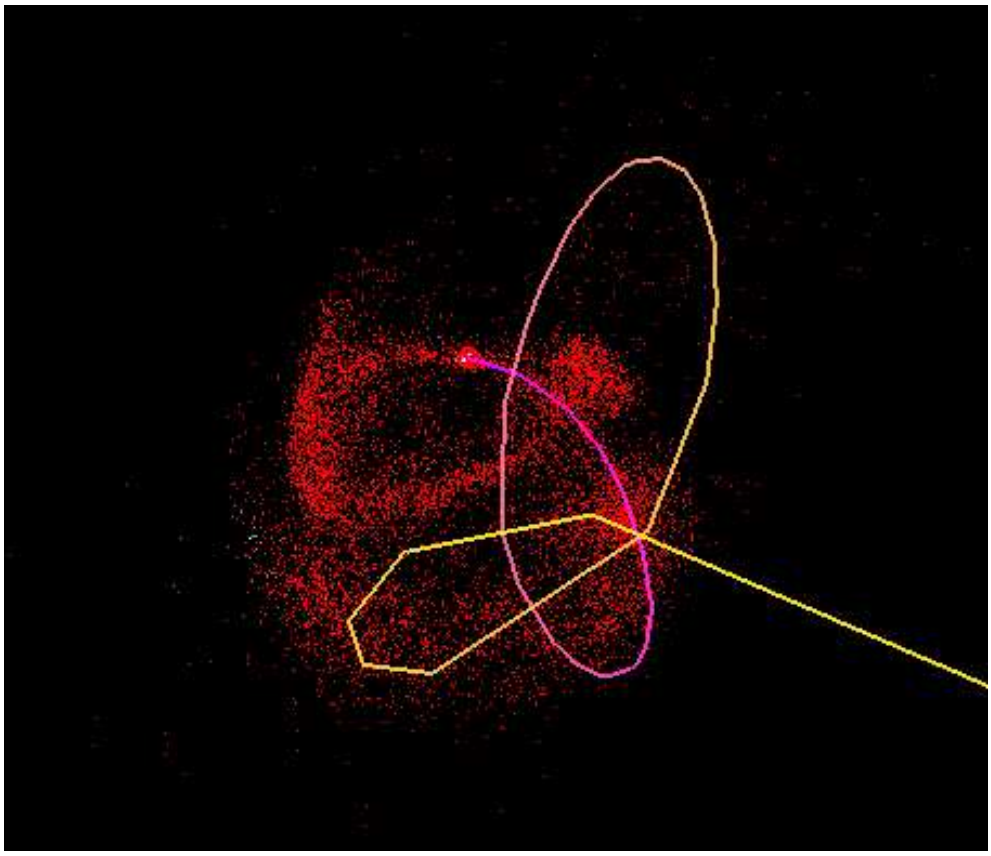

Figure 3.6: An example of a tracked satellite

a tracked satellite galaxy (dark matter substructure). The line represents the satellite's orbit going from yellow (past) to magenta (now). From this figure we can see that the satellite initially fell into the host halo and has since undergone two full orbits and is coming back for a third. When we started tracking the satellite it was a gravitationally bound collection of particles, however, during its orbit the satellite has undergone significant tidal stripping, as is indicated by the stream of red particles.

satellites within static analytical potentials where the satellite stream essentially follows the satellites orbit, the stream in this case is quite disrupted (This is further discussed in Chapter 7.

In Figure 3.7 we again see the disruption of a satellite within a dark matter host halo. The top image in this figure has the same format as figure 3.6 i.e. the orbit shown from yellow (past) to magenta (present). This satellite galaxy, however, has only undergone one complete orbit within the host halo. The position of this orbit with-respects-to the host halo can be seen in the next image down. In this image the line-of-sight projected density of the host halo is shown, however, we are only showing one in every sixteen particles. The final image shows the line-of-sight projected density for the satellite stream. It is interesting to see how the outer regions of the host halo have been built up from accreting satellites.

Explicitly, `MHT` takes the particles from an initial `MHF` analysis and then locates these particles in the next available output again. `Tracker`'s first task is then to (re-)calculate the halo's centre. This is done by using the centre-of-mass of the innermost 20 particles from the previous time step as an initial estimate, then using the same iterative method to check the credibility of the halo, as outlined in Section 3.2. Once the satellite was identified as bona fide the radial profile was generated, a NFW profile fitted, and other canonical properties calculated. The binning for the profile again used logarithmically spaced radial bins covering the entire particle distribution. The radius of the satellite was consistently determined as being the radius when the cumulative density profile dropped below $\rho_{\rm satellite}(r_{\rm vir}) = \Delta_{\rm vir}(z)\rho_b(z)$. This time we will not encounter the situation where the profile rises again as is the case for `Finder`; the satellite is no longer embedded within the "particle background" of the host halo but treated as a separated entity.

There are a number of advantages in tracing the halos in this way - first, because we are tracking just the satellites' individual particles we do not have the complication of the background density distribution and the consequent lack of contrast against the host system for all outputs $z < z_{\rm form}$. Following from this, we do not have to accept the truncation radius - the radius where the `Finder` encounters and upturn in the density profile - as the "natural" radius of the satellite. Further, this method allows us to investigate the development of tidal streams, as seen in Figure 3.6 and further elaborated on in Chapter 7.

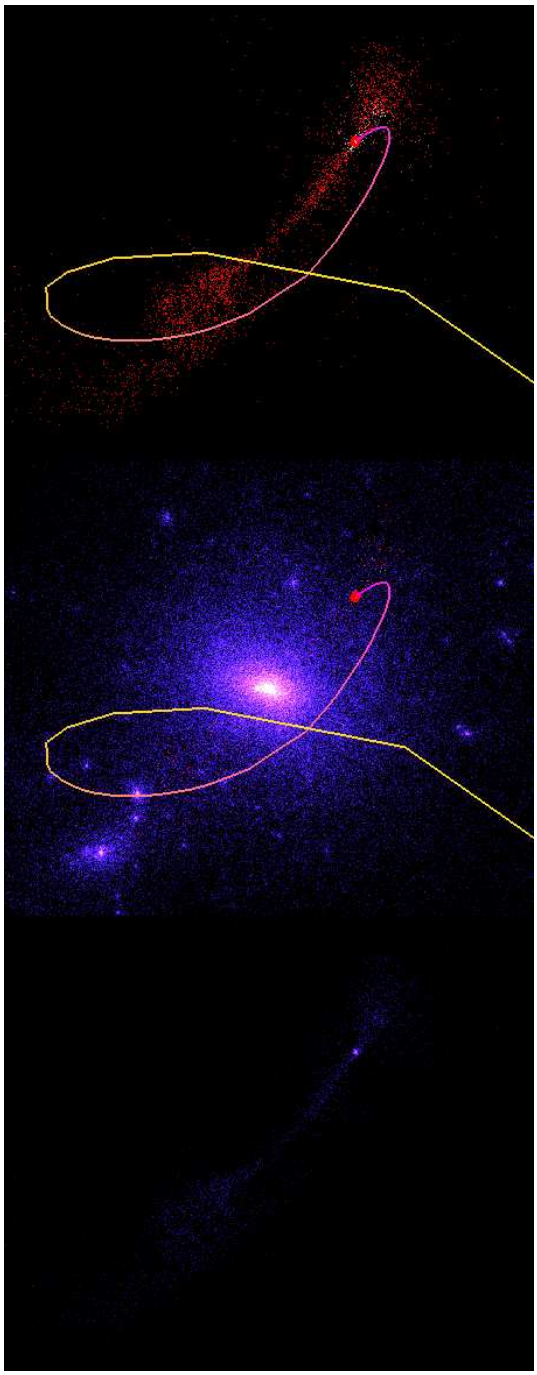

Figure 3.7: A series of images showing a disrupted satellite and its relation to the host halo.
In the top image we se that satellite galaxy, has undergone one complete orbit within the host halo. The position of this orbit with-respects-to the host halo can be seen in the middle image. In this image the line-of-sight projected density of the host halo is shown (showing 1 in every 16 particles). The final image shows the line-of-sight projected density for the satellite stream.

3.5 Analysis of MHT halos

The nature of hierarchical structure formation, i.e. mergers, dynamical and tidal destruction of substructure, requires us to work harder when applying MHT to our simulation data. Even though were are now tracing the initially bound particles forward in time, we need a criterion to decide whether a satellite galaxy is disrupted or still alive. We therefore introduce the tidal radius as given below.

3.5.1 Tidal Radius

The tidal radius is defined to be the radius of the satellite where the gravitational effects of the host halo are greater than the self-gravity of the satellite. When approximating the host halo and the satellite as point masses and maintaining that the mean density within the satellite has to be three times the mean density of the host halo within the satellites distance D to the host halo (Jacobi limit) the definition for tidal radius reads as follows

$$r_{\text{tidal}} = \left(\frac{m}{3M}\right)^{\frac{1}{3}} D \ , \tag{3.3}$$

where m is the mass of the satellite and $M = M(< D)$ is the mass of the host halo internal to the distance D.

In order to stabilise the determination of the tidal radius r_{tidal} we actually use an iterative procedure again. By defining the satellite mass m as the mass internal to r_{tidal}, i.e. $m = m(< r_{\text{tidal}})$, we find r_{tidal} by solving

$$r_{\text{tidal}} - \left(\frac{m(< r_{\text{tidal}})}{3M}\right)^3 D = 0 \ . \tag{3.4}$$

Starting with the distance of the furthest particle in the satellite particle distribution as the initial guess for r_{tidal}, the method quickly converges in two-to-three iterations.

3.5.2 Satellite Disruption

As the satellites orbit within the host halo they undergo tidal stripping, hence, the satellites are gradually losing mass. Therefore, their particle distribution becomes more and more diffuse, reducing the tidal radius of the satellite. Eventually there comes a point when the satellite loses sufficient mass that we begin to reach the limits of our numerical resolution, not having sufficient number of particles to follow

the satellite further. The satellite might have survived for longer, however, we do not have the resolution to follow it. Thus when a satellite passes through our numerical limit we tag it "disrupted". In practice this means that if there are fewer than 15 particles within the tidal radius we classify the satellite as being disrupted. Note that we are unable to separate numerical resolution disruption and real physical disruption of a satellite. It is not clear if we had infinite mass resolution that the satellite would still actually survive.

We also stress that since our tidal radius formulae assumes circular orbits, the usual D corresponds to the pericentric distance (Hayashi et al. 2003); however, we calculate $r_{\rm tidal}$ for each satellite at each individual output to check for (tidal) disruption.

Furthermore, particles outside the tidal radius are not automatically stripped from the halo - what is just as important is the time spent under the influence of that tidal field, it still takes time for the particle to climb out of the potential. For example a satellite might be on a very eccentric orbit and pass close to the centre of the host halo, thus having a very small tidal radius at the pericentre. Now it is true that most of the tidal stripping will occur at this pericentre, however, because the satellite only spends a short time there not all the particles outside the tidal radius will be stripped.

3.5.3 Orbital Information

In future chapters we present a detailed analysis of the satellites' orbits, we now introduce the terminology relevant to that discussion. The high temporal resolution of our simulations ($\Delta t = 0.17$ and $\Delta t = 0.35$ Gyrs, respectively, for $z > 0.5$ and $z < 0.5$) enables us to track in detail the orbits of the satellites. As an example, in Figure 3.8 we show the orbit of one particular satellite. We can see that this satellite initially plunged in from outside the virial radius at $z = 0.8$ and was subsequently captured by the host, undergoing two further orbits prior to $z = 0$. This orbital information was then used to construct a measure of eccentricity

$$\epsilon = 1 - \frac{p}{a} \tag{3.5}$$

where p is the most recent "closest" distance to the host's centre as a minima (labelled `peri` in Figure 3.8) and a the most recent "furthest" distance (labelled `apo`) as a maxima. Moreover, we are also in the position to calculate the number of

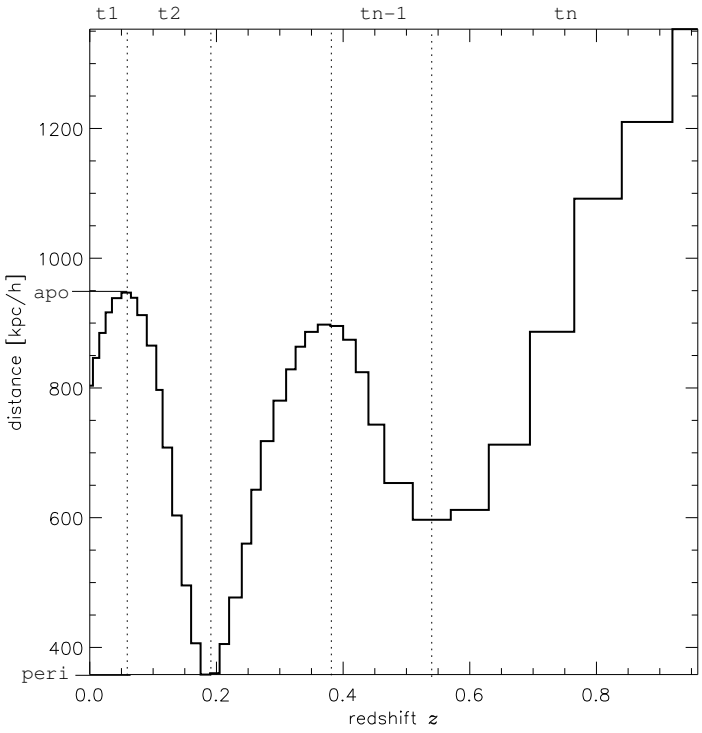

Figure 3.8: Satellite orbital details

Distance from the center of the host halo in real co-ordinate system as a function of redshift for one particular satellite with ($M_{\rm sat}/M_{\rm host} = 0.7 \times 10^{-2}$).

orbits from the time evolution of the distance to the host centre. To this extent, we simply count the number of extrema (four in the case shown) and divide by two. We further correct for incomplete orbits at the beginning and end points of the distance relation, resulting in the following formula for the total number orbits:

$$N_{\rm orbits} = \frac{N_{\rm extrema}}{2} + \min(\frac{1}{2}, \frac{t_1}{t_2}) + \min(\frac{1}{2}, \frac{t_n}{t_{n-1}}) \tag{3.6}$$

The number of orbits measured by that method for the sample satellite presented in Figure 3.8 is $N_{\rm orbits} = 2.69$.

We emphasise though that the orbits of the satellites are not always as aesthetically "smooth" as that for the one presented in Figure 3.8. We are dealing here with live potentials and hundreds of satellites orbiting within it simultaneously. The host halo is constantly growing in mass and shows internal oscillations in shape due to ongoing mergers. This has has an impact on the orbital evolution of the satellites, as described in the next chapter.

3.5.4 The radial distribution of satellites

In Figure 3.3 we showed the radial distribution of satellites for `MHF`. We now present in Figure 3.9 the same plot for `MHT` highlighting the superiority of the `Tracker`. Once again we observe the similarity in the slopes across the eight halos, a so-called "universal satellite distribution". However, the important result is that using the `Tracker` we now find (more) objects within the central 10% of $r_{\rm vir}$ of the host halos. For halo #1, for instance, we located 5 satellites with mass greater that $10^{10}h^{-1}$ $\mathrm{M}_{\odot}$ within 10% of the virial radius with the closest satellite at $z = 0$ being a mere $35h^{-1}$ kpc away from the host's centre.

To allow a more natural comparison to work published by other authors, we present the data in a slightly different fashion in Figure 3.10. This time the radial number density of satellite galaxies is shown. As with Ghigna et al. (2000) and De Lucia et al. (2003) we also find that the sub-halo population is "anti-biased" relative to the dark matter distribution in the inner regions of the halos. Moreover, we again observe no trend with environment for the sample of eight halos under investigation; all halos, irrespective of age and richness, do show the same anti-bias in the satellite distribution.

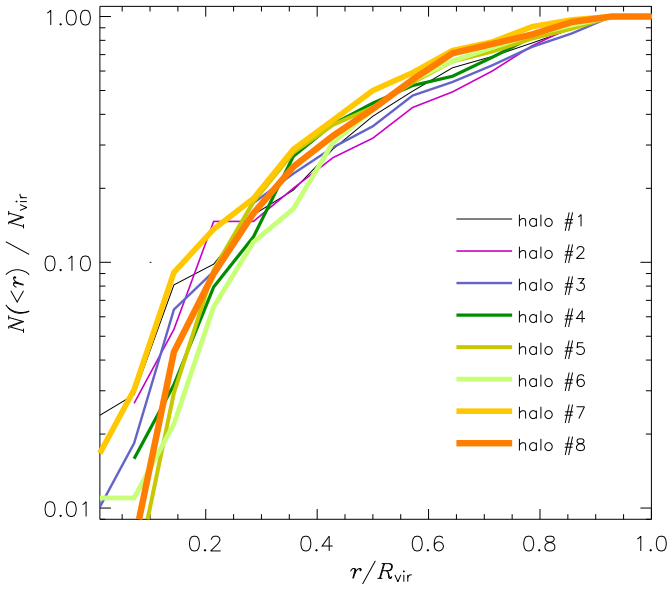

Figure 3.9: Radial distribution of satellites: `MHT`
Number of satellites within a particular radius normalised by the total number of satellites as a function of radius normalised by the virial radius at $z = 0$. Only satellites more massive than $2 \times 10^{10} h^{-1}$ $M_\odot$ were taken into account.

3.6 Comparison to other halo finders

In this section we compare `MHF` and `MHT` to two other halo finders, namely SKID and FOF. In Figure 3.11 we present a visual comparison of the effectiveness of the respective halo finders. Firstly, the top two panels show the line of sight density projection of particles for halo #1 within a $700h^{-1}$ kpc sphere. The left panel displays all the particles, while the right panel only shows every third particle. In the remaining four panels, we present the results of the halo finding algorithms: (reading clockwise, starting upper left) `MHT`, SKID, FOF, and `MHF`. A sphere of fixed radius $20h^{-1}$ kpc surrounds each located satellite where different apparent sizes are simply visualisation effects, i.e. spheres farther away from the virtual observer appear smaller.

SKID was run with multiple linking lengths and the option to remove gravitationally unbound particles enforced.[3] Under close visual inspection, the best SKID results were found with linking lengths b=0.03 & b=0.05 times the interparticle sep-

[3]For a detailed description of SKID please refer to
`http://www-hpcc.astro.washington.edu/tools/skid.html`.

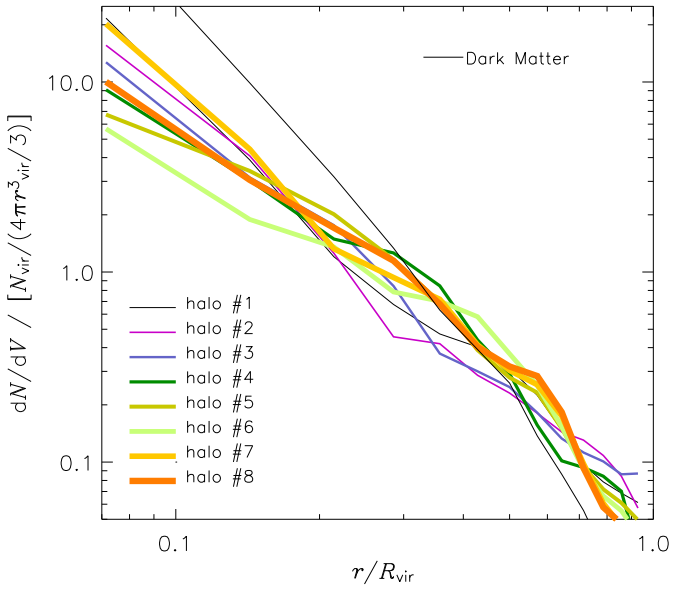

Figure 3.10: Radial number density of satellites
Number density of satellites normalised by the average number of satellites per unit volume as a function of radius normalised by the virial radius at $z = 0$. Only satellites more massive than $2 \times 10^{10} h^{-1}$ $M_{\odot}$were taken into account.

aration. The same values were taken for the FOF analysis. The results from the analysis with linking length b=0.05[4] appear to be the most reliable ones and hence are shown in Figure 3.11. We need to stress though that the analysis of the SKID and FOF results can be further refined by combining various halo catalogues into a tree as explained in, for instance, Ghigna et al. (2000). However, one of the benefits our `MLAPM` halo finders is that neither requires any further input such as a linking length or any other free parameter. Moreover, the latest version of `MLAPM` is capable of performing the analysis "on-the-fly". A visual inspection of Figure 3.11 indicates that `MHT` provides the most complete halo list. Specifically, the `Tracker` found 53 satellites, the `Finder` found 32, SKID 33 and FOF 32 within the plotted spherical region of diameter $1.4h^{-1}$ Mpc when restricting the analysis to objects with more than 100 particles. Within the sets of satellites, there is of course considerable overlap. Essentially, each set of satellites found by `MHF` SKID, and FOF were subsets of `MHT`. However, both SKID and FOF had halos that were spurious where this was not

[4]A linking length of b=0.05 expressed in terms of the interparticle separation translates into a physical linking length of $\sim 6h^{-1}$ kpc, which is roughly three times the force resolution.

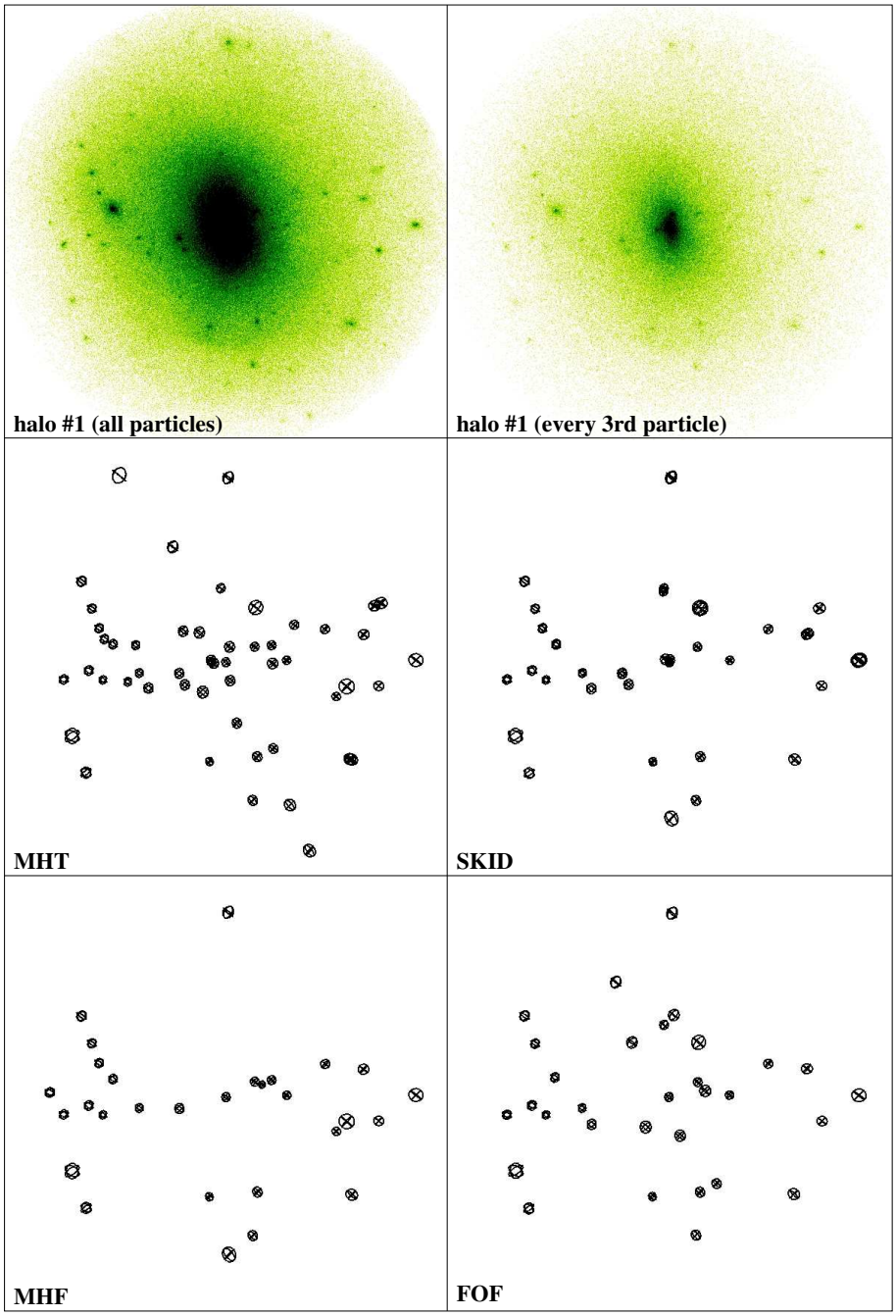

Figure 3.11: Halo finder comparison: visual comparison
The top two panels show the line of sight density projection of particles for halo #1. The left panel displays all the particles, while the right panel shows every third particle. The remaining four panels show the results of the halo finding algorithms: `MHT`, SKID, FOF, and `MHF` (clockwise from top left). A sphere of fixed radius $20h^{-1}$ kpc surrounds each satellite.

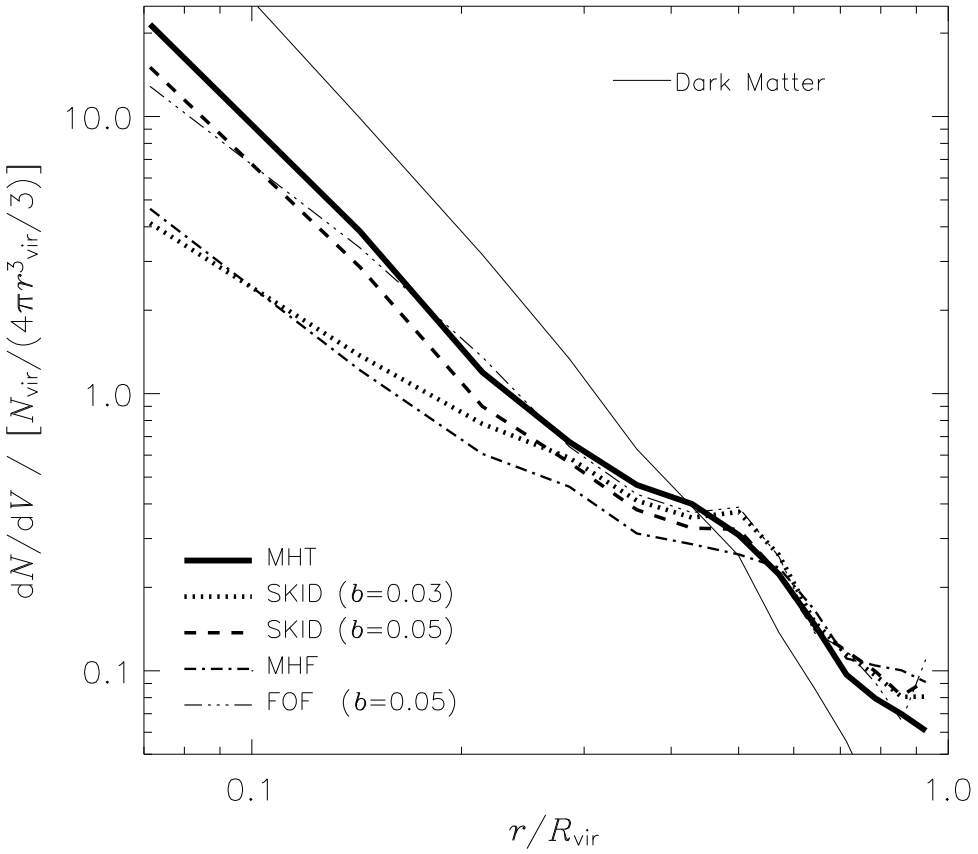

Figure 3.12: Halo finder comparison: radial number density
Number density of satellites normalised by the average number of satellites per unit volume as a function of radius normalised by the virial radius at $z = 0$, halo #1 for each of the halo finding algorithms: `MHT`, SKID, `MHF`, FOF. Only satellites more massive than $2 \times 10^{10} h^{-1}$ $M_{\odot}$were taken into account.

the case with MHT and MHF. To look at this quantitatively, we calculate the radial number density of satellites for all four halo finders again (cf. Figure 3.10). This time we concentrate on halo #1 highlighting the differences between the halo finding methods. The result is presented in Figure 3.12 which clearly shows the success of the Tracker over all other methods. However, it is interesting to note that a simple FOF analysis gives quantitatively similar results to the more sophisticated SKID data. The difference between the Finder and the Tracker is quite remarkable, as is the similarity between MHF and SKID with b=0.03. Our explanation for the lack of substructure in the central region for this particular SKID analysis is that these objects where either removed because of our lower mass cut of 100 particles or the fact that SKID did not classify them as gravitationally bound. What we can also learn from Figure 3.12 is that the sensitivity of the halo finder in the inner regions can severely bias the results. For example using MHF or SKID with b=0.03 provides a much stronger anti-bias in the satellite distribution than the more appropriate Tracker and SKID (b=0.05) analysis, respectively.

We like to the close the comparison by coming re-examining Figure 3.5, this time including the results from the SKID (b=0.05) analysis. The result for halo #1 can be viewed in Figure 3.13. We still observe that *only* the Tracker is capable of resolving satellites with central densities close to the (local) density of the host halo. We also inspected the situation for the FOF (b=0.05) data and could not find any significant difference and hence decided to not plot the data for clarity.

3.7 MHF evolution

The following section outlines the evolution of the MLAPM halo finder. It is important to stress that the updated Finder (explained below) was not used in the thesis analysis rather the finder as descried in previous sections was.

The primary desire to make changes to the Finder where twofold. First, in its original incarnation the Finder was a set of independent codes, thus for the simplicity of the user it was desirable to have only one (essentially) parameter free piece of software fully integrated with the already existing software package MLAPM. The second motivation was to re-address the method by which the Finder gathered the particles associated with the dark matter halos. We will now explain this new method for gathering the particles.

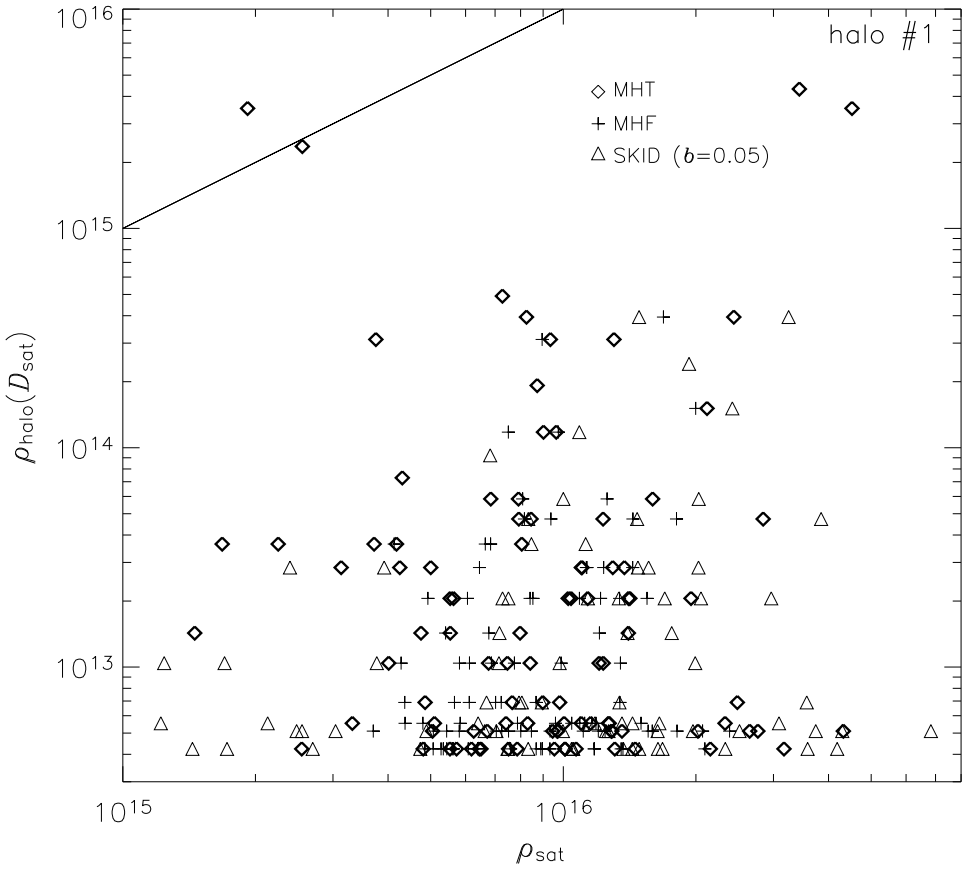

Figure 3.13: Halo finder comparison: central densities
Same as Figure 3.5, but this time comparing `Tracker` (diamonds) and `Finder` (crosses) with the SKID, b=0.05 (triangles) analysis for halo #1.

The central idea behind this new method for gathering halo particles is based on the fact that when a cell is refined, the particles that are responsible of the refinement of the cell are linked to that cell. Thus the particles are uniquely associated with the cells and hence grids. Therefore, one can essentially "cut" of each of the branches of the reconstructed "grid tree" and gather all the particles that are associated with that branch/sub-halo.

However, when we cut the branches off in this manor we are only collecting the particles associated with the sub-halo that are above the localised density of the parent branch where the sub-halo is located. While this is fine for isolated halos (which are cut at the virial density) for sub-halos it is less clear how to cut the branch off.

Cutting sub-halos of at their branch density is essentially equivalent to collecting the particles of the halo out to the upturn radius of the sub-halo (i.e. the radius at which the background density begins to rise again). Although we have seen that sub-halos sink within their host halo i.e. beyond this upturn radius (density cut) there are particles still bound to the halos. To circumvent this difficulty we also collect all the particles from the parent branch that are within half the distance to the next closest more massive branch. We chose the next most massive branch because it gives as an adaptive gathering radius, which is sensitive to the nature sub-halos i.e. sub-halos are by definition smaller than their hosts. Further we gather particles not simply from their immediate host branch (halo), but also from the host of their host etc. if required.

Once we have done this we proceed to remove gravitationally unbound particles. If a particle is found to be unbound we pass it to the host halo. The unbound procedure is ordered in such a way that the smallest sub-(n)-sub-halos are checked first for unbound particles.

Finally with the halo centres and the particles that belong to those halos gathered we calculate the same canonical properties of the dark matter halos as previously described.

The most significant difference between the previous `Finder` version and this one is the way the particles are gathered. Previously the particles where simply gathered in radial shells and each particle was not uniquely identified with a halo. In this new method none of the particles are double counted because each particle is uniquely assigned to a node.

The end result of the new `Finder` can be seen in Figure 3.14.

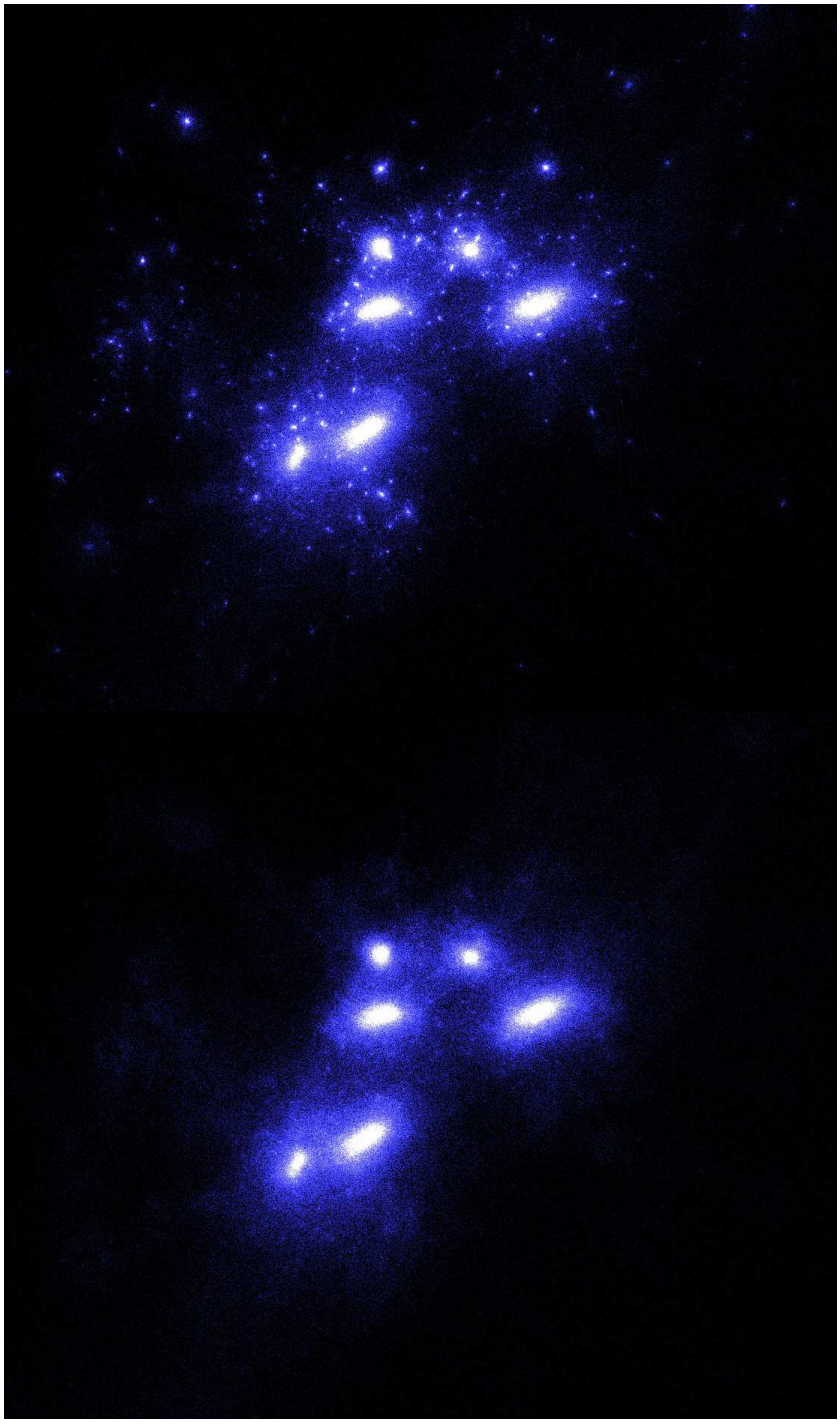

Figure 3.14: The "new" halo finder
This figure shows the line-of-sight density projection of a halo early in its formation. In the top panel you can see the abundance of substructure. In the bottom panel however, the smaller substructure has been removed using the "new" `MLAPM` halo finder.

The precise details of the halo finding story, which is a story of carefully structured memory structures and complicated pointer arithmetic (this detailed story was considered to terse for the reader) can be found by downloading the `MLAPM` source and reading the detailed comments in the files ahf_gridinfo.c & ahf_halos.c.

3.8 Conclusions

Computational cosmology is not only limited by crucial factors such as the dynamical range and the mass resolution, but also by its analysis tools. We emphasise, perhaps obviously to most readers, that N-body codes simulating structure formation in the Universe can only ever be as useful as their associated analysis tools allow.

In this chapter we presented two new methods for identifying gravitationally bound objects in such simulations. Both methods are based upon the open source adaptive mesh refinement code `MLAPM` (Knebe et al. 2001). They both exploit the refinement hierarchy of said code and hence locate halos as well as halos-within-halos with exactly the same accuracy as `MLAPM` simulates their evolution. We showed the limitations of a simple snapshot analysis and how it can be overcome by taking into account the whole history of each halo. Thus not restricting the halo finding algorithm to just the spatial information but rather including the velocity information as well, hence, using the full six-dimensional information available.

We showed that halo finding still possesses the inherent problem of overmerging in the very central regions of the host. However, by tracking satellites rather than identifying them at separate time snapshots of the simulation we learned that this problem is *not* overmerging in the conventional sense. The objects are in fact present and simulated properly, but their densities have insufficient contrast to be picked up by a simple "finder". Only when tracking them in time from (at best their very own) formation time were we able to quantify their existence as close as 5% of $r_{\rm vir}^{\rm host}$ to the cuspy centre. We do not intend to question the credibility of other (most excellent) halo finders such as SKID though. We rather pointed out that the results in the central region are subject to subtleties that can be most easily avoided by tracking satellites.

It has recently been pointed out by Taylor et al. (2003) that the radial distribution of the Milky Way's satellite galaxies does not reconcile with the predictions of semi-analytical models of galaxy formation and cosmological simulations, respec-

tively, which has been confirmed by Kravtsov et al. (2004). Even though there is quite a prominent substructure population in the simulations it is mostly clustered in the outer regions of the host whereas the Milky Way satellites are preferentially found closer in. It remains unclear if this poses a new challenge to the CDM structure formation scenario or simply reflects what we presented in this study. Namely, identifying substructure halos that lie close to the centre of the host is intrinsically challenging and might be overcome by actually *tracking* the satellites rather than *finding* them.

We further increase the statistics to suggest that anti-bias of the satellite distribution is a common property of the satellite distribution, perhaps even universal. However, this antibias is still most likely a relic of numerical overmerging. A convergence study for the satellite populations is critical in resolving this issue and reconciling the lensing observations. However, one very interesting result is the continued self-similarity in the dark matter distribution, the satellite radial distribution is common, once again perhaps “”universal” even though the number of substructure satellites changes, reminiscent of the universal density profile of the underlying host.

Finally, we updated the development of the `MHF` a quicker and cleaner implementation that is open source.

Chapter 4

The dynamics of substructure

"The dynamics of capitalism is postponement of enjoyment to the constantly postponed future."

- Norman O. Brown

4.1 Introduction

As we have seen within CDM structure forms hierarchically, whereby small objects (sub-halos) form first and subsequently merge to progressively form larger objects (White & Reese 1978; Davis et al. 1985). Thus the dynamical properties of the accreting sub-halos reflect the formation of the underlying host. Hence, it is imperative to understand the orbital evolution of these objects and how they deviate from the background dark matter distribution. The first few chapters of this thesis introduced the tools for investigating these sub-halos, we now investigate the general properties of these accreting sub-halos analysing in detail their temporal and spatial properties.

To date, typical sub-halos (satellite) properties such as orbital parameters and mass loss due to tidal interactions with their host halo have primarily been investigated using *static* potentials for the dark matter host halo (e.g. Johnston et al. 1996; Hayashi et al. 2003). We stress that each of these studies have provided invaluable insights into the physical processes involved in satellite disruption; our goal is, however, to augment these studies by relaxing the assumption of a static host potential, in deference to the fact that realistic dark matter halos are not necessarily axis-symmetric or time independent. As we saw in Chapter 2 halos are constantly

growing in mass through slow accretion and violent mergers, varying in dynamical relaxation and possessing triaxial shapes.

While a self-consistent cosmological modelling of both hosts and satellites has long been recognised as optimal, the required mass and force resolution can be difficult to accommodate due to computational costs, hence the use of static host potentials in most previous studies.

The first fully self-consistent simulations targeting the subject were performed by Tormen (1997) and Tormen et al. (1998). Both studies were landmark efforts, but lacked the temporal, spatial, and mass resolution necessary to explore a wide range of environmental effects. Unable to follow the satellite distribution within the host's virial radius, satellites were instead tracked only up to and including the point of "accretion". This allowed an analysis of the in-fall pattern, rather than the orbital evolution of the satellites. Ghigna et al. (1998) also investigated the dynamics of satellite galaxies in live dark matter host halos. Although greatly increasing the mass and spatial resolution, they still lacked the temporal resolution to explicitly track the satellite orbits. Instead, the orbits were approximated using a spherical static potential. More recently, Taffoni et al. (2003) used N-body simulations coupled with semi-analytical tools to explore the evolution of dark matter satellites inside more massive halos. However, they focus their efforts on the interplay between dynamical friction and tidal mass loss in determining the final fate of the satellites.

As we have seen in previous chapters our suite of simulations has the required resolution to follow the satellites even within the very central regions of the host potential ($\geq$5–10% of the virial radius) and the time resolution to resolve the satellite dynamics with excellent accuracy ($\Delta t \approx$170 Myrs). Hence, we have excellent data possessing high spatial, mass, *and* temporal resolution which uniquely enables us to investigate the evolution of sub-halos and their relation to their Hosts.

The outline of the chapter is as follows. In the first section we continue our analysis from the previous chapter, investigating now the satellite populations of the host halos and investigate their global properties such as total mass. In Section 4.3 we discuss the internal structure of the satellites. In Section 4.4 we take a detailed look at the satellite orbital parameters. We then investigate the kinematic properties of the dark matter halos and satellites in Section 4.5 and finish with our summary and conclusions in Section 4.6.

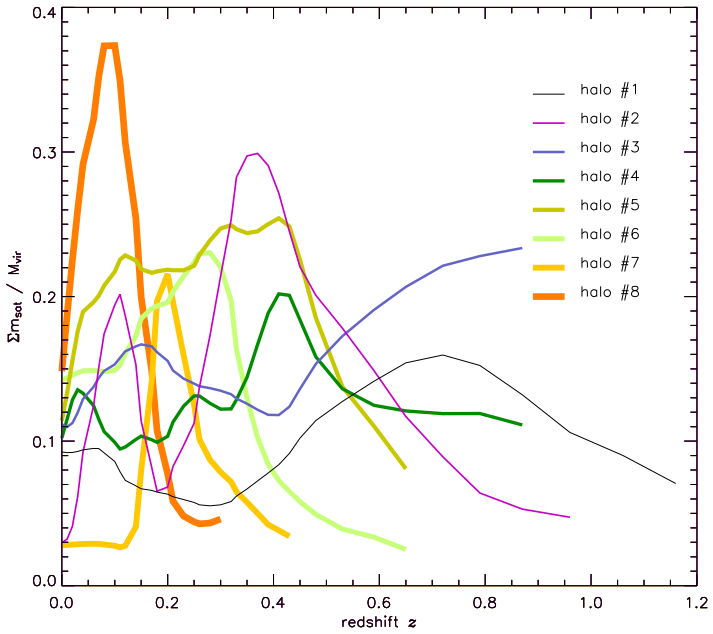

Figure 4.1: Mass locked-up in substructure
Mass locked-up in satellites within the virial radius divided by the virial mass of the host halo as a function of redshift.

4.2 Satellite Properties

4.2.1 Satellite Mass History

To gain further insight into the hierarchical build-up of the host and the evolution of its satellite population we plot the fraction of its mass locked up in the satellite distribution in Figure 4.1. We show the total mass of all the satellites (identified by the `MHT` method) living within the virial radius divided by the mass of the host halo as a function of redshift.

At $z = 0$ the average mass of all substructure is approximately 8–9% of the host halo's virial mass with the scatter allowing for as much as 15% and as little as 3%. We do not observe any pronounced trend for this fraction to depend on the age of the dark matter halo, which is consistent with the hierarchical model of satellite accretion: both small and large objects continuously fall in. The history is clearly reflected in Figure 4.1 which shows the amount of mass locked-up in satellites normalised by the virial mass of the host halo as a function of redshift. In this figure the infall of large satellites gives rise to the spiky nature of the curves.

These large variations are, however, a combination of massive halos merging via dynamical friction and "transitory structures". Transitory structures are a subsets of satellites that interact with a halo, but are not bound to it. An example is given in Figure 4.2 where we show one of these transitory events for halo #7. The peak near redshift $z = 0.2$ for this halo in Figure 4.1 is caused by an object of roughly 10% of the mass of the host orbiting in the outskirts (but still within $R_{\rm vir}$) of the host halo at a relative speed of approximately 750 km s^{-1}. Figure 4.2 captures this event showing the host and its virial radius at redshift $z = 0$ with the path of the satellite indicated by a line. The perturber itself is represented by its particles. Its tidal disruption while passing near the host can also be appreciated in Figure 4.2. We particularly highlight this encounter not only to explain the observed rise in Figure 4.1 but also to raise the readers attention to the potential of already "harassed" galaxies falling into the host halo. The particulars and nature of these objects will be postponed to a more detailed discussion in Chapter 6. The large peak for halo #8 in Figure 4.1 is due to an interaction with one of the other two large objects in the system. The violent history of halos #5 and #6 can also be seen in Figure 4.1. The more quiescent halos also stand out in this figure, with less variation in the substructure evolution except for halo #2 with a 15% mass merger at $z = 0.53$.

In summary, we have selected a sample of halos displaying widely different formation histories, which should aid in gaining insight into the environmental effects of halo formation.

4.2.2 The Supply of Satellites

We now investigate the temporal evolution of satellite accretion and tidal disruption as a function of host halo environment and richness.

In Figure 4.3 we display the normalised number of satellites within the respective host halo as a function of time after the initial formation epoch. As we intend to measure "supply rates" rather than absolute numbers of in-falling satellites we normalise the curves by the number of satellites present at the formation time of the host halo. The thin line represents the total normalised number of satellites which have been accreted, while the thick line refers to the number of *surviving* satellites. The criterion used to define tidal disruption is the reduction in the number of particles within a given satellite's tidal radius to fewer than 15. This definition is

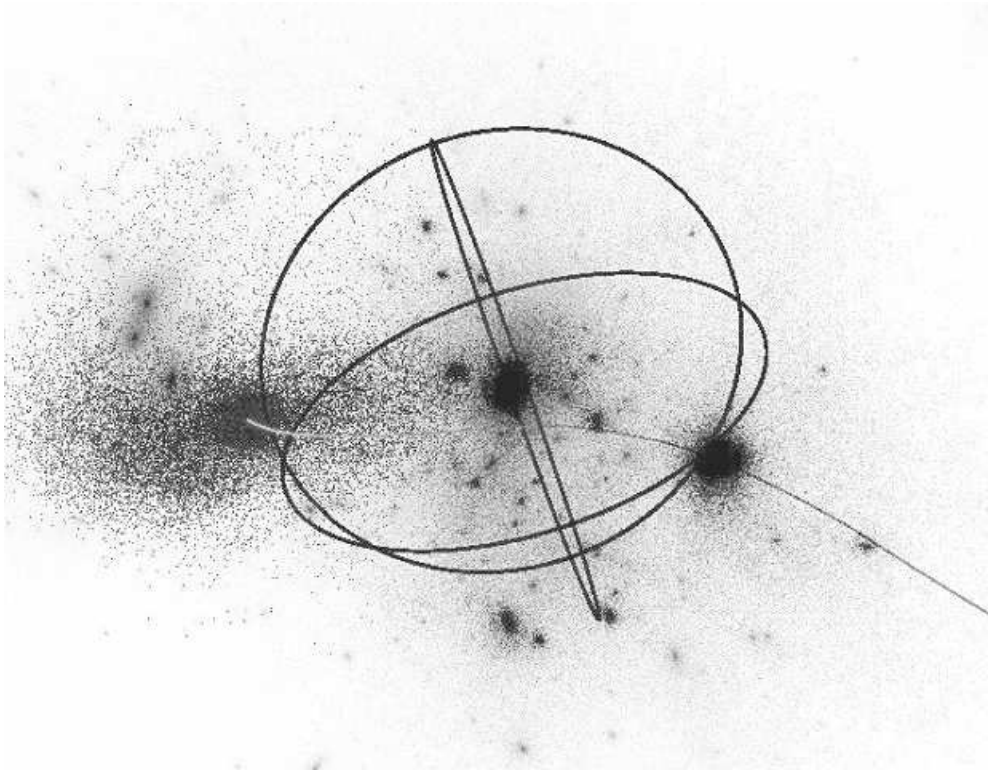

Figure 4.2: Backsplash galaxy

This figure shows a satellite of mass 10% the host halo that is responsible for the jump in the host's mass accretion history. The host halo (halo # 7) is plotted as a line of sight density projection using every $3^{\rm rd}$ particle, whereas the satellite is represented by all its particles without a density map. The satellite enters the halo at $z = 0.25$ (lower right) and leaves again around $z = 0$ with the thin line indicating its orbit. The sphere shows the virial radius of the halo at $z = 0$ and the relative velocities of the two objects is 750 km s^{-1}.

somewhat arbitrary, although ultimately based upon the numerical resolution. For a more detailed discussion please refer to the previous chapter.

The increase in the total number of satellites (thin curve) reflects the "richness" of the environment around the halo: halos with a steep slope benefit from a constant supply of satellite galaxies where as hosts that only show a mild increase draw upon a pool of fewer satellites in their immediate vicinity. This is illustrated by the case of halo #1 which lies in a particularly rich environment in which several filaments intersect (cf. Figure 4.4). As a consequence, it accretes a total of nearly five times the initial number of satellites while simultaneously showing a high satellite disruption rate. The case of halo #3 is similar, but less extreme. Halos #7 and #8, by contrast, experience only moderate in-fall, and in these halos nearly all the satellites survive. The situation is illustrated for halos #1 and #8 in Figure 4.4 & 4.5 respectively, which shows the orbital paths followed by all the satellites from the formation epoch up to the present day. In Figure 4.4 we clearly see the filament "arms" that feed halo #1 and how the satellites spiral into the dark matter halo. The filaments are helical because they consist of smaller satellites orbiting a larger host that is falling into the massive host halo. The small but rapid rise in the satellite in-fall for halo #1 (Figure 4.3) is caused by a group of satellites falling into the halo for the first time. In Figure 4.5 we feature halo #8; in contrast to halo #1, halo #8 was formed in a relatively isolated region which saw a rapid collapse. We can, however, confirm that even though the satellite accretion rate in halo #8 is far less the mass of the infalling objects is much higher. This is derived from the fact that halo #8 acquires half its mass by digesting those few satellites in a time span of approximately 3 Gyrs (cf. Figure 4.1). We note though that there also exists a significant age difference between halo #1 and #8; this explains why halo #8 satellites are traced for a shorter time leading to the "shorter" lines in Figure **??**. However, there still exist noticeable differences in the satellite accretion curves for halos #1 and #8 (cf. Figure 4.3) when restricting halo #1 to the first 3.5 Gyrs of its existence.

We define the substructure "richness" as the ratio of the final to initial number of satellites, and list its value for each of the eight halos in Table 4.1.

The number of surviving satellites is not directly correlated with the richness, but rather to the orbital characteristics of the accreted satellites, as we will demonstrate in detail below. In general, the accreted satellites are not immediately disrupted, but are progressively destroyed over time.

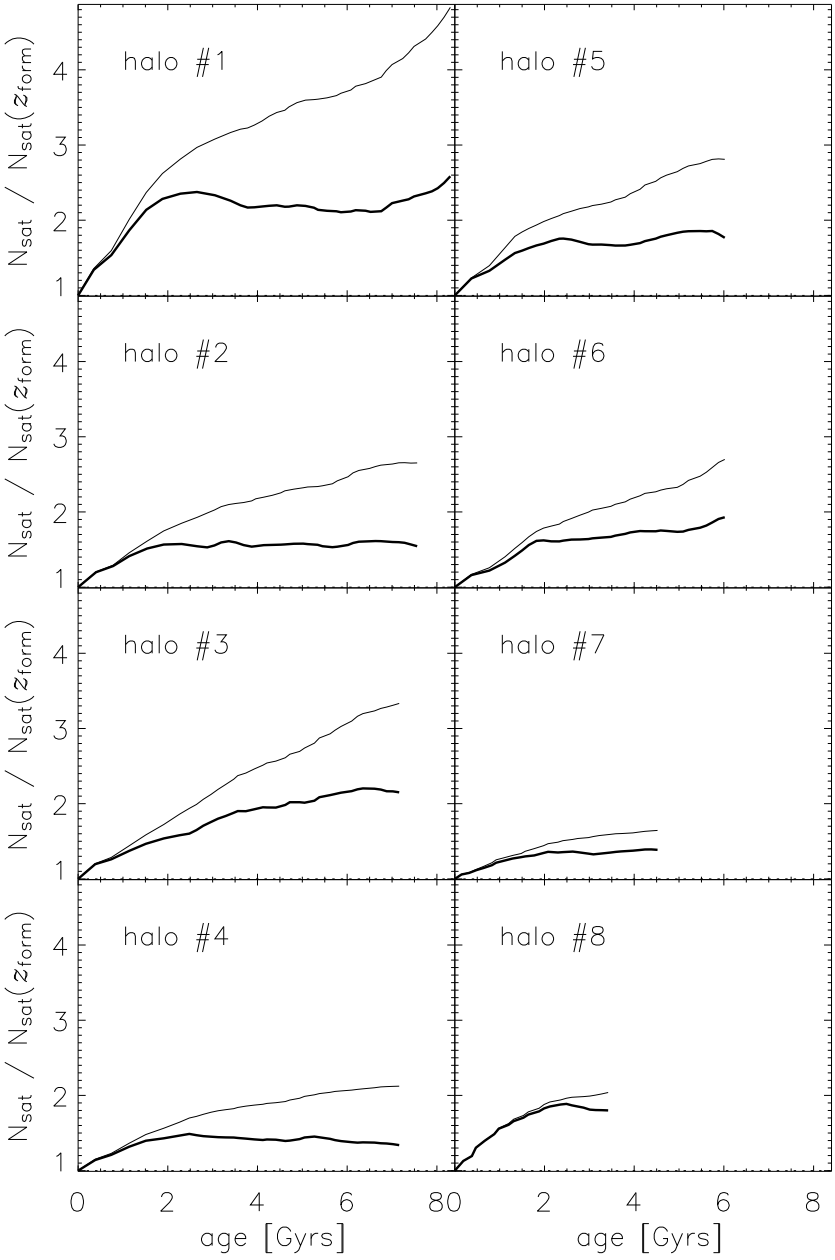

Figure 4.3: Number of satellites within the virial radius as a function of redshift Number of satellites within the virial radius of their respective host as a function of redshift. The thin line is the total number of satellites that have fallen into the host whereas the thick line shows the number of surviving satellites. Both lines are normalised to the total number of satellites at $z_{\rm form}$.

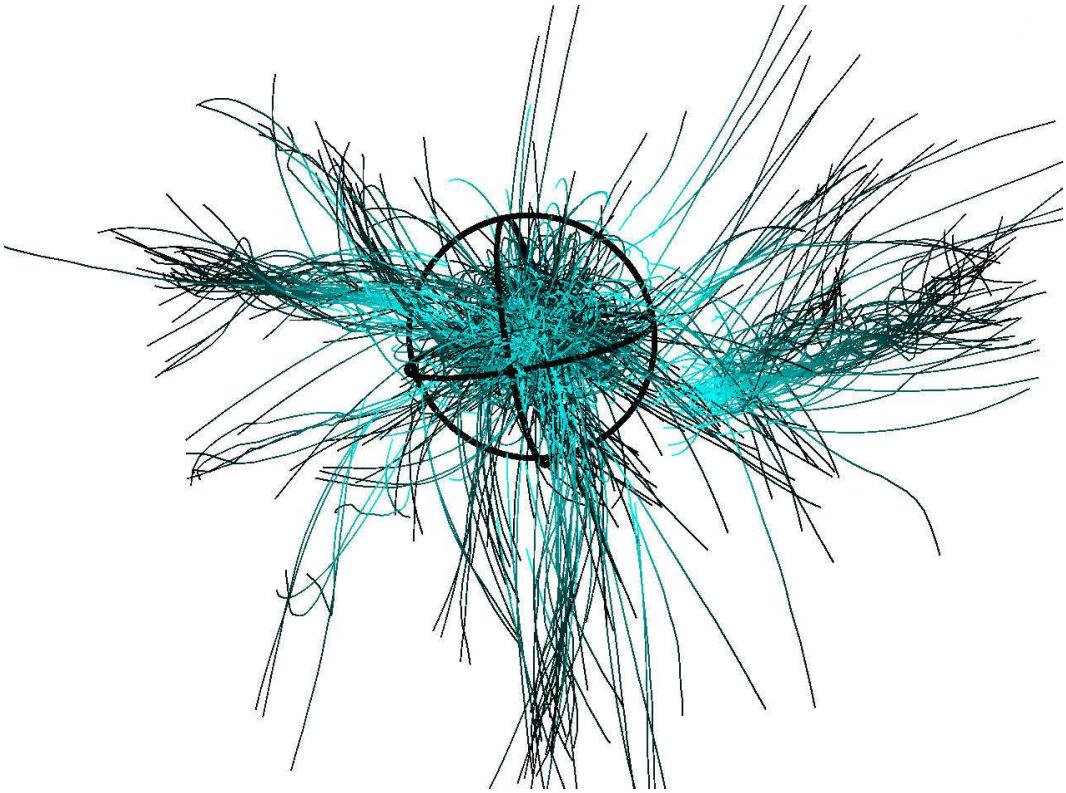

Figure 4.4: The orbits of the satellites for Halo #1
The orbits of all objects in the vicinity of the host halo are shown as lines that graduate from dark at $z_{\rm form}$ to light $z = 0$. The black spheres have a $2h^{-1}$ Mpc radius. The figure shows the "rich environment" of halo #1 with satellites continually infall into the halo.

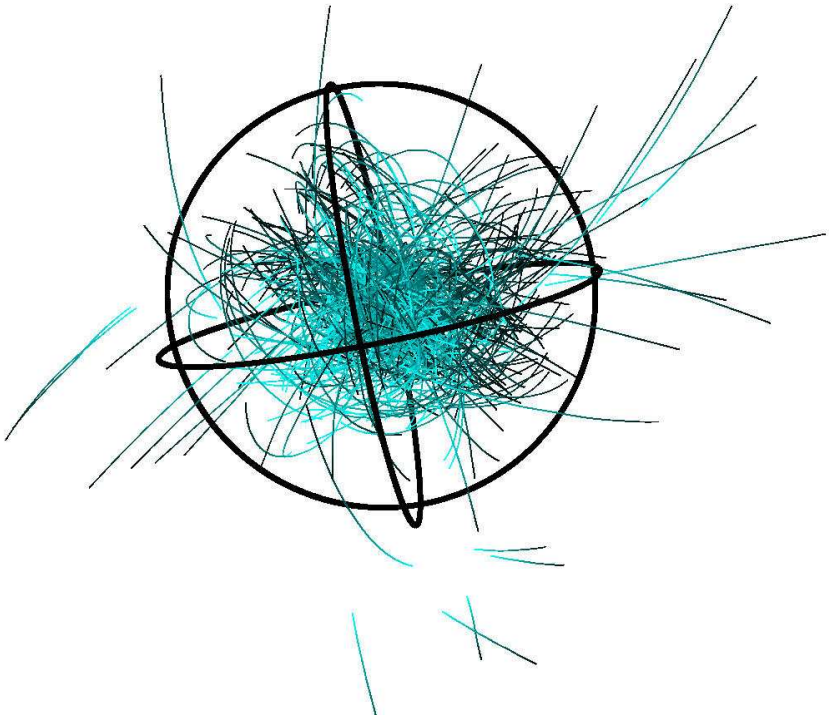

Figure 4.5: The same as Figure 4.4 but this time showing the more isolated halo #8. Halo #8 saw an early rapid infall of essentially all its associated satellite substructure then little latter on.

To further investigate the link between satellite disruption and satellite in-fall we calculate the ratio of disrupted (or "dead") satellites to the total number of satellites that fall into the host halo. The result is presented in Figure 4.6. It is now possible to interpret the slope of this figure as the "rate of disruption" of satellite galaxies. For all halos this disruption rate (i.e. slope) is very similar. There seems to be no strongly pronounced correlation with either mass, environment or age. In this respect, the destruction rate of satellite galaxies appears to be "common" in CDM halos. However, there also appears to be a (marginal) trend that host mass is related to the ability to disrupt satellites (within the limited mass range presented here). This can be seen explicitly for halos #1 and #3: #1 destroys its satellites more efficiently than #3 and is also the more massive of the two. However, these halos also have a large difference in triaxiality (refer to Table 4.1). Conversely, as halo #3 is comparable in mass to halo #4 with a strikingly similar satellite destruction rate. But as halo #3 and #4 are close in triaxiality, we rather suspect the disruption rate to correlate with mass than with triaxiality. However, this correlation - if in fact correct - must also have significant scatter, as the most massive halo (#8) shows the lowest destruction rate. This might be linked to the environment and supply of new satellites, respectively.

4.2.3 Summary of Host Halos and Satellite properties

Table 4.1 summarises the additional basic properties of our halos and their environments, illustrating the variety of richness and satellite number. Note, an applied mass-cut of $2 \times 10^{10} h^{-1}$ $M_{\odot}$ (corresponding to 100 particles) was used, which explains the rather 'low' number for $N_{\rm sat}(<r_{\rm vir})$ in Table 4.1. Further, this fixed mass cut explains the variation in the number of satellites from halo to halo.

4.3 Density Profiles of Satellites

For field galaxies in cosmological simulations there is the well know relationship between $r_{\rm max}$, the point where the rotation curve of the satellite galaxy peaks and the scale radius r_s (as defined in Eq. (4.1)) (Bullock 2001). In this section we aim to verify this relation for substructure halos, which on analytical grounds should be of the order $r_{\rm max} \approx r_s$.

To verify this analytical relation we rather use the cumulative density profile

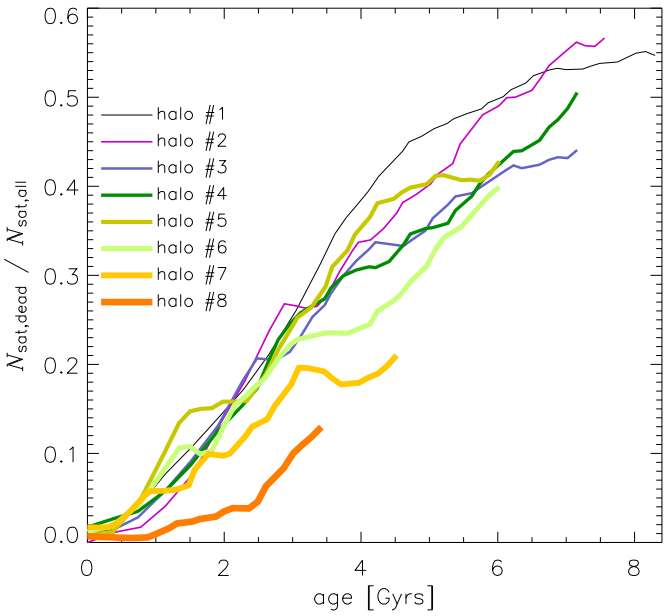

Figure 4.6: The rate of satellite disruption
The ratio of "disrupted" satellites to the total number of satellites for satellites within the virial radius of their respective host, as a function of time, where zero age is the formation time of the halo.

Table 4.1: Additoinal properties of the eight host dark matter halos.

Halo	$N_{\rm sat}(<R_{\rm vir})$	richness
# 1	158	4.7
# 2	63	3.1
# 3	87	4.3
# 4	57	2.9
# 5	175	3.6
# 6	85	3.2
# 7	59	1.9
# 8	251	2.8

$\rho(< r)$ than the differential $\rho(r)$; for (sub-)halos containing orders of magnitude fewer particles than the host this leads to a more smooth profile and hence a more stable fit to an analytical function.

$$\rho^{\rm cum}(r) = \frac{M(< r)}{4\pi r^3/3} = \frac{\rho_s r_s^3}{r(r_s + r)^2} \tag{4.1}$$

where r_s is our scale radius used to calculate the concentration $c = r_{\rm vir}/r_s$. Navarro (1997) used the differential density profile

$$\rho^{\rm NFW}(r) = \frac{dM(r)}{dV} = \frac{\rho_s^{\rm NFW} R_s^3}{r(R_s + r)^2} \tag{4.2}$$

where is r_s again is used to define the concentration $c_{\rm NFW} = r_{\rm vir}/R_s$ of the halo. We are interested in a relation between our scale radius r_s and the maximum of the circular rotation curve $r_{\rm max}$ as presented for our sub-halo populations in Figure 4.7. Therefore using

$$v_{\rm circ}^2 = \frac{GM(< r)}{r} \tag{4.3}$$

together with Eq. (4.1) gives

$$v_{\rm circ}^2 = \frac{4\pi G r \rho_s r_s^3}{3(r_s + r)^2} \tag{4.4}$$

We obtain the maximum of $v_{\rm circ}$ by differentiating it with respects to r

$$\frac{dv_{\rm circ}}{dr} = \frac{1}{2v_{\rm circ}} \frac{4\pi G r_s^3}{3(r_s + r)^2} \left(1 - \frac{2r}{r_s + r}\right) \tag{4.5}$$

and setting it to zero. Simple algebra then reveals the relation

$$r_s = r_{\rm max} \tag{4.6}$$

To verify this relation we plot r_s versus $r_{\rm max}$ in Figure 4.7. We find that this relation holds for all our satellite galaxies with very little scatter. The solid line is the one-to-one relation with the dashed lines showing $r_s = 2r_{\rm max}$ (upper) and $r_s = 0.5r_{\rm max}$ (lower).

Thus as for satellite galaxies in the 'field' this same relationship holds for galaxies within clusters. Although it is important to verify this relationship with higher resolution simulations since the inner profiles of sub-halos are challenging to resolve.

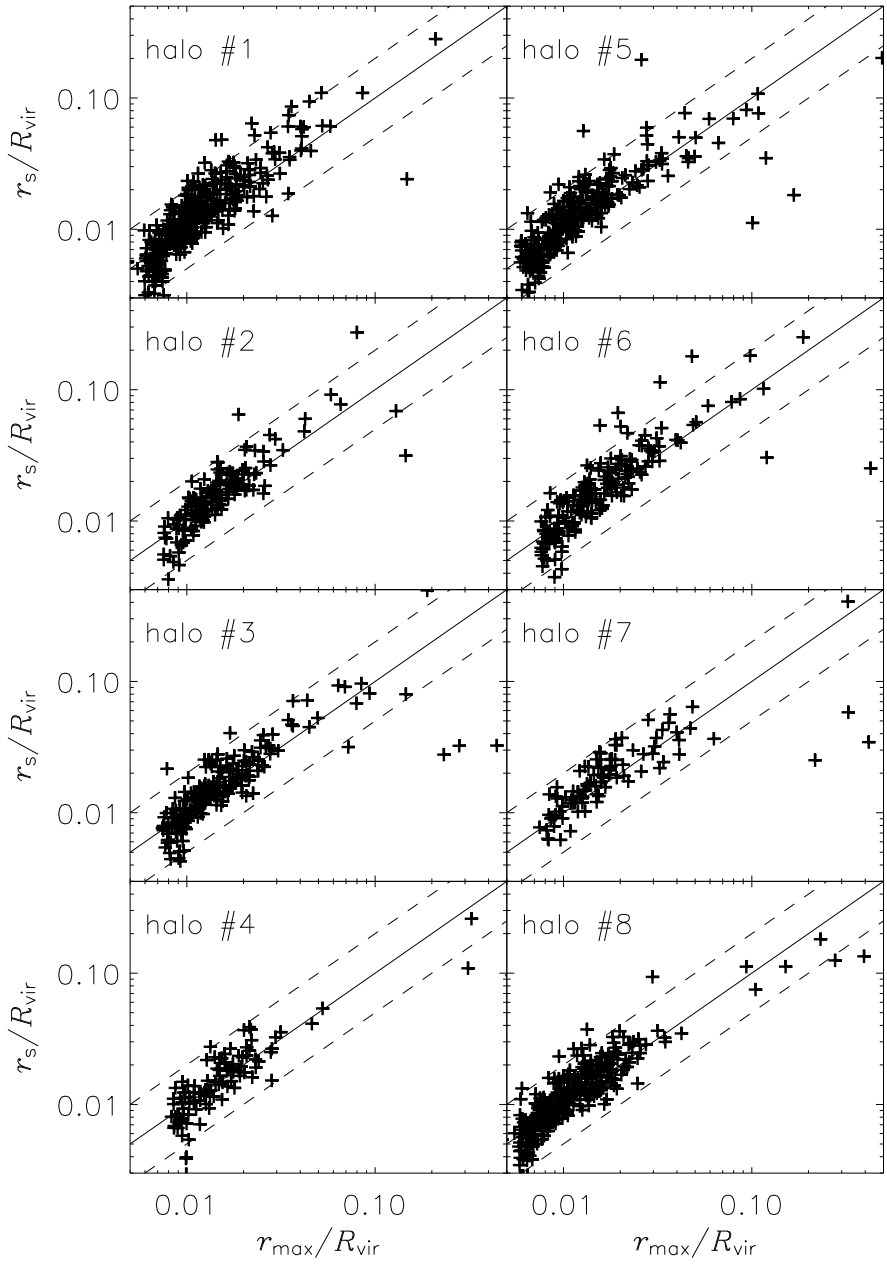

Figure 4.7: Density Profiles of Substructure Halos
We plot the relation between scale radius r_s defined in Eq. (4.1) and the position of the maximum of the rotation curve. Both of these values are normalised by the hosts virial radius.

4.4 Satellite Orbital Parameters

We now turn to the detailed analysis of the evolution of satellite galaxies. In the following subsections we investigate their lifetimes, orbital parameters, and derive relevant correlations and relations.

4.4.1 Number of Satellite Orbits

In Figure 4.8 we show the distribution of the number of orbits for both surviving satellites (thick lines) and disrupted satellites (thin lines) at redshift $z = 0$.

For the satellites that survived until $z = 0$ the distribution peaks at or near one orbit for each of the eight host halos. More than 70% of the satellites have had at least one full orbit with some having as many as four, therefore making a study of the satellite dynamics valid. The length of the tail to the right of the peak at one orbit is somewhat correlated with the age of the dark matter halo. Further, the peak is more pronounced in the younger halos. However, halos #1 and #3 both show distinctive peaks at one orbit which relates to the richness of environment given in Table 4.1, rather than the age, as satellites are continuously falling in.

The interpretation of the distribution for the disrupted satellites is more interesting. We note that these orbits are determined by mass-less tracer particles placed at the last credible centre of the satellite before disruption. The distributions are generally "flatter" with the most prominent peak near zero orbits. One explanation for such a distribution is that the in-falling satellites are being disrupted before completing one orbit. This suggests that satellites contributing to this bin in the distribution are very massive and rapidly decay via dynamical friction. Having said that, we emphasize that this interpretation may be somewhat simplistic. All satellites were identified at $z_{\rm form}$ and we do not have an indication as to how long the satellites had already existed within the host's progenitor prior to that redshift. Therefore, (massive) satellites that had already been orbiting within the progenitor would be the first to be disrupted, giving this biased result. Another small contribution to this bin is from the sub-substructure. As seen in Figure 4.4 the systems of substructure are spiralling into the dark matter halo, thus the sub-structure is being destroyed in its very own (sub-)host before completing a full orbit. Regardless of this "zero orbit" peak, most of the disrupted satellites complete at least the same number of orbits as the ones which survive to $z = 0$.

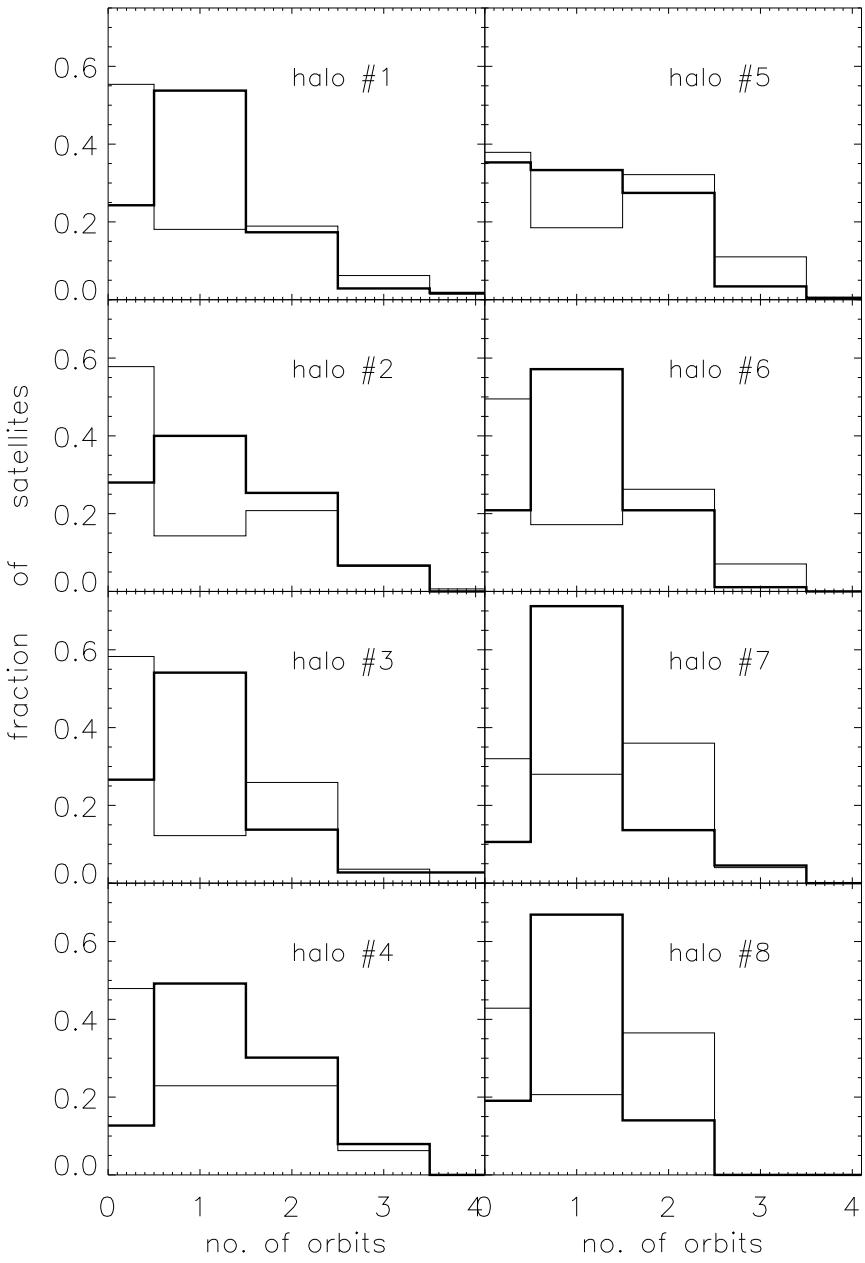

Figure 4.8: Satellite number of orbits

The thick histograms show the distribution of the number of orbits for all satellites that survive until redshift $z = 0$. The thin histograms show the distribution for disrupted satellites.

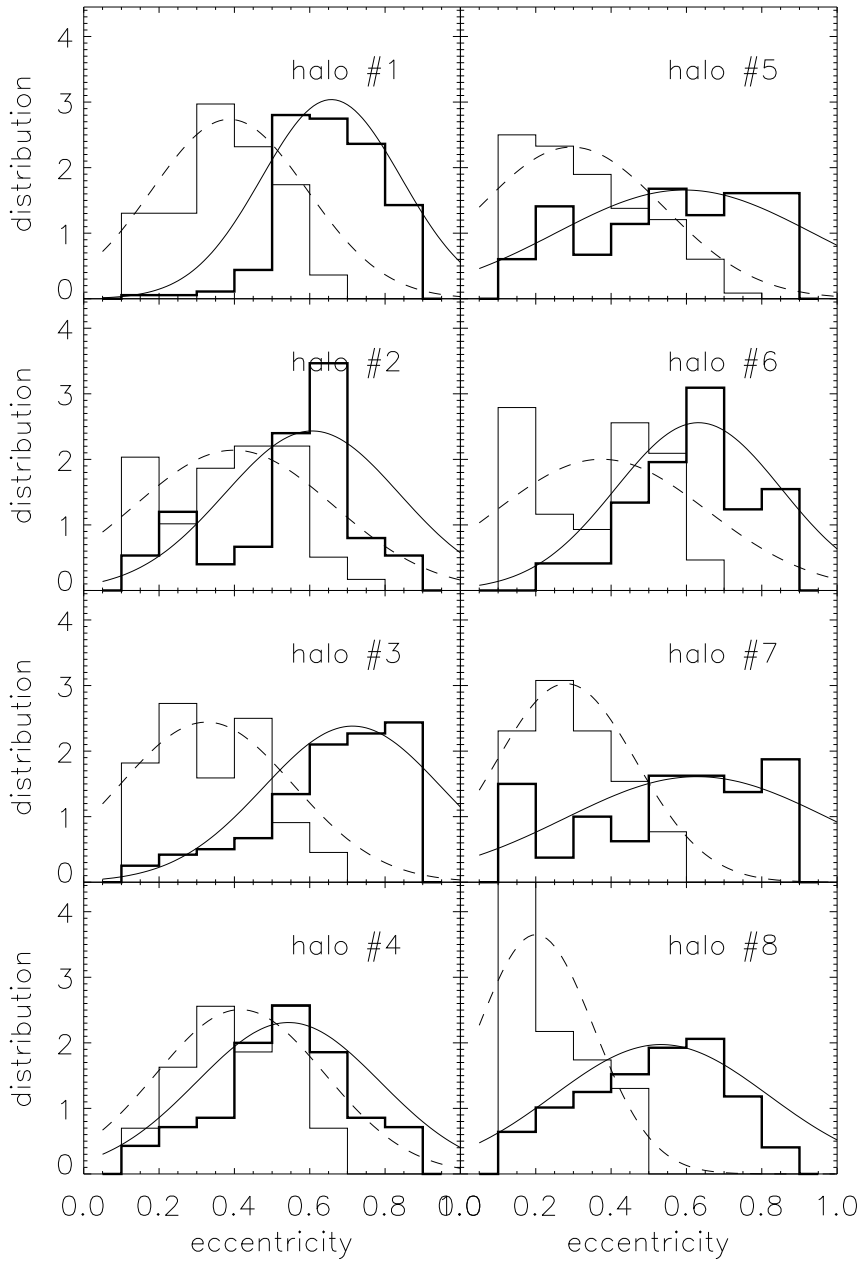

Figure 4.9: The orbital eccentricity distribution

The orbital eccentricity distribution function presented as histograms for all satellites that survived until redshift $z = 0$ (thick lines) and those which were destroyed (thin lines). The curves represent best-fit Gaussians to the distributions.

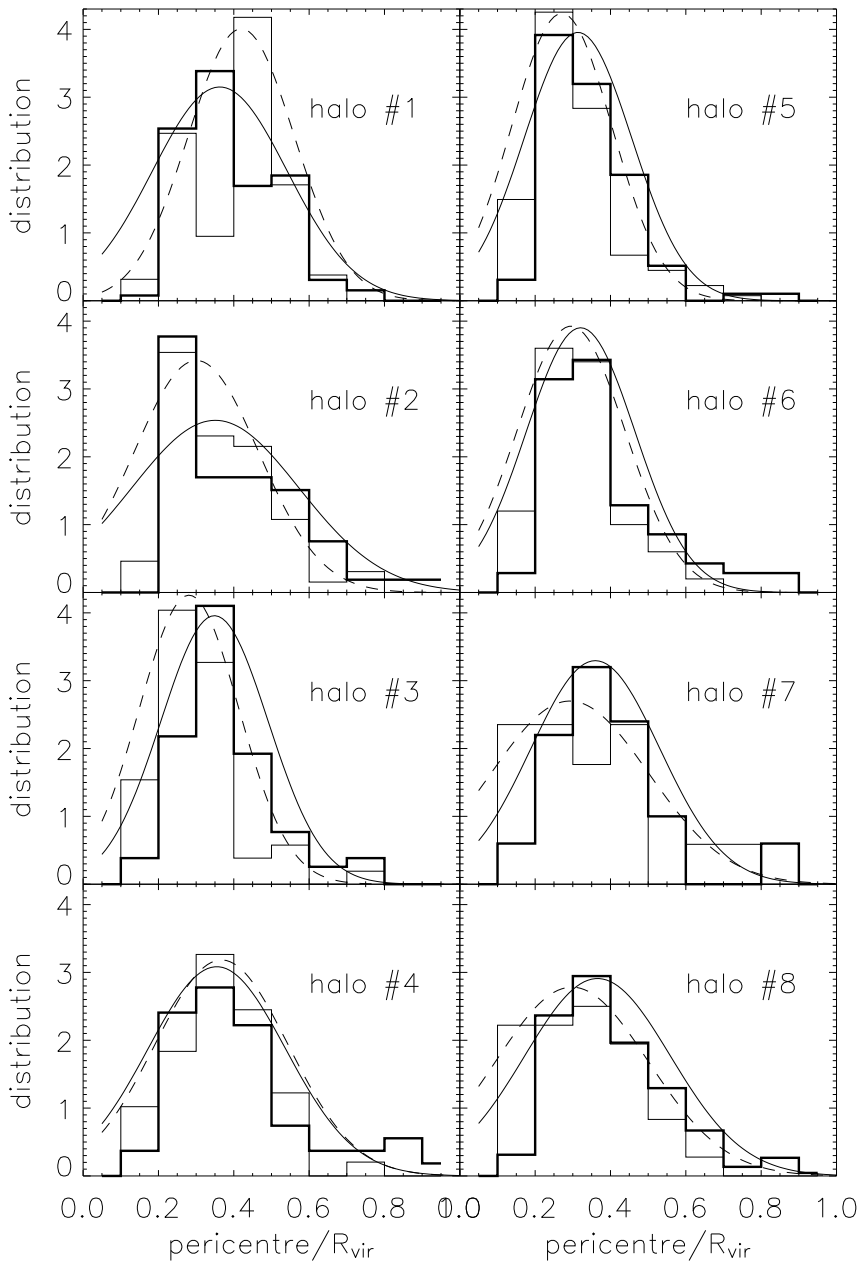

Figure 4.10: The orbital pericentre distribution

The orbital pericentre distribution function presented as histograms for all satellites that survived until redshift $z = 0$ (thick lines) and those which were destroyed (thin lines). The curves represent best-fit Gaussians to the distributions.

4.4.2 Orbital Eccentricity and Pericentres

As previously stated, we define eccentricity as

$$e = 1 - \frac{p}{a} \, , \tag{4.7}$$

where the pericentre p and apocentre a distances were those last measured in the satellite's (or the tracer particle's) orbit. Using this definition we show in Figure 4.9 the distribution of the orbital eccentricity e for both live (thick lines) and disrupted satellites (thin lines). Further, we fit a Gaussian

$$P(e) = \frac{1}{\sqrt{2\pi\sigma^2}} \, e^{-\frac{(e-e_0)^2}{2\sigma^2}} \tag{4.8}$$

to the distributions (solid curves for live and dashed lines for disrupted satellites). From this fit the peak orbital eccentricity for the eight halos has an average of $\langle e_0 \rangle = 0.61$ with an average standard deviation of $\langle \sigma \rangle = 0.19$. We do not observe again any correlation of peak position and width of the distribution with environment, age, host history or richness, even though σ appears to be larger for the younger dark matter halos. It is interesting to note that if we stack the data from the eight halos together and then separate the satellite population into differing mass bins we see little variation. This common behaviour still holds and probably reflects the scale free nature of gravity and hierarchical structure formation in CDM models. The disrupted satellites, however, have a different distribution, almost mirroring the survivors about the $e = 0.5$-axes, with the peak eccentricity near $\langle e_0^d \rangle = 0.34$ and a dispersion of $\langle \sigma^d \rangle = 0.16$. Thus, the destroyed satellites were preferentially on more circular orbits.

The pericentre distributions provide additional insight into the nature of the orbits of the disrupted satellites. The result for redshift $z = 0$ can be seen in Figure 4.10 where p has been normalised by the virial radius of the host. Again, live satellites are represented as thick lines and disrupted ones as thin lines. A striking characteristic of these distributions is again the similarity between the halos. Moreover, we also observe a similarity in the distribution for the live and disrupted satellites. This is emphasised particularly by the best-fit Gaussians to the distributions. The maximum peak lies at 35% of the virial radius for live satellites with a mean dispersion of $\langle \sigma \rangle = 0.12$ as opposed to 31% of $R_{\rm vir}$ for the disrupted ones with a dispersion of $\langle \sigma^d \rangle = 0.11$. Unlike eccentricity, the pericentre distribution rises

quickly towards the peak and falls off moderately to the outer parts of the host halo. We already noted the lack of correlation with mass, age, environment and richness, but there is, however, a mild dependence on the state (live or dead) of the satellite as disrupted satellites appear to have had marginally nearer excursions towards the host centre. When we stack the data from the eight halos and separate into differing satellite mass bins we again see little variation.

In summary the difference between live and disrupted satellites lies primarily in the eccentricity distribution. Disrupted satellites seem to be on more circular orbits. Since the disrupted satellites have similar pericentres to those which survive their circular nature means that they spend more time in the deeper regions of the potential well. Hence, they experience stronger tidal forces for longer periods, and are thus disrupted more easily.

We close this subsection with an examination of the pericentre-eccentricity relation (Figure 4.11). The crosses represent the satellites that survived until redshift $z = 0$, while the diamonds represent the disrupted satellites. Although many of the features seen here are also seen in Figure 4.9 and Figure 4.10, there are two additional ones which we will comment on now.

One such feature is the bimodality in the satellite distribution of halo # 1. In this Figure there seems to be two distinct (live and dead) satellite populations orbiting within the dark matter halo. As we saw, particularly in Figure 4.4, this dark matter halo lies in a rich area being fed by (at least) two filaments. Perhaps these two satellite populations are a remnant of the filamentary large-scale structure surrounding the host? If that is true, it is interesting that the satellites still maintain their dynamical distinctiveness after several orbits.

In addition there appears to be a distinct population of satellites with an extremely tight (anti-)correlation between eccentricities $e \approx 0.6 - 0.9$ and pericentres $p \approx 0.3 - 0.8$ in many halos. Upon detailed investigation these satellites were identified to have completed one orbit and were entering the halo for the first time. This is consistent with the notion of the satellites in-falling on radial orbits. We investigate this point in the next section, namely the evolution of eccentricity.

4.4.3 Evolution of Eccentricity

In the previous section we considered the orbital characteristics of the satellites at redshift $z = 0$. We now investigate the evolution of the orbital eccentricities of the

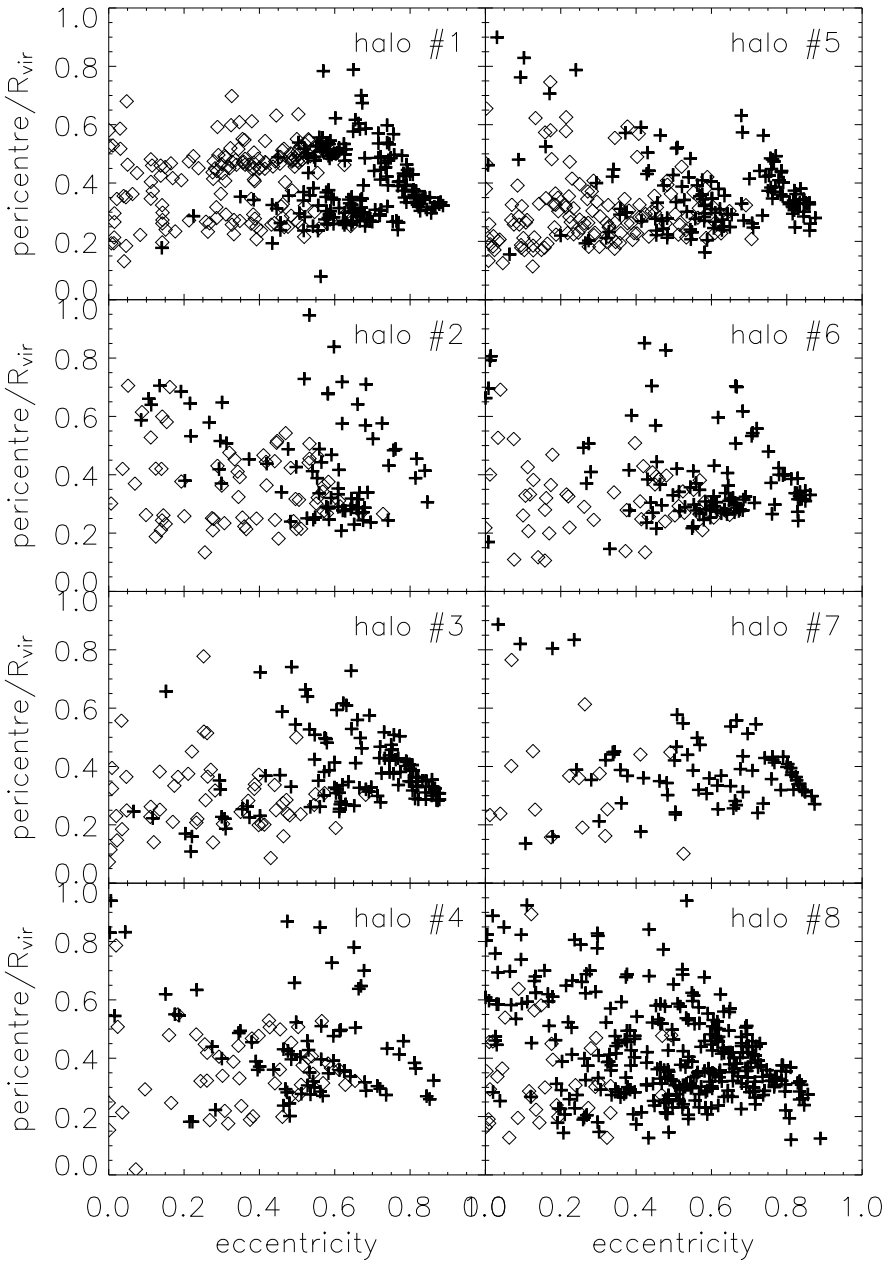

Figure 4.11: Satellite eccentricity vs pericentre

We plot the satellite eccentricity against pericentre normalised by the virial radius of the host. The crosses represent the satellites that survived until $z = 0$ while the diamonds represent the disrupted satellites.

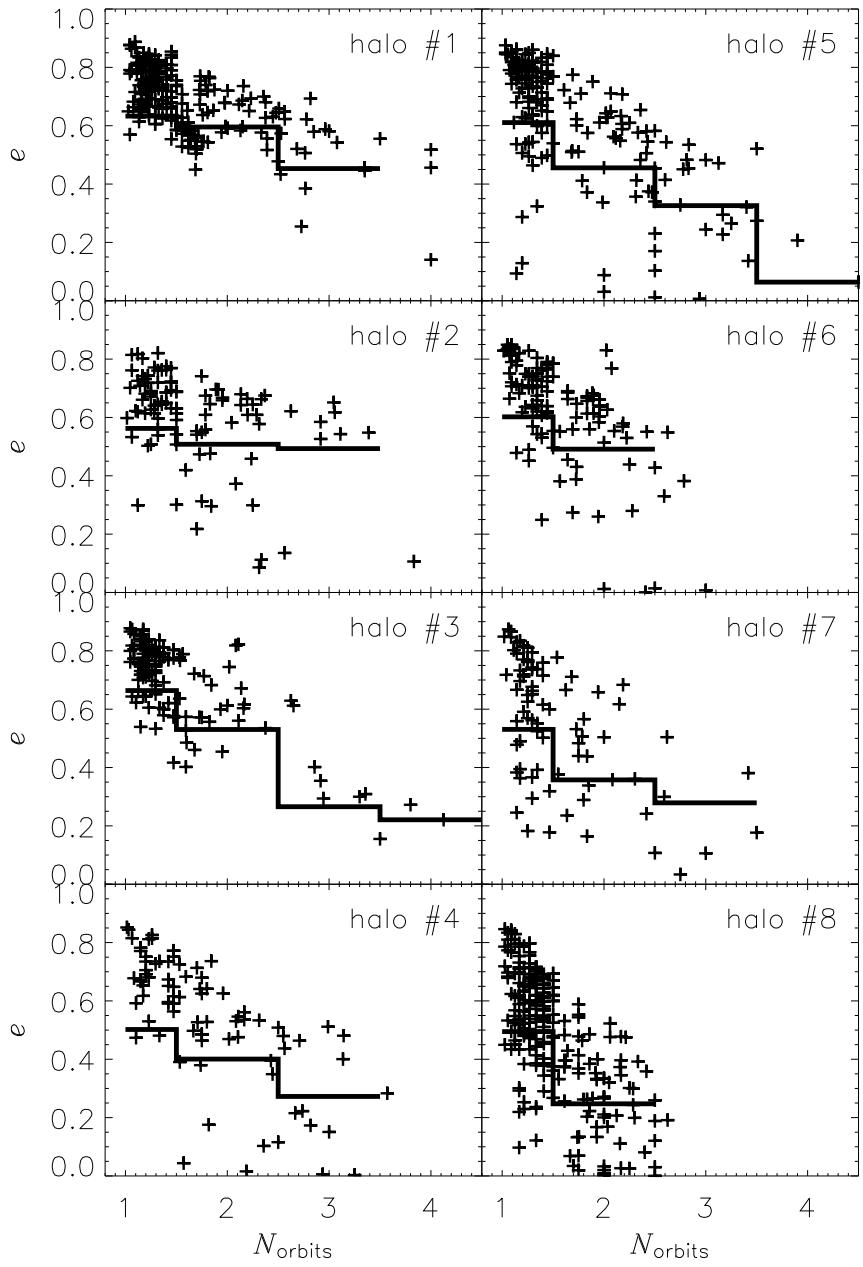

Figure 4.12: Evolution of orbital eccentricity
The final orbital eccentricity plotted against the number of orbits completed for each surviving satellite (crosses). The histogram shows the averaged eccentricity (see text for details).

satellite family.

Figure 4.12 shows the eccentricity of each satellite (represented by the crosses) versus the number of orbits the satellite has completed. There is a clear trend for eccentricity to decrease as the number of orbits of a satellite increases. This is also demonstrated by the histogram, which is not the "binned" results of the crosses, but is instead the average eccentricity for all satellites that had $\geq N_{\rm orbits}$ orbits

$$\langle e \rangle (N_{\rm orbits}) = \frac{1}{N_{\rm sat}(\geq N_{\rm orbits})} \sum_{i=1}^{N_{\rm sat}(\geq N_{\rm orbits})} e_i(N_{\rm orbits}) \ . \tag{4.9}$$

Here, $e_i(N_{\rm orbits})$ is the eccentricity of satellite i after $N_{\rm orbits}$ orbits and $N_{\rm sat}(\geq N_{\rm orbits})$ is the number of satellites with equal or more than $N_{\rm orbits}$ orbits.

For example, a satellite that has had 3 orbits contributes its respective value of eccentricity to the average eccentricity in the bins for 1, 2, and 3 orbits. This histogram shows a trend indicative of orbit circularisation with time. Before the work of Hashimoto et al. (2003) one would have been quick to interpret this result as dynamical friction circularising the orbits, however, they suggested otherwise. To confirm this, we selected the satellites at differing pericentre, as dynamical friction is proportional to the local density of the background field, and thus has it's strongest influence at pericentre. Having done this, we saw no significant change in the above trend. Further, when we used the analytical predictions of Taffoni et al. (2003) we found that very few satellites in the population presented could be affected by dynamical friction. Therefore, we do not attribute the circularising of the orbits to dynamical friction. One mechanism which could be responsible for the circularising of the orbits is the secular growth in the host halo's mass. In response to this increase in host mass the velocity and hence the orbit of the satellite changes. Further we suggest that this change acts to circularise the orbit. Within the context of a fully self-consistent N-body simulation this claim is difficult to verify. However, in Section 4.5 we show that a clear relationship exists between satellite velocity dispersion and host halo mass, implying that the satellite velocities respond to a change in host mass.

Finally we compare our orbital parameters to those presented by Ghigna et al. (1998). The major difference between our respective analysis in the derivation of the orbital characteristics is that even though their host halos and satellite galaxies formed fully self-consistently in cosmological simulations they took the satellite positions

and velocities and evolved them in a *static spherical potential* in order to obtain orbital characteristics. Ghigna et al. found that the satellites on radial orbits were more likely to be disrupted than those on circular orbits because they penetrate further into the dark matter halo potential well. In addition, radial orbits were quite common and circular orbits quite rare in their simulations. The average ratio of apocentre:pericentre in their outputs was 6:1, with nearly 25% of the halos on orbits with ratios in excess of 10:1. In our language this 6:1 ratio equates to an eccentricity of ~ 0.83. Hence, the Ghigna et al. satellite orbits were considerably more radial than ours. We can not reconcile this discrepancy through dynamical friction arguments. However, it could potentially be explained by the lack of a live halo. This explanation correlates with our previous finding in Section 4.4 for a recently in-falling satellite population. This latter population constitute a distinct subpopulation with a strong (anti-)correlation in Figure 4.11 and an average eccentricity of ~ 0.8, quite similar to the result of Ghigna et al. .

4.4.4 Circularity of Orbits

Another way to measure the circularity of the orbits can be written

$$\lambda = \frac{J_{\mathrm{sat(E)}}}{J_{\mathrm{circ(E)}}} \tag{4.10}$$

where λ is the ratio between the actual angular momentum of the satellite J_{sat} and the angular momentum of a circular orbit J_{circ} with the same energy E.

The correlation of λ with the the orbital eccentricity defined in Eq. (4.7) is presented in Figure 4.13 for all satellites that had at least one full orbit at redshift $z = 0$. The solid lines are upper limits given by the assumption that both satellite and host halo are point masses. For a derivation of this relation please refer to the Appendix.

We observe that most of the satellites follow the trend indicated by the analytical estimate showing that low-eccentricity satellites are in fact on more circular orbits. However, the trend is only suggestive but not strong with a significant scatter making it difficult to substitute one measure for the other.

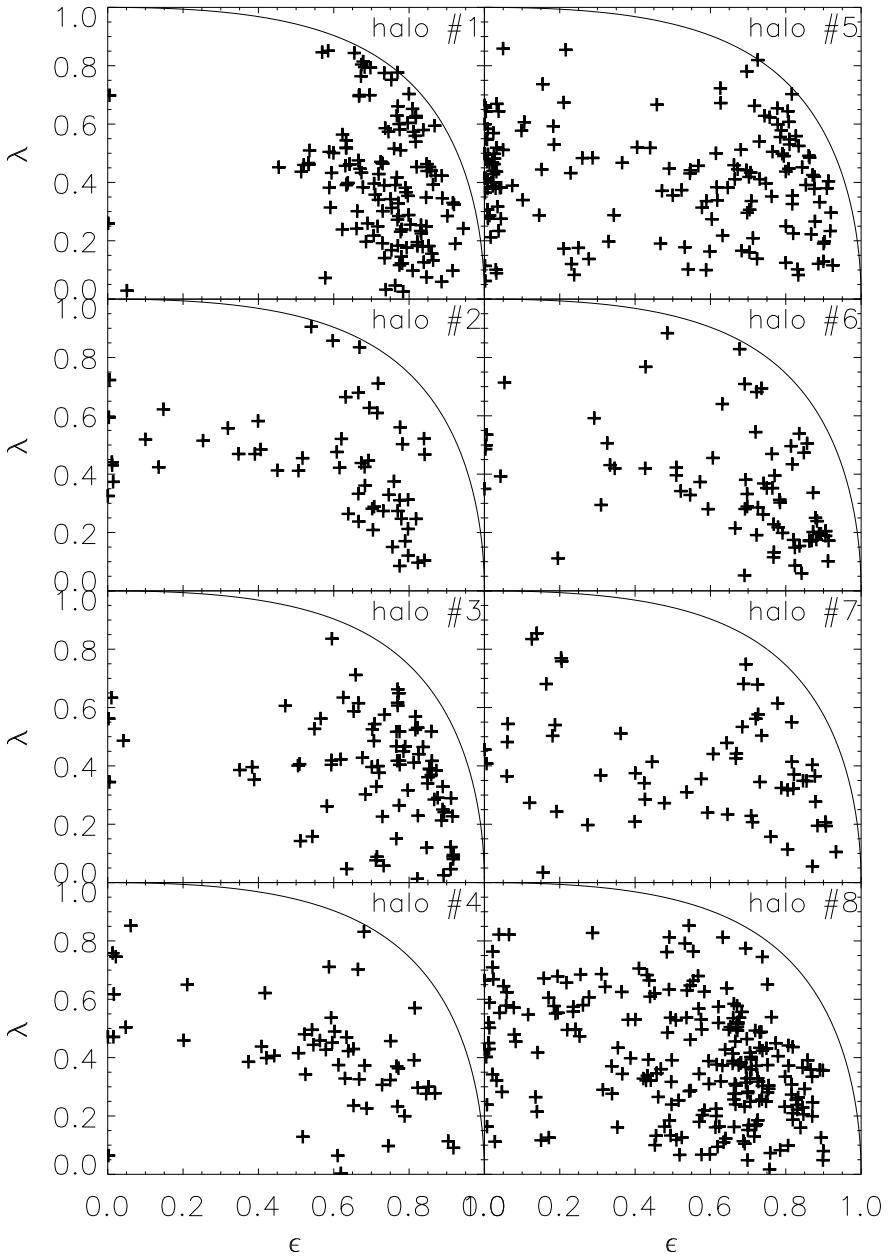

Figure 4.13: Circularity vs orbital eccentricity
Circularity as a function of orbital eccentricity. Only satellites with at least one full orbit are considered and the solid line marks the 1:1 correlation.

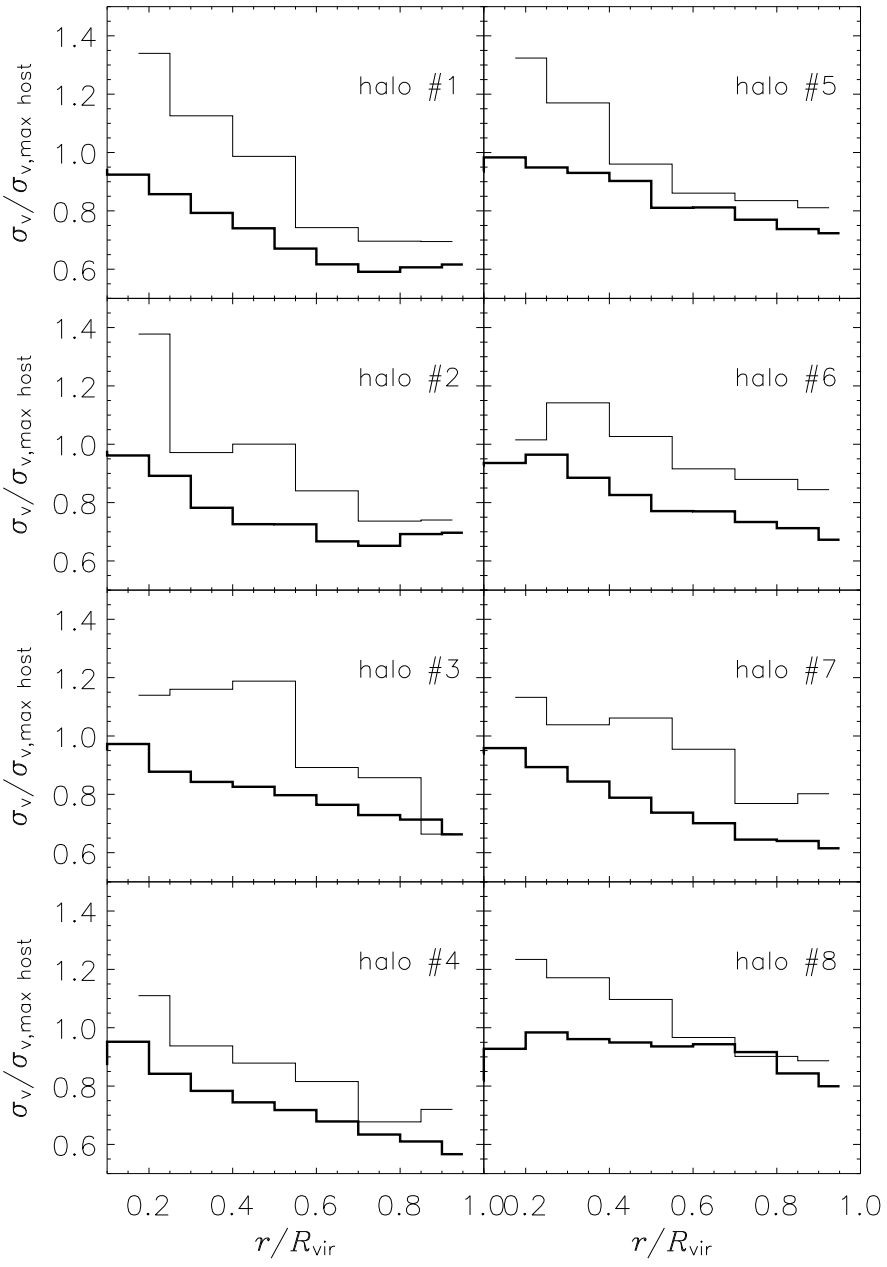

Figure 4.14: Radial velocity dispersion

The normalised three dimensional velocity dispersion as a function of halo-centric distance normalised by the maximum circular velocity of the host halo. The dark lines represents the dark matter distribution, while the light line is the satellite distribution.

4.5 Host and satellite kinematics

A controversy still exists as to whether or not cluster members trace the dark matter velocity distribution. Colin et al. (2000) found a substantial positive velocity bias when calculating the local (or one-point) velocity bias

$$b_v(r) = \frac{\sigma_{v,\mathrm{sat}}(r)}{\sigma_{v,\mathrm{DM}}(r)} \ . \tag{4.11}$$

A similar yet less pronounced signal was reported by Okamoto & Habe (1999), whereas Ghigna et al. (1998) did not find any significant velocity bias in their analysis of cluster substructure. Ghigna et al. (2000) re-visited this issue, obtaining a small positive bias, but much weaker than that reported by Colin et al. (1999). Springel et al. (2001) also examined this question, suggesting a small anti-bias from their cluster simulations.

We now attempt to shed light on this controversy, by comparing the kinematical properties of the host halo and the satellite populations. We first look at the three-dimensional velocity dispersion normalised by the maximum circular velocity of the host as a function of (normalised) halo centric distance. The results for all eight host halos is presented in Figure 4.14. The dark matter distribution of the halo is represented by the thick histograms while curves based upon the satellite galaxy population are plotted as thin histograms. Note that we do not see the characteristic "rise and fall" for the velocity dispersion of a Navarro, Frenk & White (1997) profile (cf. Lokas & Mamon 2001), because for the host halos under consideration σ_v peaks at about 10% of R_{vir}, which is where we start to plot the data. In general though, from the inner bin at 10% of R_{vir} out to R_{vir} we see a drop in the dark matter's three-dimensional velocity dispersion. This drop is even more pronounced for the satellite population. Thus in general for each halo we see an increasing satellite "local velocity bias" as we get closer to the center of the host halo. In the outer regions we have $b_v(\leq R_{\mathrm{vir}}) \sim 1.0$ while in the inner regions $b_v(\geq 0.1R_{\mathrm{vir}})$ varies from $1.1 - 1.4$ with the largest value for b_v being recorded for halo #2, $b_v(\approx 0.1R_{\mathrm{vir}}) \sim 1.4$. Essentially for all halos though $b_v(r) \geq 1.0$ at all radii. This result agrees with the data shown by Colin et al. (1999) and Ghigna et al. (2000), in which both groups found that the satellite population is "positively" biased with $b_v(\approx 0.1R_{\mathrm{vir}}) \sim 1.2 - 1.3$. However, it contrasts with the Springel et al. (2001) findings in which a small negative velocity bias for the central regions of the cluster was claimed.

Table 4.2: The global velocity bias for the eight host dark matter halos, within the virial radius.

halo	$\sigma_{v,halo}$	$\sigma_{v,sats}$	$b_{v,\mathrm{global}}$	$b_{v,\mathrm{global}}^{N_{\mathrm{orbits}}\geq 1}$
# 1	1140	1077	1.12	1.01
# 2	887	811	1.07	1.01
# 3	900	834	1.09	0.98
# 4	789	729	1.06	0.99
# 5	1170	1168	1.08	0.98
# 6	857	807	1.12	1.03
# 7	811	852	1.19	1.13
# 8	1067	1119	1.09	1.02

There is no discernible relationship between the eccentricity distribution (cf. Figure 4.9) and the bias seen in Figure 4.14; however, there is sufficient orbital distribution variation to accommodate for the variation in the bias. Improved statistics will be needed to decouple the detailed variations. However, we have shown that the velocity bias has the same basic shape for all eight halos, strengthening the case that this is a general characteristic of the satellite population.

Using all the dark matter particles and satellite galaxies within the virial radius we also calculate the global velocity bias

$$b_{v,\mathrm{global}} = \frac{\sigma_{v,\mathrm{sat}}(< R_{\mathrm{vir}})}{\sigma_{v,\mathrm{DM}}(< R_{\mathrm{vir}})} \tag{4.12}$$

which is summarized for all eight halos in Table 4.2. It is interesting to note that we find a slight positive bias, even though Klypin et al. (1999) and Ghigna et al. (1998) both claimed that such a global velocity bias should not exist. However, Klypin et al. (1999) did hint that the possibility of a mild negative bias might exist, based upon earlier theoretical work by Carlberg (1994). Carlberg argued that as galaxies fall into the cluster for the first time they lose energy to the cluster and become systematically more bound, orbiting freely as coherent, self-gravitating units. From his simulation he measured a value of $b_{v,\mathrm{global}} \sim 0.8 \pm 0.1$. From our halos we find an average global velocity bias $\langle b_{v,\mathrm{global}} \rangle \sim 1.103 \pm 0.002$, which is only a very slight bias. If we restrict the global velocity bias calculation to satellites that have had at least one orbit, $\langle b_{v,\mathrm{global}}^{N_{\mathrm{orbits}}\geq 1} \rangle \sim 1.019 \pm 0.002$, a 7% decrease in the bias. The quoted errors are the scatter within the eight halos.

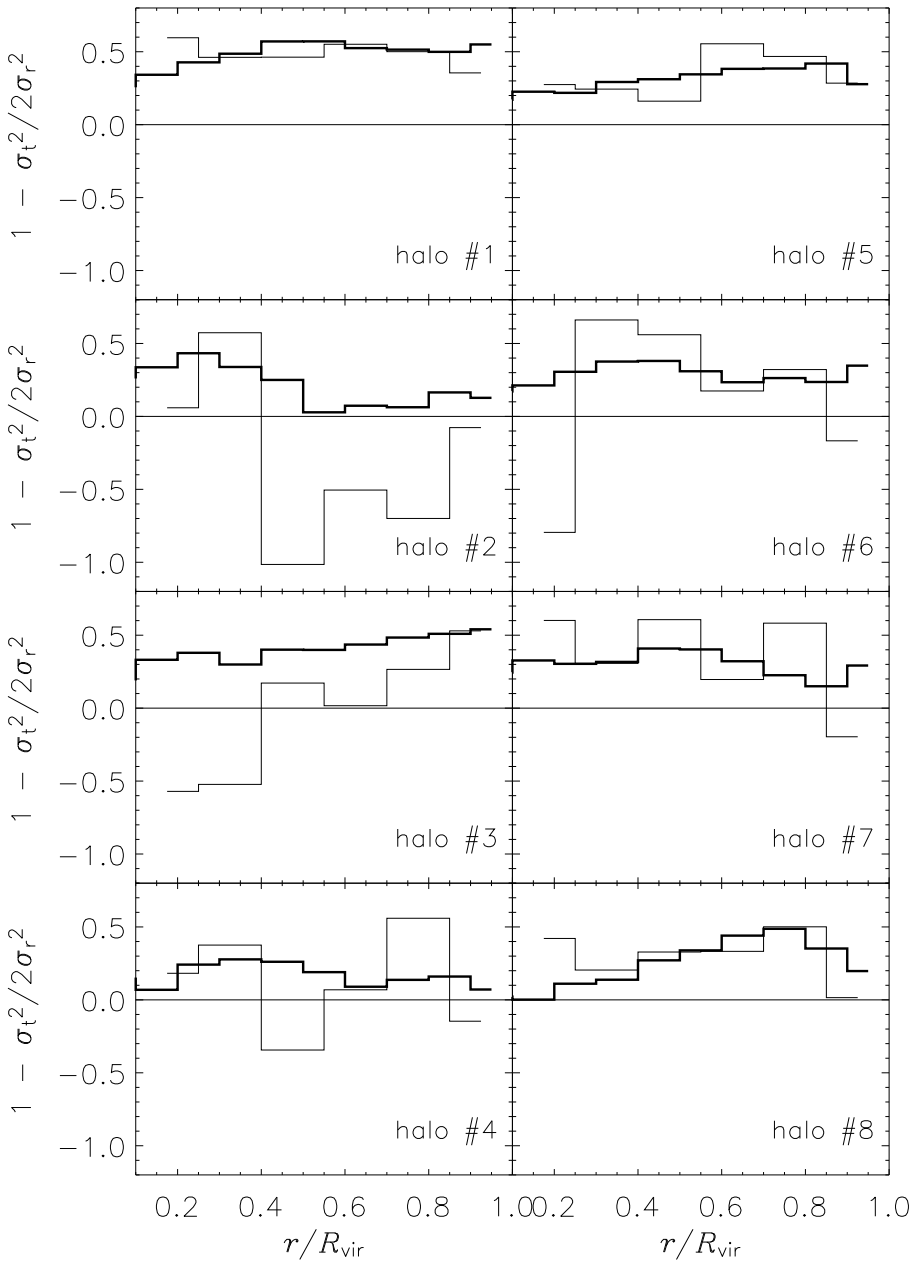

Figure 4.15: Radial velocity anisotropy

The velocity anisotropy parameter as a function of halocentric distance. The thick line represents the dark matter distribution, while the thin line is the satellite distribution. The quantities were calculated in linear radial bins.

To further investigate the velocity bias we measure the variation from an isotropic velocity distribution using the anisotropy parameter, as seen in Figure 4.15

$$\beta = 1 - \sigma_t^2/2\sigma_r^2 \ , \tag{4.13}$$

where σ_t measures the variance in the tangential and σ_r in radial direction. Once again, the dark matter ($\beta_{\rm DM}$) and satellite distribution ($\beta_{\rm sat}$) were averaged in linearly spaced radial bins, normalised by the virial radius. The dark matter distribution is represented by the thick histogram and the satellite galaxies by the thin histogram. For an isotropic distribution $\beta = 0$; if $\beta \to 1$, then the velocities are preferentially radial; if $\beta \to -\infty$, they are preferentially tangential.

The standard way to represent β is on a logarithm scale starting from the inner percent of the virial radius. Cole & Lacey (1996) and Thomas et al. (1998) employed this technique and measured a linear increase in $\beta_{\rm DM}$, starting with essentially isotropic orbits close to the halo core and becoming increasingly radial in the outer regions. In keeping with previous figures we plot the data on a linear scale. This makes it difficult to compare to this work. However, our value for $\beta_{\rm DM}$ does follow the same general radial relationship seen in earlier studies.

In general $\beta_{\rm sat}$ for the substructure population (broadly) follows the dark matter distribution. However, for halos #2 and #3, satellite orbits are generally more tangential than the dark matter background.

Finally, to gain further insight into the velocity distributions of the satellite and dark matter distributions we investigated the radial variation of the radial velocity component. When normalised by the maximum circular velocity for all eight halos, we find that the fraction $v_{r,\rm DM}/V_{\rm circ}^{\rm max}$ is essentially zero. Although, we do see signs of a slight dip in the outer regions. This dip is a characteristic signature of in-fall into the system.

4.5.1 Observational Impact

One way Astronomers determine the mass of galaxy cluster by assuming that the galaxy distribution is virialised. The virial theorem then gives (Heisler, Tremaine & Bahcall 1985):

$$M_{\rm vir} = \frac{R_{\rm vir}\sigma_v^2}{G} \ . \tag{4.14}$$

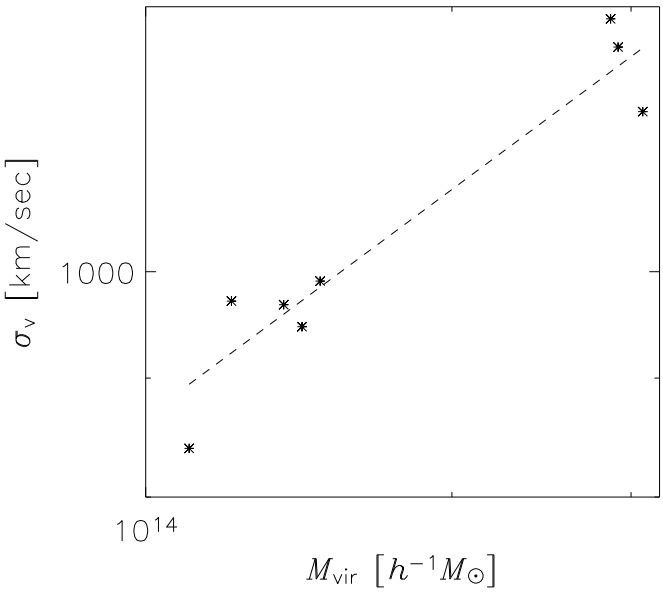

Figure 4.16: Satellite velocity dispersion vs Host halo mass
The velocity dispersion of the satellite galaxies within the virial radius of the host halo as a function of host halo mass.

In practice, however, the observational determination of the correct radius $R_{\rm vir}$ and velocity dispersion σ_v are far from straightforward, as it is difficult to determine whether or not a galaxy is a member of a cluster. Furthermore, even though we have just learned that the satellites are "stationary", the existence of the slight global velocity bias (cf. Table 4.2) does impact the determination of cluster masses. Or in other words, the observed positive bias will result in an over-estimation of the halo mass when relying on the dynamics of its substructure.

From our simulations we find (to no surprise) that the velocity dispersion of a system of galaxies is a reliable indicator of the depth of the potential associated with the system. Even though we do not have a broad mass range ($M_{\rm vir} \sim 1 - 3 \times 10^{14} h^{-1}$ M$_\odot$) to test this hypothesis we reconstruct the expected relationship between mass $M_{\rm vir}$ and velocity dispersion $\sigma_{v,{\rm sat}}$ of the satellite galaxies within the virial radius of the host halo. The results are presented in Figure 4.16. Each of our halos scatter about the expected analytical relationship:

$$\sigma_v \sim M_{\rm vir}^{1/3} \tag{4.15}$$

This relationship can easily be understood analytically when we combine Eq. (4.14) and our definition for virial radius $\Delta_{\rm vir}\rho_b = 3M_{\rm vir}/(4\pi R^3_{\rm vir})$. The solid line displayed in the figure is the best fit power law to our eight data points. The logarithmic slope was found to be ~ 0.329, sufficiently close to the expected value of $1/3$.

4.6 Conclusions

In Chapter 2 we analysed the differences between the host halos. In the first part of this chapter we described global properties of the satellite populations, such as richness. Through this analysis we discovered that our sample of dark matter galaxy clusters sampled a variety of triaxialities, formation times and mass/satellite accretion rates and formation histories (from quiescent to violent) despite being of comparable mass. Even though the differences between the host halos we found considerable similarities between the satellite populations.

These similarities are dramatically demonstrated in the satellites orbital distribution. The average orbital eccentricity of the satellites was found to be $e \approx 0.6$ with minimal scatter ($\sigma \approx 0.2$). Moreover, the average pericentre distance of the satellites was $p \sim 35\%$ of the virial radius for all halos, again with minimal scatter ($\sigma \approx 0.1$). Satellites that were disrupted while orbiting within the host's virial radius were replaced with a mass-less tracer particle and hence we were also able to present their orbital parameters at redshift $z = 0$. We found that even though they have smaller eccentricities ($e^d \approx 0.34$) than the surviving ones, their pericentre distributions are nearly identical. Since the pericentre distributions of both surviving and disrupted satellites were similar, implication is that the disrupted satellites spend more time in the deeper regions of the potential well. As such, they experience stronger tidal forces for longer periods, and are thus being disrupted more readily. We also noticed that satellites with more orbits tend to have smaller eccentricities. Difficult to explain through the application of dynamical friction we attribute this to the satellite's response to the growing host halo.

In comparison to the host halo we also found that the satellite populations on average held approximately 10% of the host's mass, with the majority of that mass locked in the larger satellites.

Further, the local velocity bias at all radii is greater than one and this increases as we move closer to the halo centre. Since this is a characteristic for each of

our halos, it strengthens the case that this is a general pattern of the satellite population in dark matter halos. For the global velocity bias we find an average $\langle b_{v,\mathrm{global}} \rangle \sim 1.103 \pm 0.002$, a slight, but significant, positive bias. Further, if we restrict the global velocity bias calculation to satellites that have had at least one orbit we observe a 7% decrease in bias to $\langle b_{v,\mathrm{global}} \rangle \sim 1.021 \pm 0.002$. Thus when we just consider the "virialised" satellites, the bias nearly vanishes. Finally we recovered the $\sigma_v \sim M^{1/3}$ relationship between satellite velocity dispersion and halo mass.

Surprisingly, all the above stated results appear to be independent of the actual host halo and its history. We were unable to identify any trends with richness, triaxiality and/or formation time (other than the number of orbits). Such similarities are suggestive of potential additional underlying CDM universal laws.

Chapter 5

Anisotropy of Substructure Orbits

"I think it's one of the scars in our culture that we have too high an opinion of ourselves. We align ourselves with the angels instead of the higher primates."

- Angela Carter

5.1 Introduction

Observations of the distribution of bright elliptical galaxies within the Virgo galaxy cluster show a remarkable collinear arrangement (West & Blakeslee 2000). Moreover, this axis also appears to be part of a filamentary bridge connecting Virgo and the rich cluster Abell 1367. This phenomenon has already been recognized (Arp 1968; Bingegeli, Tammann & Sandage 1987) but only with accurate measurements of distance did it become possible to discriminate between this being a genuine three-dimensional structure or merely a chance alignment of galaxies. West & Blakeslee (2000) based their distances upon the surface brightness fluctuations method (cf. Blakeslee, Ajhar & Tonry 1999 for a recent review), concluding that not only were the brightest cluster members distributed anisotropically over the cluster, but the distribution of dwarf ellipticals was elongated in the same direction (Bingelli 1999). Plionis et al. (2003) investigated this substructure-cluster correlation statistically using 303 Abell clusters. They affirm that there is indeed such a signal and also that this signal is related to the dynamical state (and the environment) of the cluster.

Moreover, even on smaller scales – in galactic systems – there are clear observational indications that the distribution of the orbits of satellite galaxies is biased towards the galactic pole (Holmberg 1969) giving an anisotropic distribution. Zaritsky et al. (1997) found that satellites of (isolated) disk galaxies are scattered asymmetrically about the parent galaxy and aligned preferentially with the disk minor axis. At first this signal (dubbed the Holmberg effect) was only prominent for distances out to ∼50 kpc from the host (Holmberg 1969), but an analysis based on a much larger sample (cf. Zaritsky et al. 1993) of satellites extends it to 200 kpc (Zaritsky et al. 1997). This result is confirmed by a study of the satellites orbiting M31 (Hartwick 2000; Grebel, Kolatt & Brandner 1999). In addition, for the one galaxy where individual satellite orbits are known, the Milky Way, there is also evidence that that the orbits are preferentially polar (Zaritsky & Gonzalez 1999). This is derived from information based upon the alignment of satellites on the sky (Kunkel & Demers 1976; Lynden-Bell 1982), the orientation of the Magellanic Stream (Mathewson, Clearly & Murray 1974), the three-dimensional distribution of satellites (Majewski 1994; Hartwick 1996), and their actual velocities (Scholz & Irwin 1994).

All these observations clearly indicate that on scales spanning from galaxy clusters down to galaxies there is a signal indicating a correlation between the alignment of substructure and the shape of the gravitational potential this substructure moves in. However, the source of this alignment of satellites has been debated for a number of years, with two potential solutions suggested to explain this puzzling arrangement. If the distribution of in-falling satellites is initially spherical, then dynamical selection may preferentially destroy or suppress the star-formation in those on more equatorial orbits[1]. For instance, Peñarubbia, Kroupa & Boily (2002) have argued that in flattened dark matter halos, the timescale for dynamical friction is substantially longer for satellites that are on polar orbits. Alternatively, the present non-isotropic distribution of satellite systems may reflect the fact that it has always been non-isotropic, with the satellites being accreted along preferred directions. These hypotheses can be readily tested in numerical simulations of structure formation. However, in previous attempts to decipher this signal from cosmological N-body simulations there still remains a certain amount of uncertainty (Zaritsky et al. 1997).

[1]With *equatorial* we mean "perpendicular to the major axis"

The first fully self-consistent simulations targeting the subject were performed by Tormen (1997). They though lacked resolution in time, space and mass to perform a detailed analysis of the satellite population for differing environments, and hence more refined simulations are required. Tormen (1997) could not follow the satellite distribution within the host's virial radius but rather tracked all progenitors prior to accretion. This allowed him to analyse the in-fall pattern rather than the orbital evolution of the satellites.

In this chapter we investigate the anisotropy of satellite orbits within our simulations. The brief outline of the chapter is as follows. We first discuss the orbital alignment with host halo axis in Section 5.2. Following that we investigate the connection between the large-scale structure and our sub-halo populations in Section 5.3. We then hypothesise a solution to the Holmberg effect in Section 5.4 and make our concluding remarks in the final Section 5.5.

5.2 Orbial alignment with host halo

Figure 5.1 presents the (normalized) distribution of angles between $\vec{R}_{\rm sat}^{\rm apo}$ and $\vec{E}_{1,\rm host}$. $\vec{E}_{1,\rm host}$is derived by the triaxiality of the host system (cf. Section 2.4.2). This graph shows that there is a clear trend in at least six of the eight halos for the two vectors to be aligned (the distribution peaks at 0° and 180°, respectively) meaning that the orbits of the satellites are preferentially found along the major axis of the host.

Figure 5.2 shows the (normalized) distribution of angles between the angular momentum vector $\vec{L}_{\rm sat}^{\rm apo}=\vec{R}_{\rm sat}^{\rm apo}\times\vec{V}_{\rm sat}^{\rm apo}$ of the satellite at its last apocenter and $\vec{E}_{1,\rm host}$, clearly revealing evidence for these two vectors to be parallel (distribution peaks at 90°). We like to stress that only satellite galaxies that at least had one or more complete orbits were taken into account in Figure 5.1 and Figure 5.2; the figure is *not* based upon the in-fall pattern of satellites as investigated by, for instance, Tormen (1997). We also need to stress that the distributions presented in that Figure are normalized, i.e. they are corrected for the bias introduced by plotting them as a function of the angle θ rather than $\cos\theta$. The data is binned equally spaced in angle ranging from 0° to 180°, and therefore the area probed on the sphere varies with θ. Further, the distribution needed to be normalized by the the respective area A specified by the actual range of angles $[\theta-\Delta\theta/2, \theta+\Delta\theta/2]$. This area is proportional to $A \propto \cos(\theta-\Delta\theta/2) - \cos(\theta+\Delta\theta/2)$.

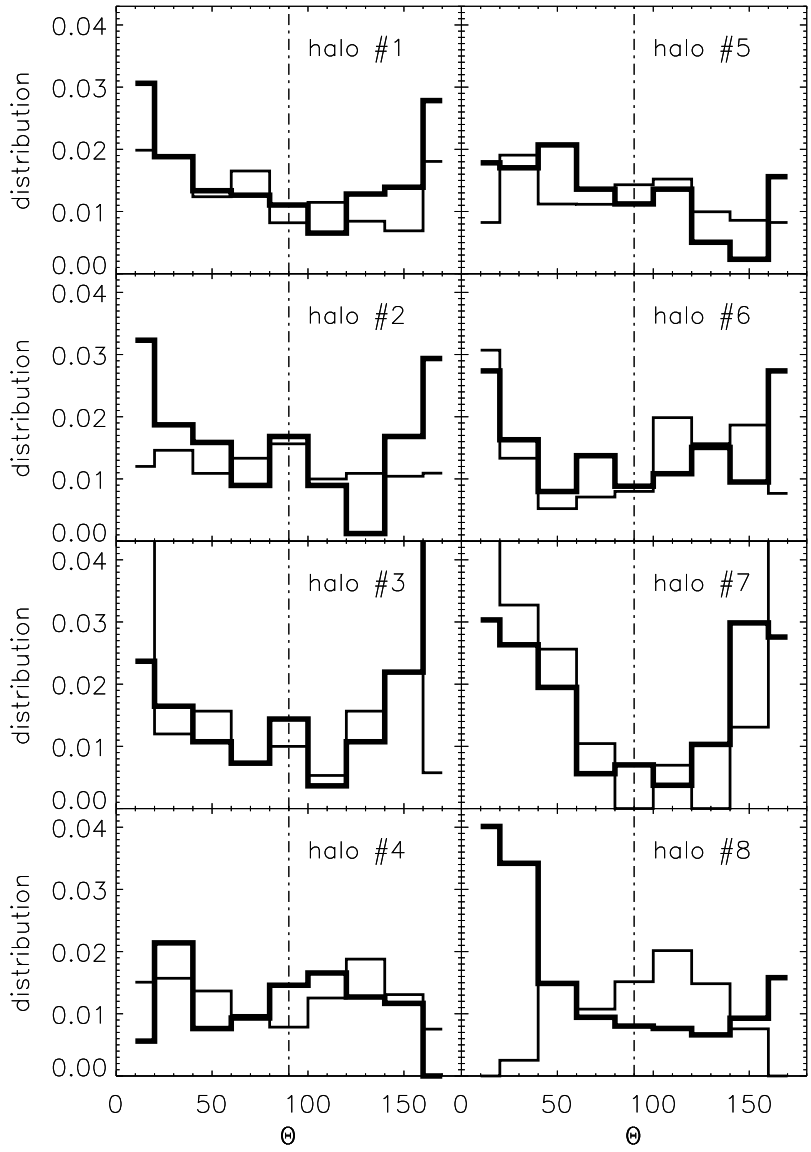

Figure 5.1: Satellite alignment with the the principal axis of the host
The (normalized) distribution of angles between position vector $\vec{R}_{\rm sat}^{\rm apo}$ of the satellites measured at the last apocentre and the major axis $\vec{E}_{1,\rm host}$ of the halo. θ values of 0° and 180° indicate alignment with the the principal axis of the host. The thin histogram show the disrupted satellites. Only satellites more massive than $2 \times 10^{10} h^{-1}$ $\rm M_\odot$ (100 particles) that had one full orbit were taken into account.

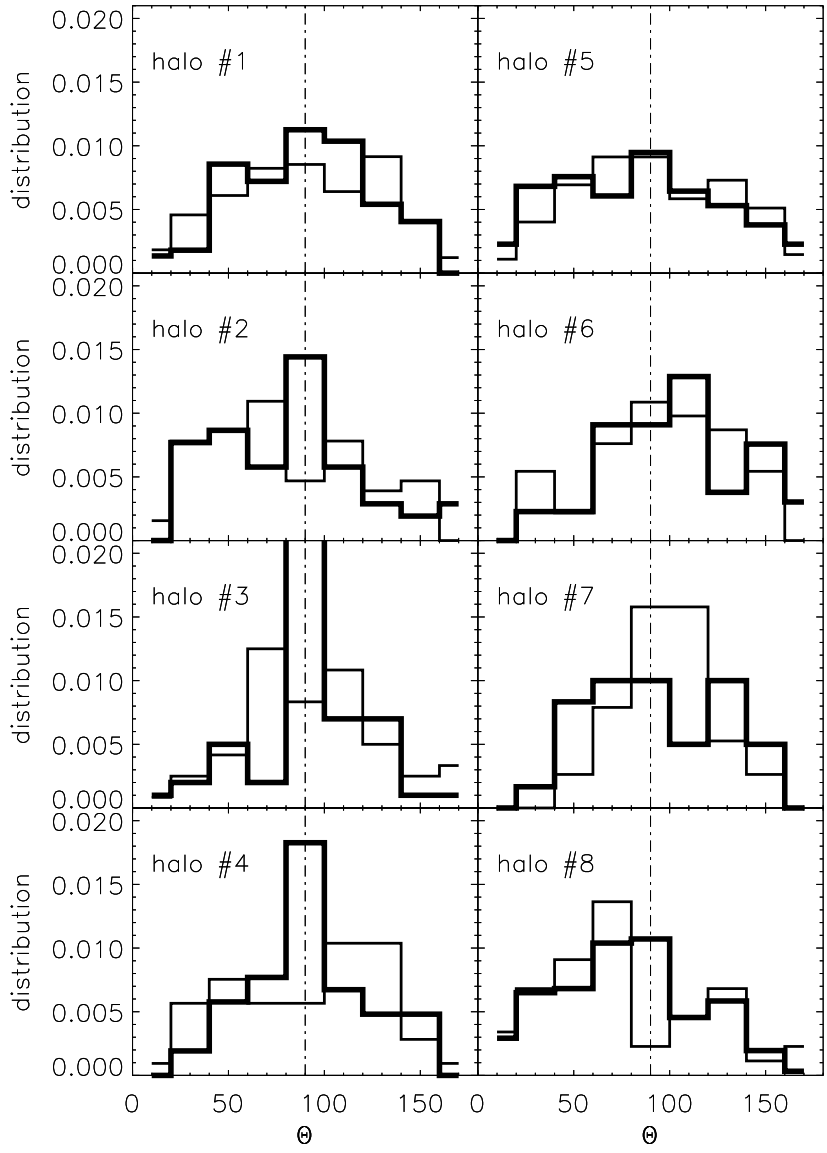

Figure 5.2: Satellite orbital plane contains the major axis of the host
The right panel shows the (normalized) distribution of angles between angular momentum vector $\vec{L}_{\rm sat}^{\rm apo}$ of satellites measured at the last apocentre and the major axis $\vec{E}_{1,\rm host}$ of the halo. A θ value of 90° means that the orbital plane of the satellite contains the major axis of the host where θ of 0° and 180° would require for the plane to be perpendicular to the host's principal axis. The thin histograms are for disrupted satellites. Only satellites more massive than $2 \times 10^{10} h^{-1}$ $M_\odot$ (100 particles) that had one full orbit were taken into account.

As outlined in the introduction to this Chapter there are two possible scenarios that explain the substructure-cluster alignment found in observations of galaxy clusters (Plionis et al. 2003; West & Blakeslee 2000) and the analysis of N-body-simulations presented in this study. Either some dynamical process can be held responsible, meaning that initially the orbits were randomly distributed and only some satellites survive to give rise to the observed correlation in Figure 5.1 and Figure 5.2, or alternatively, their orbital parameters are imprinted upon them at the time they enter the host halo as already pointed out by Tormen (1997).

"Dynamical destruction", whereby satellites on more equatorial orbits suffer more tidal disruption, can be rejected because a comparable (although not as pronounced) alignment signal is found when restricting the analysis to those satellites that are in fact disrupted: We placed mass-less tracer particles at the last centre of the satellites before they were classified "disrupted". These "disrupted systems" are presented as the thin lines in Figure 5.1 and Figure 5.2.

We therefore conclude that it must be the initial distribution of the satellite systems that is responsible for the present day alignment. For example, galaxies are "funnelling along the filaments" (Kitzbichler & Saurer 2003) which has also been confirmed by X-ray observations of the spatial distribution of substructure in galaxy clusters (West, Jones & Forman 1995) and biases the types of possible orbits.

5.3 Alignment with large-scale structure

It would now be reassuring to confirm a link between the host halo shape and the surrounding environment, i.e. are the filaments that feed the halo with material preferentially angled with respect to the orientation of the host halo? When projecting the positions of the satellites onto a sphere at the time they enter the virial radius of the host it is clear that they are not randomly distributed; they cluster in directions linked to the filamentary structure surrounding the host halo, as found before observationally (e.g. West & Blakeslee 2003; Plionis & Basilikos 2002, and references therein) and in N-body-simulations (e.g. Faltenbacher 2002; Hatton & Ninin 2001; Onuora & Thomas 2000; Colberg et al. 1999; Splinter et al. 1997; Tormen 1997). Tormen (1997) already pointed out that there is a strong alignment between the distribution of in-falling satellite galaxies and the shape of the dark matter host. However, Tormen's simulations did not have the spatial and mass resolution to in-

vestigate the orbits of satellites *within* the host halo. We are, for the first time, tracing the dynamics of the satellites within the dark matter hosts confirming that the alignment for both, disrupted and surviving, satellites is maintained for several orbital periods. Figure 5.3 now presents a visual impression of the trajectories of all surviving satellites identified at formation time of host halo #3 until redshift $z = 0$, qualitatively supporting the scenario that these orbits are linked to the filamentary structure which will leave its imprint in observed anisotropy.

Plionis et al. (2003) also established a link between the alignment and the dynamical age of the clusters. Our simulations though show that this finding can not be generalized: both our oldest halos, in which the satellites had as many as 4–5 orbits, do show the correlation signal. We do not observe a trend for a "randomisation" of the orbits in older halos. The satellites actually preserve the alignment with the host they had when they first fell into the cluster.

5.4 Holmberg effect

In Section 5.1 we showed that the (observational) substructure-alignment signal spans from galaxy clusters down to galactic scales. Our results are mostly applicable to the former, and any extrapolation to smaller scales has to be handled with care. In the case for galaxies, for instance, the interaction between the galactic disk and the incoming satellite could enhance destruction in the galaxy plane, i.e. satellite on prograde orbits decay faster than the ones on retrograde (or polar) orbits due to orbital resonances between the disk and the satellites (Peñarubbia, Kroupa & Boily 2002). Based on theoretical and numerical studies (cf. Lacey & Cole 1993 and Moore et al. 1999) it should be possible to re-scale our simulations to a Milky Way sized object by requiring that the maximum of the circular velocity curves of our halos equals 220 km s^{-1}. The scaling factor lies in the range of about 4–5 (cf. $v_{\rm circ}^{\rm max}$ values in Table 2.5) and hence our "rescaled dark matter halos" would correspond to the ones in the observational data with virial radii in the range 260–295h^{-1} kpc. This scaling factor in length entails a scaling in mass of 64–125 (simply the length scale to the power of three). This brings the mass of our galaxy clusters down to $\sim 10^{12} h^{-1}$ M$_\odot$ which agrees with the dark matter mass inferred for our Milky Way (Freeman 1996). More problematic, however, are the ages of our systems: our halos are only $\leq$8.3 Gyrs old opposed to 12 Gyrs for the Milky Way. Satellites in the

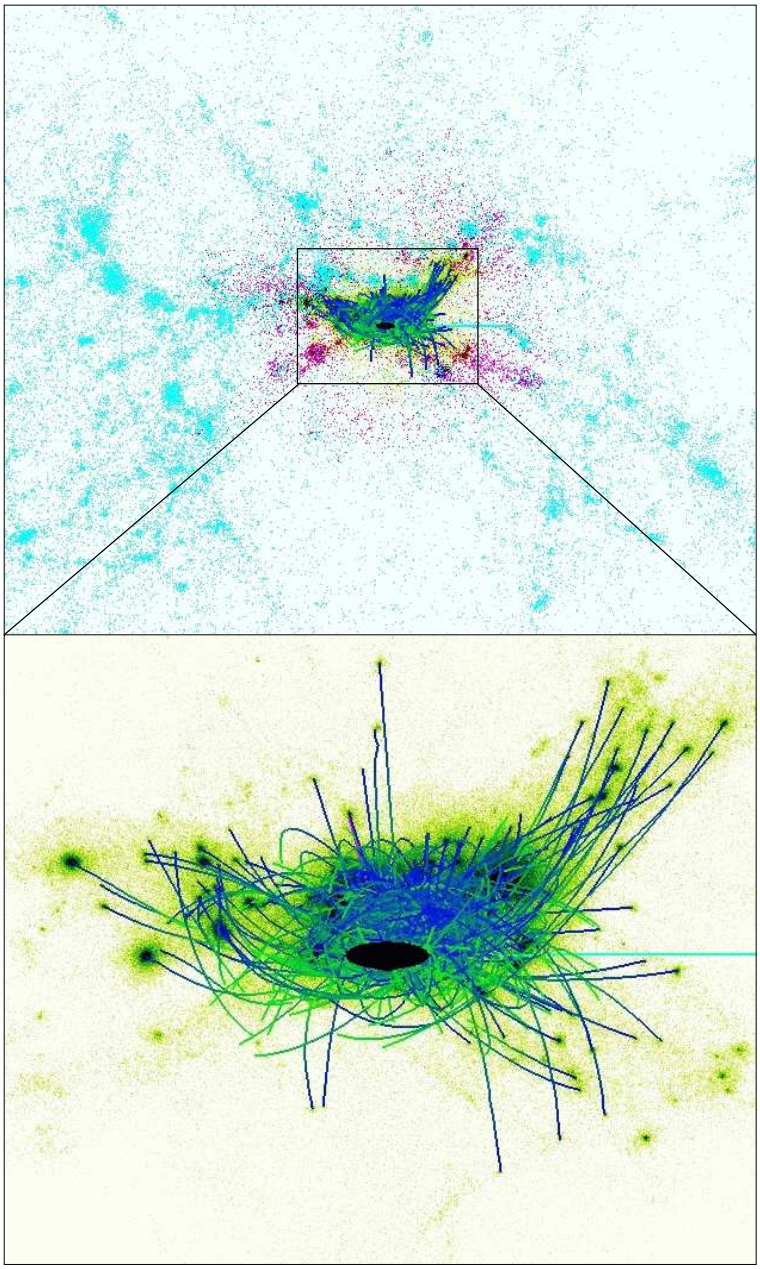

Figure 5.3: Alignment with immediate large-scale structure
Orbits of all satellite galaxies identified at formation time (dark) to redshift $z = 0$ (light). The left panel shows how the host halo fits into the surrounding large-scale structure presented at formation time. The right panel zooms into the region marked in the left panel, this time not showing low-resolution particles. The shape (and position) of the underlying host halo at redshift $z = 0$ is indicated by the best-fit ellipse to the grid used to calculate its triaxiality. The vertical line extending to top edge of panel indicates the principal axis of the host. With the assumptions presented in this paper, the pole of the host galaxy within the dark matter halo is aligned with this principle axis.

Milky Way had the chance to complete nearly twice as many orbits leaving more space for an explanation based upon the dynamical destruction scenario.

When re-scaling our data, putting aside the age issue, and trying to explain the Holmberg effect, another uncertainty comes into play: the orientation of the stellar disk. In a triaxial potential there are in general stable closed orbits about both the major and the minor axis (e.g., Binney & Tremaine 1987). So, in principal the disk plane could either be perpendicular to the major or perpendicular to the minor axis. Under the assumption it lies perpendicular to the major axis of the dark matter halo the satellites in our simulations will be on polar orbits. There are indications that this configuration results in the most stable disk configuration within a triaxial halo (Hayashi et al. 2003). Moreover, even though there are clear indications that the angular momentum of the dark matter is well aligned with the minor axis of the halo (e.g. Warren et al. 1992), van den Bosch et al. (2002) showed that the angular momentum of the baryonic component (i.e. gas) not necessarily follows that of the dark matter distribution. They found an average misalignment between $\vec{L}_{\rm gas}$ and $\vec{L}_{\rm DM}$ of the order of 40° in their numerical simulations. Hence the orientation of the galactic disk with respects to the dark matter halo is not well determined. Turning to observations does not resolve this question, with studies of polar rings indicating strongly oblate halos (i.e. Iodice et al. 2003), while others suggest dark matter halos are more spherical, or even oblate (Olling & Merrifield 2000; Ibata et al. 2001). The situation is not at all clear, but the assumption that disks are perpendicular to the major axis (which is in agreement with results presented by Hayashi et al. 2003) would provide an explanation for the Holmberg effect, even though this is a very speculative interpretation.

5.5 Conclusion

In conclusion this chapter presented an analysis of our cosmological simulations that focused on the relationship between the orbits of satellite galaxies and their host halos. We show that the apocentres of the orbits of these satellites are preferentially found within a cone of opening angle ∼40° around the major axis of the host halo, in accordance with the observed anisotropy found in galaxy clusters. We do, however, note that a link to the dynamical age of the cluster is not well established as both our oldest dark matter halos do show a clear anisotropy signal. Further analysis

connects this distribution to the in-fall pattern of satellites along the filaments. Thus we therefore conclude that the satellite orbits are determined by their initial distribution i.e. the large-scale structure rather than some "dynamical selection" during their life within the host's virial radius.

Since the publication of this chapter as a paper there has been an ongoing discussion in the literature.

Lee & Kang (2005) applied similar ideas to develop an algorithm for reconstructing the triaxial shapes of dark matter halos from the anisotropic spatial distributions of sub-halos.

Zentner et al. (2005) extended our work from clusters to galaxies and found the same results on galactic scales, which smaller and more dynamically evolved systems.

Zentner's result strengthens our explanation of the origins of the Holmberg effect. However, Balin et al. 2005 showed that the galactic disks do not align with the major axis of the dark halo, which would make this interpretation of the Holmberg effect contradictory.

This is emphasised by additional recent observational results. Sales & Lambas (2004) analysed the 2dF Galaxy Redshift Survey finding strong statistical evidence of the Holmberg effect. However, Brainerd (2004) analysed the distribution of satellite galaxies relative to isolated host galaxies in the Sloan Digital Sky Survey (SDSS) finding significant anisotropy with satellites aligning with the major axes of the hosts thus in stark contrast to the Holmberg effect and in favour with our results.

There obviously needs to be more research to be done to finally resolve the mystery of the Holmberg effect.

Chapter 6

Outskirts of Dark Matter halos

"When you talk with me about my research, do not ask me what I found; I found nothing. Ask me what I invented, what I made up from and out of my data."

- Sandelowski (1994)

6.1 Introduction

The relationship between galaxy morphology and local environment (i.e. the morphology-density relation) was first noticed by Hubble & Humason (1931), where they reported that field and cluster galaxy populations differ. Oemler (1974) extended this finding by showing that the relationship held for differing clusters richness. The field truly emerged when Dressler (1980) demonstrated the strong relationship over five orders of magnitude between the local density of galaxies and the proportions of different morphological types. Bhavsar (1981), de Souza et al. (1982), and Postman & Geller (1984) extended this work further to include the environments of both loose and compact groups. Recently, Aguerri et al. (2004) performed a thorough analysis of 116 bright galaxies in the Coma cluster, finding that bluer objects are located at larger projected radii while simultaneously showing a larger velocity dispersion than their red counterparts. Moreover, the bluest objects also host the most prominent disks contrary to systems observed close to the cluster centre or in high-density environments. Environmental dependence of galactic stellar populations is also seen in the Butcher-Oemler effect (Butcher & Oemler 1978, Kodama & Bower 2001) with

clusters at higher redshifts showing a greater fraction of blue objects than are seen at present.

The above observational work supports the idea that galaxies in clusters are substantially different from galaxies in the field. But the origins of these morphology-density relationships are still not fully understood with several large and small scale mechanisms proposed to explain their existence, including ram pressure stripping (Gun & Gott 1972), tidal stripping/star formation (Merritt 1983, 1984), starvation (Larson, Tinsley & Caldwell 1980), galaxy merger and harassment (Icke 1985; Moore et al. 1996) and dynamics (Tsuchiya & Shimada 2000).

Recent cosmological simulations (both hydrodynamical and N-body) have provided valuable insight into the mechanisms responsible for the morphology-density relationship (Springel et al. 2001; Goto et al. 2003; Okamoto & Nagashima 2003). In the analysis which follows, we focus on the dynamics of satellite galaxies as described in Chapter 2. But now we concentrate on the outskirts of these clusters, i.e. distances in the range $[R_{vir}, 2.5R_{vir}]$, which (observationally) have only recently been probed through wide-field optical imaging and spectroscopy (Miyazaki et al. 2002; Lewis et al. 2002). We will demonstrate that a rich population of galaxies exist beyond the virial radius most of which have previously spent time near the cluster centre. We characterise the spatial, velocity and mass properties of this population and contrast these with those of the spatially coincident newly in-falling galaxies.

Our work complements the earlier studies of Balogh et al. (2000) and Mamon et al. (2004). Balogh et al. investigated the *particle* "backsplash" from cosmological simulations and found that $50 \pm 20\%$ of the particles within $[R_{200}, 2R_{200}]$ had passed through the R_{200} radius. Mamon et al. recently extended this work to calculate the maximum backsplash distance for particles to be $2.5R_{100}$ and for galaxies $1.7R_{100}$.

For later reference and comparison to previous studies by Balogh et al. (2000) and Mamon et al. (2004) we relate R_{vir} to other definitions of the virial radius, namely R_{200} and R_{100}. According to the NFW profile (Navarro, Frenck & White 1997) the dark matter density in the outer regions of halos drops like $\rho \propto r^{-3}$ and hence $R_{vir} \sim 1.4R_{200}$ and $R_{vir} \sim R_{100}$.

The outline of this chapter is as follows. We investigate the number distribution of galaxies in the cluster outskirts in Section 6.2, with the mass distribution discussed in Section 6.3 and the velocity distribution of the satellites investigated in Section 6.4. We finish with our summary and conclusions in Section 6.5.

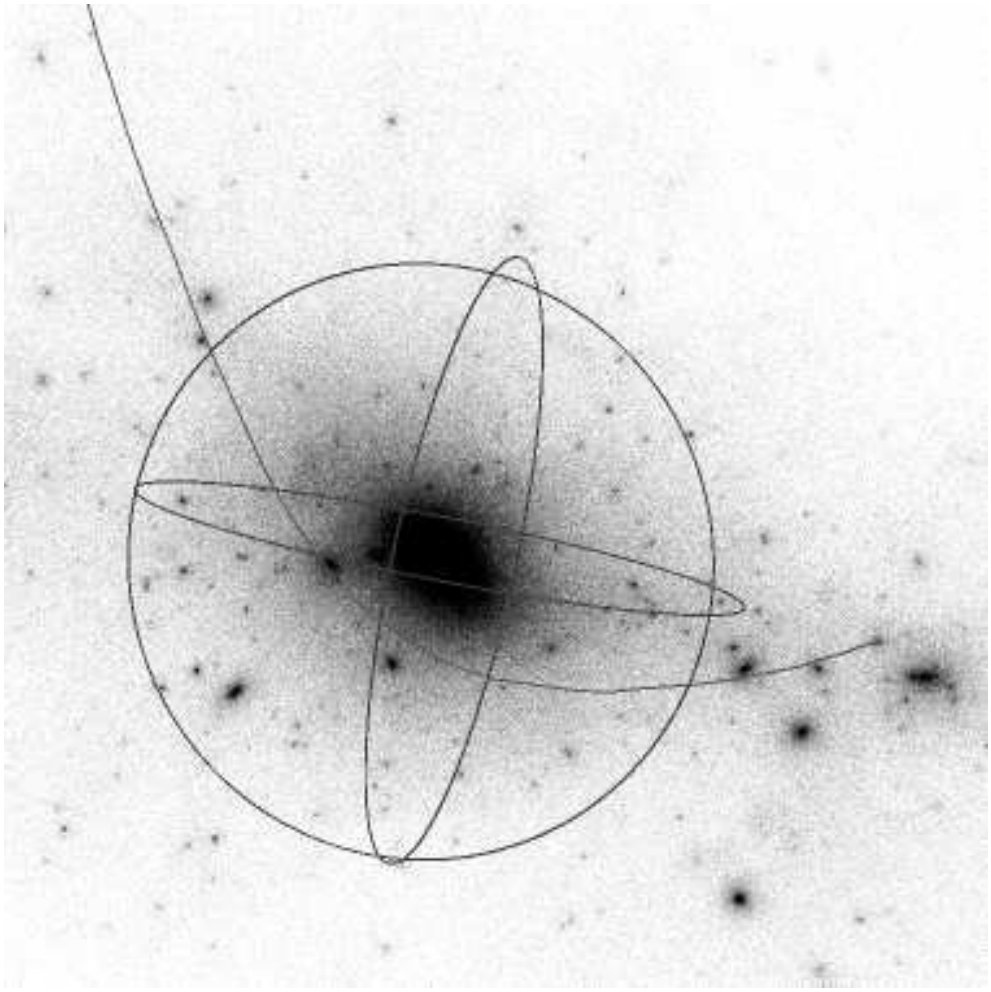

Figure 6.1: Image of a "backsplash" galaxy

A simulated cluster at z=0 with the virial radius indicated by the dark sphere. The other line in this figure represents the orbital path of a "backsplash" galaxy. Such a galaxy has previously spent time near the cluster centre but now lies outside the virial radius of the cluster.

6.2 Number distribution of galaxies

The fact that galaxies in clusters are different from galaxies in the field has been attributed to a variety of mechanisms acting on a variety of scales. It has been suggested that galaxies can "rebound" up to $1.7R_{100}$ (Mamon et al. 2004), thus blurring the definition of "cluster" and "field". In this section we investigate cluster galaxy "backsplash": how significant is the population of galaxies that once passed through a cluster's virial radius but now resides in its outskirts?

In Figure 6.2 we plot for all of our eight simulated clusters the minimum distance $D_{\rm min}$ a galaxy reached to the cluster centre throughout its history versus its current distance $D_{z=0}$. Both distances have been normalised by the cluster's present day virial radius $R_{\rm vir}$. There are four distinct populations of satellites visible in this figure:

1. $D_{\rm min} = D_{z=0}$: (the infalling population)
These satellites are falling in for the first time.

2. $D_{\rm min} > R_{\rm vir}$ and $D_{z=0} > R_{\rm vir}$: (infalling sub-population)
This population is made up of subhalos orbiting satellites, i.e. sub-subhalos.

3. $D_{\rm min} < R_{\rm vir}$ and $D_{z=0} > R_{\rm vir}$: (backsplash satellites)
These satellites once passed through the virial radius of the respective host but have "rebound" to the outskirts of the galaxy cluster.

4. $D_{\rm min} < R_{\rm vir}$ and $D_{z=0} < R_{\rm vir}$: (the bound population)
This is the "normal" satellite population orbiting within the virial radius and bound to the host.

Our data sets indicates that the maximum backsplash distance encountered is $\sim 2.5R_{vir}$ which is larger than the value presented in Mamon et al. (2004)[1] yet not widely in disagreement, further very few backsplash galaxies exist beyond $\sim 2R_{vir}$.

A more quantitative analysis reveals that 30% of all satellites with $D_{\rm min} < R_{\rm vir}$ are outside the host's virial radius at $z = 0$. Further, 50% of all galaxies with a current distance $D_{z=0}$ in the range $[R_{\rm vir}, 2R_{\rm vir}]$ are in fact backsplash galaxies, consistent with the value 50 ± 20 % quoted by Balogh et al. (2000) (based on cluster particles as opposed to gravitationally bound satellites though).

[1] refer to the end of Section 6.1 for conversion of $R_{\rm vir}$ to R_{100}.

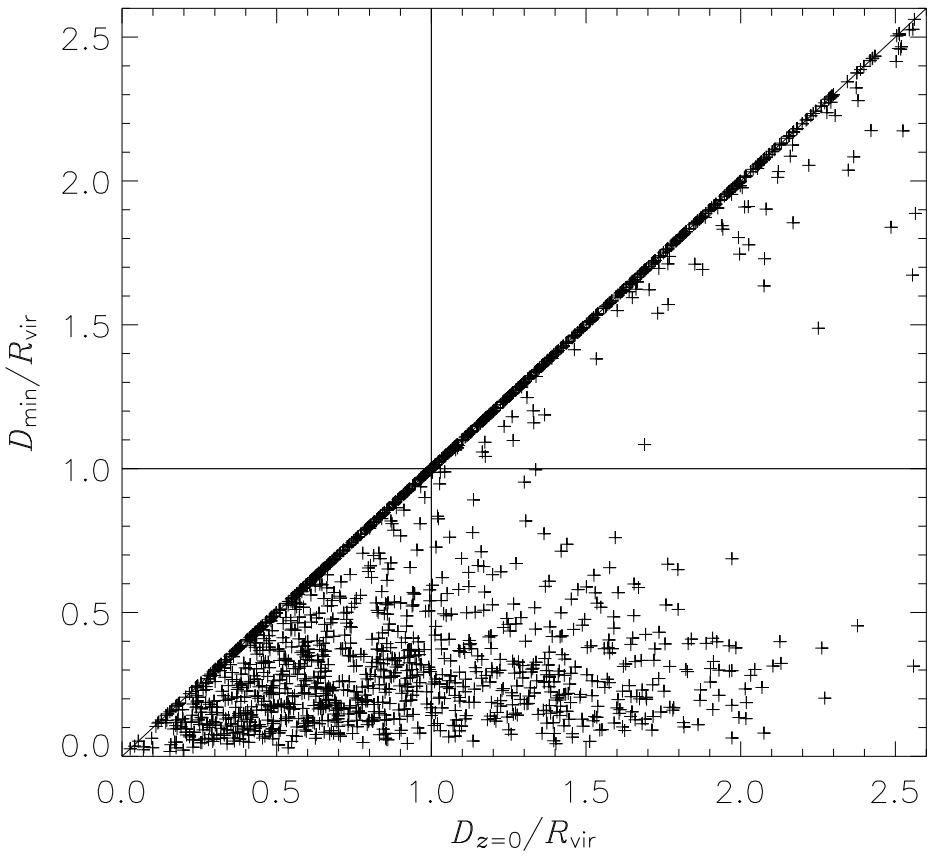

Figure 6.2: Minimum distance for all satellite galaxies versus current distance
Minimum distance for all satellite galaxies versus current distance in terms of the host's virial radius. The population in the upper right corner consists of substructure orbiting within satellites, i.e. sub-subhalos. This figure clearly indicates that there is a distinct population of "backsplash" satellites, i.e. $D_{\rm min} < R_{\rm vir}$ and $D_{z=0} > R_{\rm vir}$ in the lower right corner.

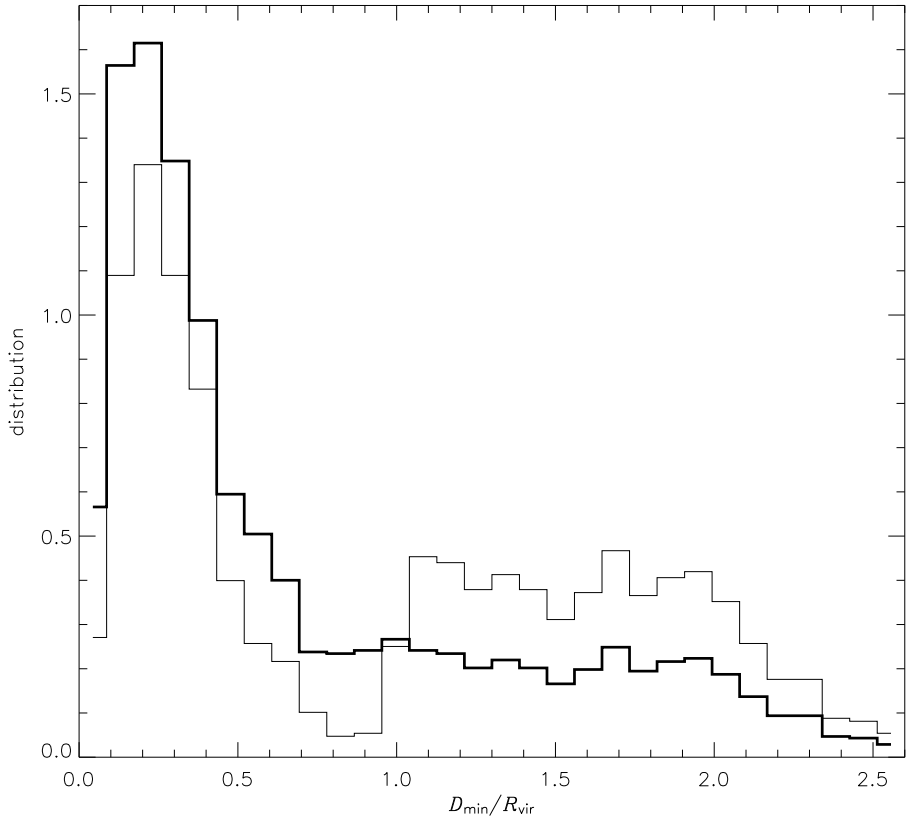

Figure 6.3: Normalised distribution function of galaxy minimum distance
The relative normalised distribution function of the minimum distance $D_{\rm min}/R_{\rm vir}$ for the whole galaxy population (thick histograms) and the satellites with current positions greater than the virial radius (thin histograms). We note that they both peak near 25% of the cluster virial radius.

Only 2% of the backsplash population has had more than one orbit (i.e. eight satellites in total) and most stem from single passages through the host's virial radius, respectively. And each of these eight "multiple passage" backsplash galaxies are found in the range $[R_{\rm vir}, 1.2R_{\rm vir}]$ which is close to the host.

We now investigate the depth to which backsplash galaxies penetrate the cluster potential. To this extent we plot in Figure 6.3 the normalised number distribution of the minimum distance $D_{\rm min}$ for the entire satellite population (thick histogram) and the restricted set of satellites currently outside the virial radius (thin histograms). It is interesting to note that the distributions are fairly similar for $D_{\rm min} < R_{\rm vir}$, i.e. they both peak near 0.25. We stress that this is the minimum distance as measured over the lifetime of the host halo and hence is not to be confused with the last pericentre whose distribution peaks at about 35% of $R_{\rm vir}$ (cf. Chapter 4). Figure 6.3 reveals that the a number of the galaxies that are now in the outskirts of the cluster have had passages as close to the host as their bound counterparts which implies that the former are on highly radial orbits. This is consistent with the findings of Solanes et al. (2001) who found evidence that gas-poor spirals in HI deficient clusters move in orbits more radial than those of the gas-rich objects. In fact, 90% of our backsplash satellites once passed within the inner 50% of the virial radius.

In summary the number of backsplash galaxies is significant and should be accounted for when interpreting the galaxy morphology-density relationship. These galaxies penetrate deep within the cluster potential, as deep as their bound counterparts. Hence, they should be sampling the large and small-scale transformation mechanisms alluded to in the introduction. For example, if we used the prescriptions outlined in Treu et al. (2003), these galaxies would also have undergone starvation, ram pressure stripping, tidally triggered star formation and significant tidal stripping, thus confusing any correlation of the galaxy's morphology with local environment.

6.3 Mass distribution of the galaxies

One way to gauge the significance of these transformation mechanisms is to investigate the mass loss of a galaxy during its encounter with the cluster. To this extent we focus only on the backsplash population and plot the relative mass lost over the

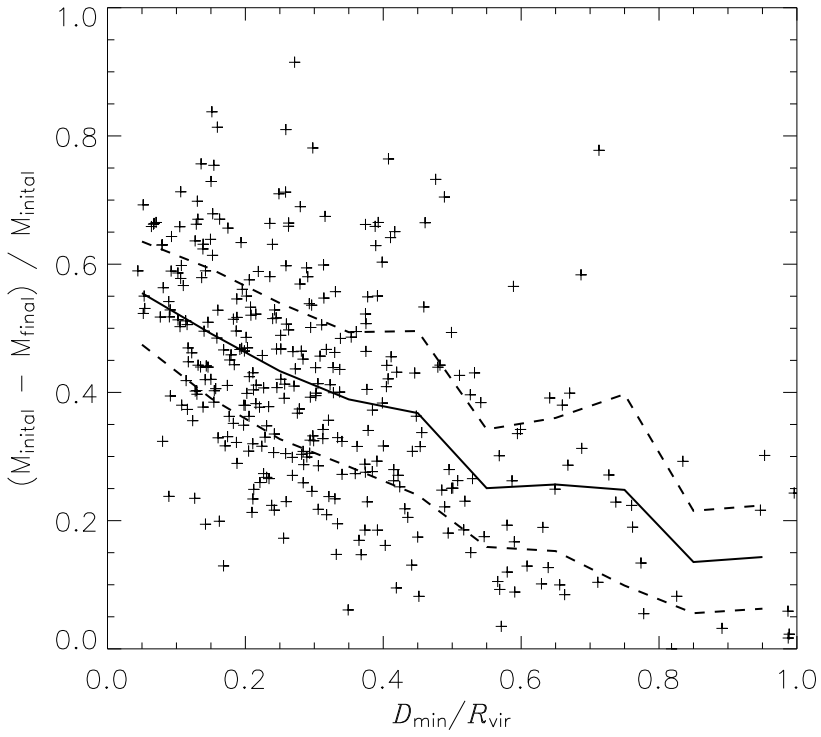

Figure 6.4: Relative mass loss for "backsplash" galaxies as a function of minimum distance
Relative mass loss for the "backsplash" galaxies over the lifetime of the host as a function of minimum distance (normalised by the cluster radius). The solid line shows the average with the dashed lines being the standard deviation.

lifetime of the host as a function of minimum distance $D_{\rm min}/R_{\rm vir}$ for each of these satellite in Figure 6.4. We find that the closer a satellite gets to the host the stronger the tidal stripping. This result is not surprising but needs to be viewed from the perspective of the backsplash population: galaxies in the outskirts experienced significant tidal interactions and mass loss, in some cases up to 80% of their original mass.

Further to that, we see little dependence of *present day* clustercentric distance on the mass lost as can be seen in Figure 6.5. At all distances outside the virial radius the average mass lost for each backsplash galaxy is $\sim 40\%$.

Since the population of backsplash galaxies has undergone significant tidal stripping we expect the mass spectrum to be different from that of the galaxies in-falling for the first time. In Figure 6.6 we plot the relative number distribution of satellites

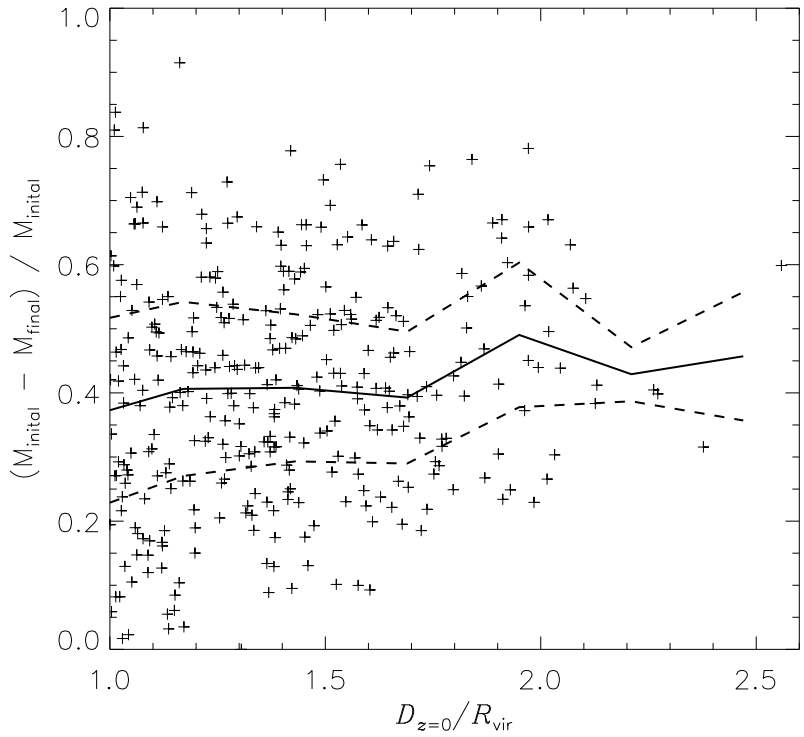

Figure 6.5: Relative mass loss for "backsplash" galaxies as a function of current position

Relative mass loss for the "backsplash" galaxies over the lifetime of the host as a function of current position (normalised by the cluster radius). The solid line shows the average with the dashed lines being the standard deviation.

with a certain mass $M_{\rm sat}$ measured in terms of the host's virial mass $M_{\rm host}$. The thin histogram represents the backsplash population and the thick histogram shows the in-falling population. To better discriminate between these two populations we fitted the mass spectra to a simple power-law

$$n(M) = CM^{\alpha} \tag{6.1}$$

There is a marginal difference between the slopes, the backsplash population having $\alpha = 0.9 \pm 0.3$ whereas the in-falling satellites distribution is characterised by $\alpha = 0.7 \pm 0.3$. The steeper slope of the backsplashed galaxies reflects the lack of larger satellites and an over-abundance of smaller galaxies, respectively. This tilt in the mass spectrum is readily explained by the mass loss highlighted in Figure 6.4. We note that the first mass bin was not used in fitting the power-law as it simply reflects the *absolute* mass cut of $2 \times 10^{10}\ h^{-1}\ \mathrm{M}_{\odot}$ (i.e. we did not use a relative mass cut with respect to the mass of the host).

6.4 Velocity properties of backsplash galaxies

To populate the outskirts of clusters, galaxies that once passed through the virial radius and close to the centre of the host must have had high velocities. In this section we explore the relative velocities of satellite galaxies within the cluster and its outskirts.

6.4.1 A kinematically distinct backsplash population

Figure 6.7 shows the absolute value of the relative velocity between a satellite galaxy and the host cluster as a function of current clustercentric distance. We present the results for two populations again, namely the in-falling satellites that are still outside the virial radius (diamonds) and the backsplash galaxies alongside galaxies within the virial radius (crosses).

At the virial radius the maximum relative velocity for a galaxy in our data set is 1500 km s^{-1} with no galaxy farther away having a greater velocity. This finding can be used to explore the two competing models for the ram-pressure stripping observed in NGC 4522, a spiral galaxy in the Virgo cluster with a distance close to the virial radius (Vollmer et al. 2001). Kenney et al. (2004) suggested two possible scenarios to

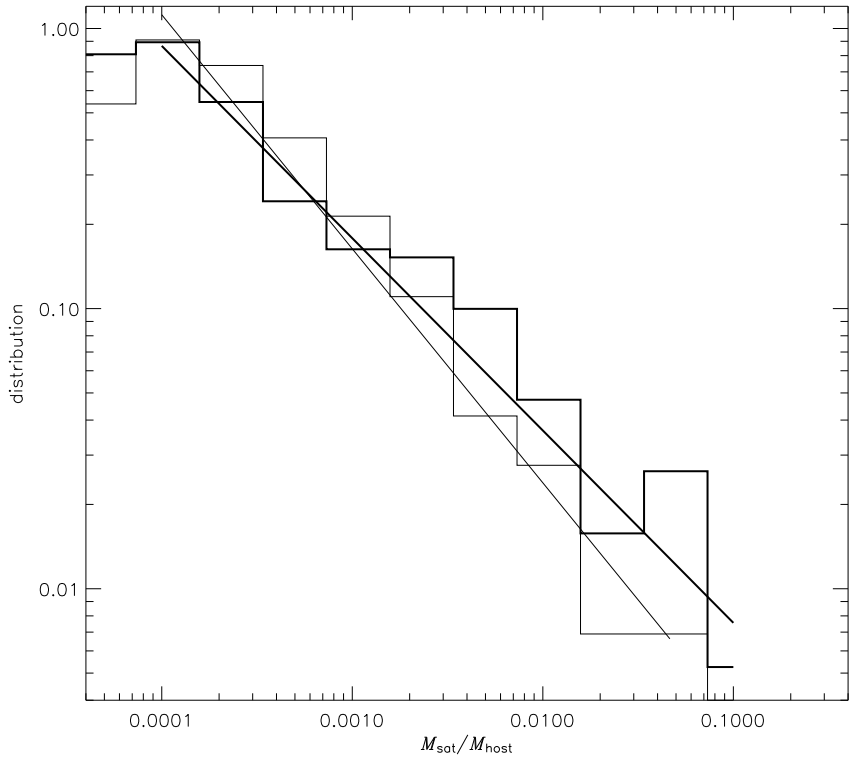

Figure 6.6: The relative number distribution of satellite masses
The relative number distribution of satellite masses. The thin histogram represents the backsplash population and the thick histogram shows the satellites in-falling for the first time.

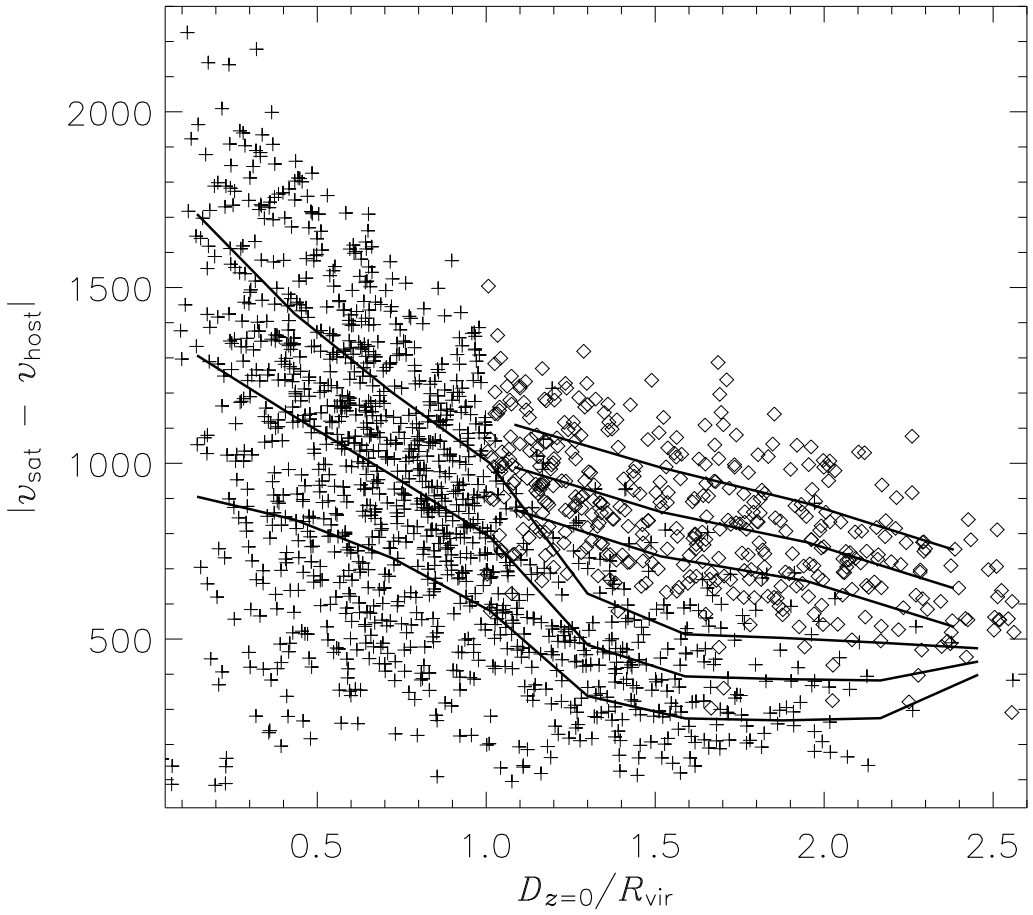

Figure 6.7: Absolute relative velocity for the in-falling satellites
The absolute value of the relative velocity for the in-falling satellites (diamonds) and the population of satellite that have crossed the virial radius at sometime (crosses) as a function of current cluster distance to the host. The middle solid lines represent averages with the outer lines being the standard deviations. Note the kinematic distinction between the populations.

explain its ongoing ICM-ISM stripping: either NGC 4522 is experiencing stripping at this distance due to bulk motions and local density enhancements of the ICM produced by shocks in the ICM, or – since ram-pressure stripping is proportional to v^2 – the galaxy has a very high relative velocity, of order 4000 km s^{-1}. As hinted by Kenney et al., such a velocity is extremely unlikely, and as shown in Figure 6.7 only in the very central regions of clusters do galaxies reach these high relative velocities.

Figure 6.7 furthermore shows that the backsplash population is quite distinct kinematically; the in-falling satellites have significantly larger velocities than the backsplash galaxies. This provides a possible mechanism to observationally detect these rebound satellites.

To investigate this in more detail we divided all (in-falling and backsplash) satellites into three radial bins between 1 and 2 $R_{\rm vir}$. In Figure 6.8 we show the distribution of the relative velocities for all satellites in the respective bin (solid lines). The dotted (dashed) lines are for the backsplash (in-falling) population alone, normalised to the total number of satellites (i.e. the actual distribution is simply the sum of these two distributions). From the distributions presented in Figure 6.8 it is rather obvious that the backsplash population should be detectable by simply plotting the velocity distribution function (VDF) for cluster galaxies in the range $[R_{\rm vir}, 2R_{\rm vir}]$: there are two distinct peaks with the lower velocity peak indicative of the rebound satellites. Moreover, as we move further away from the host the separation between the two populations becomes even more pronounced.

One might still pose the question though, if the backsplash population can be identified by their "flight path", i.e. the orientation of their velocity vector. In Table 6.4.1 we therefore summarise the numbers of backsplash galaxies moving towards ("approaching") and away ("receding") from the centre of the host. This demonstrates that the backsplash galaxies cannot simply be selected by the direction of their velocity as they appear to move in both directions. However, as distance increases we do find a higher percentage of backsplash galaxies moving away from the host.

6.4.2 Observational impact

Thus far, we have relied upon the fact that our simulation data provides full six dimensional velocity and spatial information. In this section we extend the velocity distribution function to the "observer's plane" by restricting the data to projected

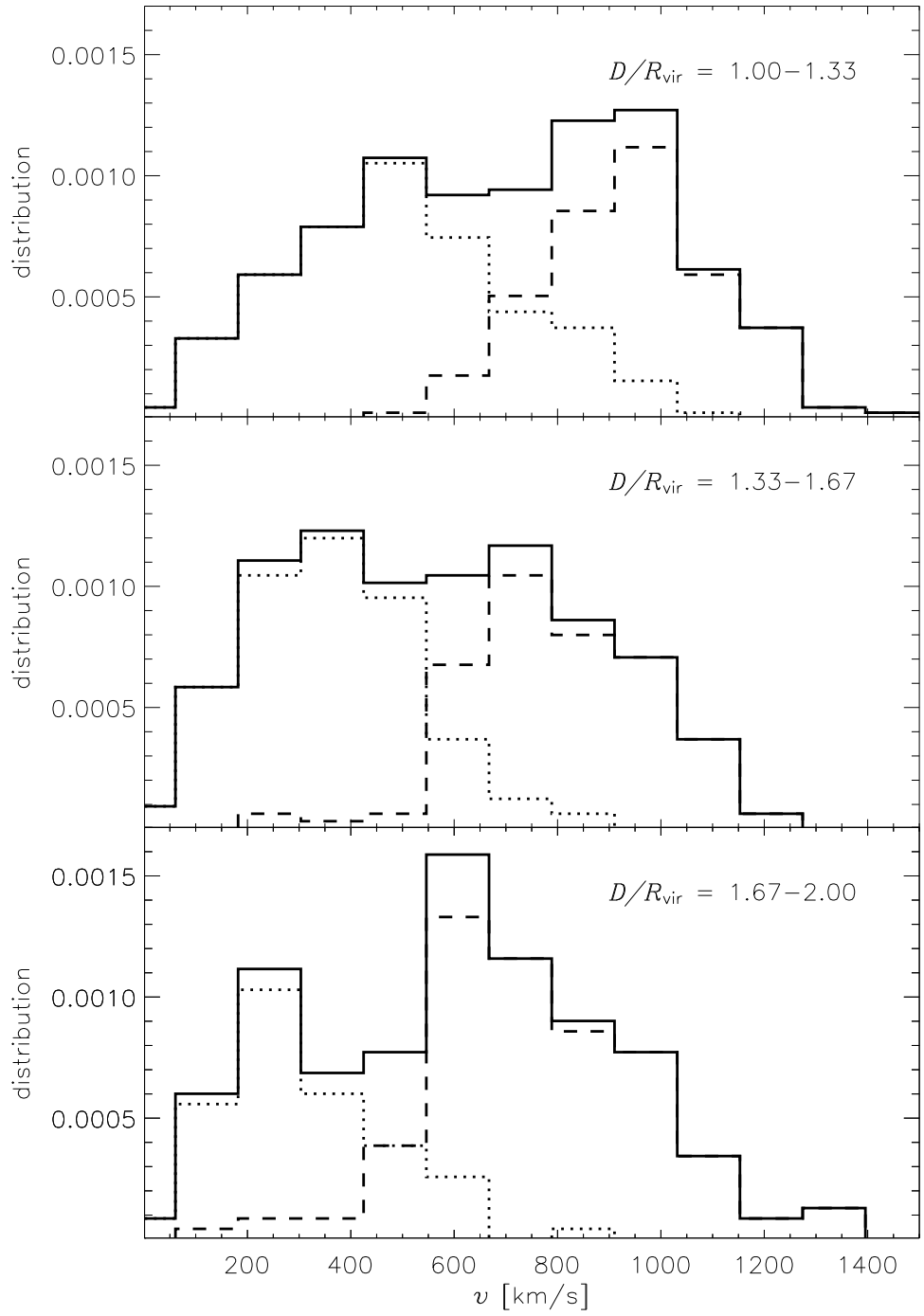

Figure 6.8: The distribution of the relative velocities

The distribution of the relative velocities in three distance bins, i.e. 1.00–1.33, 1.33–1.67 and 1.67–2.00 virial radii. The dotted histograms shows the backsplash galaxies while the dashed lines represent the in-falling galaxies (both normalized to the total number of satellites). The solid histogram is the sum of both distributions. We see that the distribution has two distinct peaks.

Table 6.1: Number of inbound and outbound backsplash galaxies in different radial bins.

distance ($R_{\rm vir}$)	receding galaxies	approaching galaxies
1.00 - 1.33	102	106
1.33 - 1.67	87	57
1.67 - 2.00	47	22

distances and line-of-sight velocities; we make this transformation by placing the potential observer at infinity.

In Figure 6.9 we show the distribution of the line-of-sight velocities (still with respect to the host) for galaxies with projected distances between 1.0 and 2.0 virial radii. Velocities have also been convolved with a velocity uncertainty of 100 km s^{-1}, typical of that encountered in existing multi-object spectroscopic surveys such as the 2dFGRS (Colless et al. 2001). The dotted histogram shows the backsplash galaxies while the dashed histogram represents the in-falling galaxies (both normalised to the total number of satellites). The solid histogram is the sum of both distributions.

Not surprisingly, this figure appears quite different from Figure 6.8 due to the loss of information when transforming from 6-dimensional space to 3-dimensional space. The kinematically distinct bimodal populations are no longer readily separable. However, if the backsplash population does not exist, one should simply observe the dashed histogram in Figure 6.9. The presence of a backsplash population "distorts" the Gaussian velocity distribution function such that it increases with decreasing line-of-sight velocity.

Figure 6.9 should now be comparable to extant cluster data sets such as the 2dFGRS (Lewis et al. 2002). Lewis et al. show VDFs for 17 clusters (of order 50 galaxies per cluster). Stacking the 17 cluster VDFs, eliminating all galaxies within the (projected) virial radius, should yield a composite 1–2 R_{vir} VDF with $\sim 200-300$ galaxies; such a composite VDF should either support or refute our predicted result (Figure 6.9). However, this is just a first step to a fair comparison. The next step would require colour, surface brightness, kinematic selection and the inclusion of interloping galaxies that are false detections of cluster members.

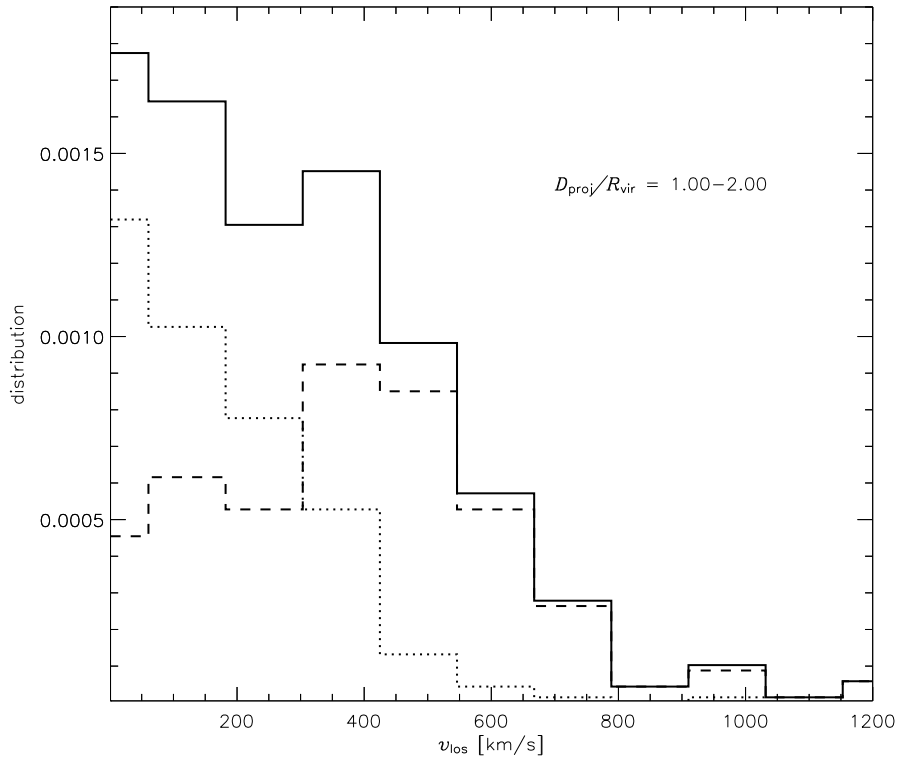

Figure 6.9: The distribution of the line-of-sight velocities

The distribution of the line-of-sight velocities (relative to the host) for galaxies with projected distance between 1.0–2.0 virial radii. Velocities have been convolved with the 2dF velocity uncertainty of 100 km s^{-1}, typical of that encountered in multi-object spectroscopic surveys (e.g. Colless et al. 2001). The dotted histogram represents the backsplash galaxies while the dashed histogram is based upon the in-falling galaxies (both normalized to the total number of satellites). The solid histogram is the sum of both distributions.

6.5 Conclusions

Observational data supports the idea that galaxies in clusters are substantially different from galaxies in the field. There is a clear correlation between galaxy morphology and density of the local environment. However, the origin of this relation is far from being understood.

In this study we have presented an analysis of satellite galaxies that once passed through the virial radius close to the centre of their respective host halo, but are now found outside the virial radius in the outskirts of the cluster. We have shown that this backsplash population is not negligible and needs to be accounted for when interpreting the various galaxy morphology relationships and decoupling the degeneracy between nature and nurture.

We must also appreciate that the in-falling population is not expected to be pristine. Rather, we would expect that in-fall galaxies have undergone some sort of pre-processing in groups before entering the cluster too as indicated by the sub-subhalos in Figure 6.2.

Our results can be summarized as follows:

- 30% of all galaxies that ever came closer to the host than its virial radius are now located in the range $[R_{\rm vir}, 2.5R_{\rm vir}]$,
- 50% of all galaxies in the region $[R_{\rm vir}, 2R_{\rm vir}]$ are backsplash galaxies,
- 90% of the backsplash galaxies penetrated deeper than 50% of $R_{\rm vir}$ into the host's potential,
- during their passage through the cluster, on average the backsplash galaxies lose 40% of their mass, thus
- the mass spectrum of the backsplash population has a steeper power-law slope than their in-falling counterparts, thus it has fewer massive galaxies and more light ones,
- the velocities of the in-falling satellites is too small to account for ram-pressure stripping in the cluster outskirts,
- the backsplash population has a factor of two smaller relative velocity than the in-falling satellites, making it kinematically distinct.

When transforming the last result into the observers plane though, the velocity separation between the in-falling and backsplash population is removed. However, the backsplash population should still be detectable as it is responsible for a continuous rise in the distribution function towards low line-of-sight velocities.

Our results suggest that we not only expect the backsplash population to experience various large-scale transformation mechanisms, but also small-scale ones, undergoing starvation, ram pressure stripping, tidally triggered star formation and significant tidal stripping.

Chapter 7

Mapping Substructure debri

"I have an existential map. It has You are here written all over it."

- Steven Wright

7.1 Introduction

With the discovery of stellar streams within the Milky Way (Helmi et al. 1999; Chiba & Beers 2000; Ibata et al. 2001c & 2002; Brook et al. 2003; Yanny et al. 2003; Navarro, Helmi & Freeman 2004; Majewski et al. 2004) and M31 (Ibata et al. 2001a; McConnachie et al. 2004) and streams and shells in clusters (Trentham & Mobasher 1998; Gregg & West 1998; Calcáneo-Roldán 2000; Feldmeier et al. 2002) they have become a standard fixture in our understanding of galaxy and cluster formation. These streams provide important observational support for the hierarchical build-up of galaxies and clusters and the Λ-dominated cold dark matter (ΛCDM) paradigm. Future observational experiments such as RAVE [1] and GAIA[2] are designed to shed further light on the importance of streams in galaxy formation. Thus to better interpret this observational data coming online in the near future it is necessary to have clear theoretical understanding of the stellar streams left behind by dissolving satellites (sub-halos).

The most common approach to this has been to simulate the disruption of individual satellite galaxies in *static* analytical potentials representative of the distribu-

[1] `http://astronomy.swin.edu.au/RAVE/`
[2] `http://astro.estec.esa.nl/GAIA/`

tion of dark matter (DM) halos (Kojima & Noguchi 1997; Helmi & de Zeeuw 2000; Harding et al. 2001; Ibata et al. 2002; Bekki et al. 2003; Majewski et al. 2004). Such simulations have provided great insight into the formation of stellar (Ibata et al. 2002) and gaseous (Yoshizawa & Noguchi 2003; Connors et al. 2004) streams, and helped to constrain the shape of the Milky Way's halo (Johnston et al. 1999; Ibata et al. 2001b) and substructure content (Johnston et al. 2002).

As we have seen though in the Introduction the ΛCDM structure formation scenario predicts that small objects form first and subsequently merge to form entities thus DM halos are never "at rest" but always be in the process of accreting material from its vicinity and hence grow in mass. This also extends to the Milky Way, although it encountered its last major merger some 10 Gyrs ago (Gilmore, Wyse & Norris 2003). Therefore, the question presents itself, *is a static analytical DM potential a valid assumption for a study of the disruption of satellites?*

While Zhao et al. (1999) already addressed the issue of the evolution of a satellite galaxy in a time-varying *analytical* potential, in this chapter we complement this study by comparing the disruption processes of satellite galaxies in a series of analytical potentials of growing complexity *and* fully self-consistent cosmological simulations. The brief outline of the chapter is as follows. We first discuss the simulation set up of the various host halo and satellite galaxy systems in Section 7.2. We then investigate the disrupted satellite first in real space in Section 7.3 then in integral space in Section 7.4. Finally we make our conclusions in Section 7.5.

7.2 The host halo and satellite galaxy

This study focuses on halo #1 from the series of high-resolution N-body galaxy clusters simulations as described in Chapter 2. Halo #1 was chosen because it is the oldest of the simulated clusters (i.e. 8.3 Gyrs) having a reasonably quiet merger history.

From this simulation we chose one particular satellite galaxy orbiting within the live host halo and refer to its evolution as the "live model". This choice was based upon two constraints: firstly, the satellite contains a sufficient number of particles and secondly, it has had multiple orbits. The satellite used throughout this study complies with these criteria in a way that it consists of $\sim$ 15,000 particles (as opposed to $\sim$ 800,000 for the host) at the "initial" redshift $z = 1.16$ (8.3 Gyrs ago) and has

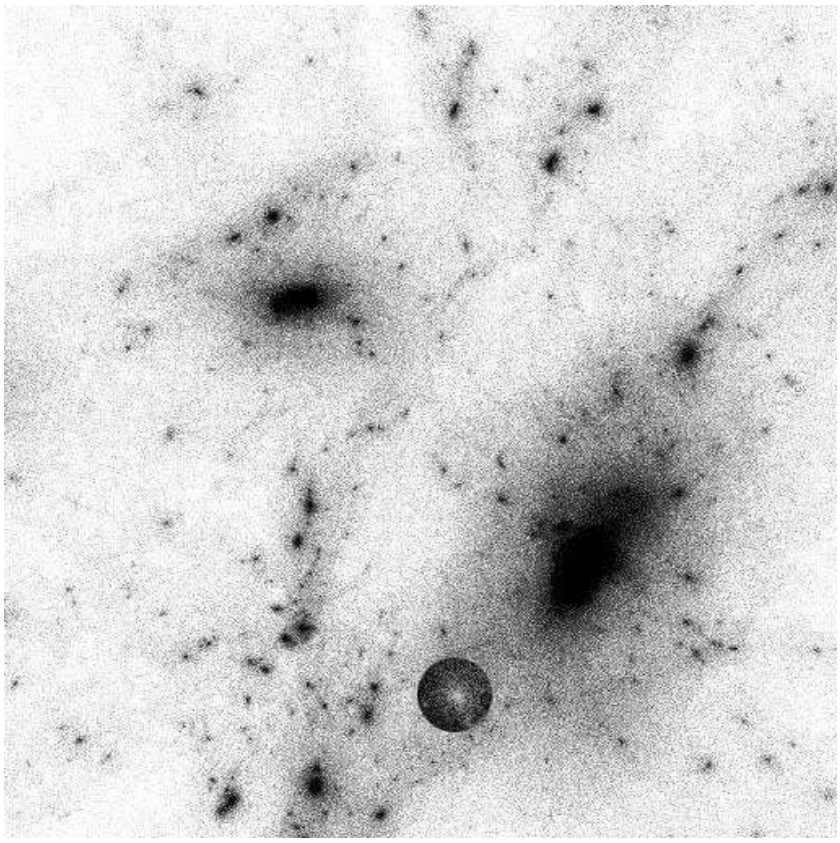

Figure 7.1: The satellite galaxy at $z = 1.16$
This figure shows the line-of-sight projected density for the host halo and the satellite galaxy at $z = 1.16$. Note that the satellite galaxies colour has been inverted make it easy to see. This satellite galaxy is falling into the host halo for the first time.

roughly 4 orbits within the host's virial radius until $z = 0$ when the mass of the host reached $2.8 \times 10^{14} h^{-1}$ $M_{\odot}$ (roughly 1,550,000 particles). This satellite is highlighted in Figure 7.1 at $z = 1.16$. At this redshift the satellite galaxy is falling in for the first time along one of the filamentary structures feeding the host.

After extracting the satellite from the cosmological simulation we used a tree N-body code (GCD+: Kawata & Gibson 2003) to model its evolution for 8.3 Gyrs in two (external) analytical potentials. The first of these two models we call the "evolutionary model" which uses an analytical reconstruction of the live halo's potential as follows: at each available snapshot of the live model, we fitted the host's DM density profile to the functional form of a (spherical) Navarro, Frenk & White

profile (Navarro, Frenk & White 1997, NFW)

$$\frac{\rho(r)}{\rho_b} = \frac{\delta_s}{(r/r_s)(1+r/r_s)^2} \ , \tag{7.1}$$

where ρ_b measures the cosmological background density, δ_s controls the amplitude and r_s measures the radius where the profile turns from its logarithmic slope of $d\log\rho/d\log r = -1$ to $d\log\rho/d\log r = -3$. From this series of snapshot NFW profiles we reconstruct the evolution of the parameters $\delta_s(z)$ and $r_s(z)$. Our best fitting functions are given below:

$$\begin{aligned} \delta_s &= \frac{23456}{(z+0.08)^{0.28}} - 1015 \ , \\ r_s &= 167.28 - 58.14 \ z^{1.2} \ . \end{aligned} \tag{7.2}$$

The mass growth can be calculated from $\delta_s(z)$ and $r_s(z)$ as follows

$$M(<r) = 4\pi\rho_b\delta_s r_s^3 \left(\ln\left(1+\frac{r}{r_s}\right) - \frac{r}{r+r_s} \right) \ . \tag{7.3}$$

Figure 7.2 shows the evolution of r_s, δ_s and consequentially mass as a function of redshift for both the numerical simulation alongside the analytical formula described by Eq. (7.2). The increase of the host's mass around $z = 0.45$ is related to a transient ("backsplash") satellite galaxy passing just within the virial radius at high velocity (cf. Chapter 3). The second model assumes a static analytical host potential and hence is labelled "fixed model". The parameters $\delta_s = 21070$ and $r_s = 97.8$ adopted for the fixed model agree with the initial values for the evolutionary model.

The analytical potential for a NFW density distribution that was used in the simulations can be derived by solving Poisson's equation and reads as follows (cf. Lokas & Mamon 2001).

$$\Phi_{\rm NFW}(r) = -4\pi G\rho_b\delta_s r_s^3 \frac{\ln\left(1+r/R_{\rm vir}\right)}{r} \ . \tag{7.4}$$

All three models are summarized in Table 7.1. Note that in both analytical models the hosts are assumed to be spherical. Dynamical friction is not implemented, either.

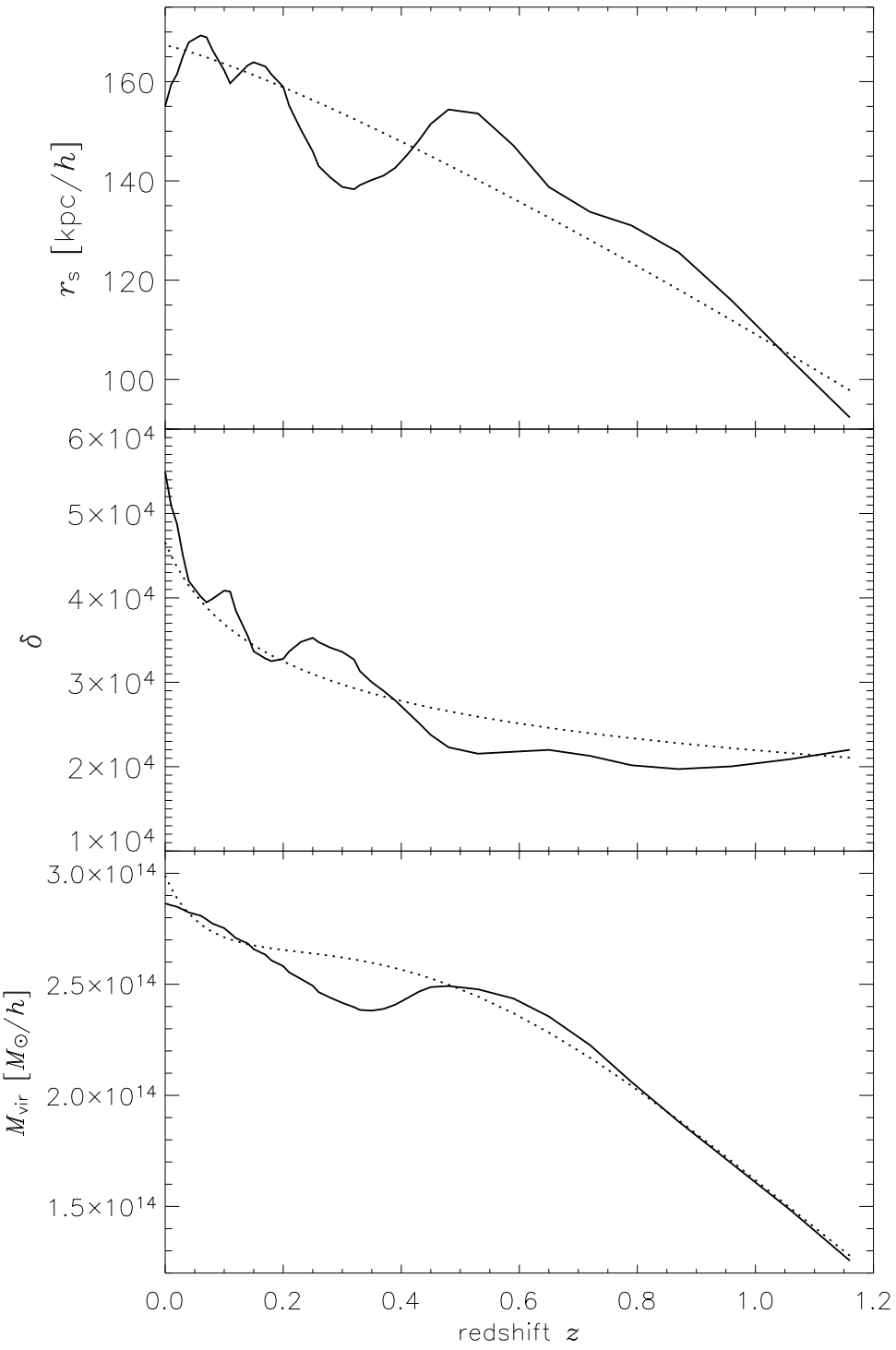

Figure 7.2: The evolution of the Host Halo

The redshift dependence for r_s (upper panel), δ_s (middle panel) and consequentially virial mass, $M_{\rm vir}$ (lower panel). The solid lines indicate the evolution in the live model, and the dashed lines are our best fitting formula to describe the evolution (see eq. 7.2).

Table 7.1: Summary and nomenclature for the four models. The disruption times and number of full orbits are for the modelled satellite galaxy.

Model	δ_s	r_s $[h^{-1}$ kpc]
live	solid lines in Figure 7.2	
evolutionary	as given by Eq. (7.2)	
fixed	21070	97.8

7.3 Real-Space Properties

In Figure 7.3 we show the real-space distribution of the disrupted satellite after the 8.3 Gyrs evolution, i.e. at $z = 0$. Figure 7.4 shows the distance of the satellite galaxy to the host as a function of time. The spread in the number of orbits amongst the models can readily ascribed to the difference in host mass and the small "mis-modelling" of its growth as seen in Figure 7.2 at around redshift $z = 0.3$.

These figures further highlight a number of interesting differences and similarities amongst the models. The most striking feature is that neither of the analytical models is capable of producing the real-space distribution of particles seen in the live model, and the live model shows the most "compact" distribution. Although all models display "shell"-like features, they are less eminent for the live host. Instead, the live model exhibits a "cross-like" feature and appears to be more compact in the central region, respectively. A comparable feature, in fact, has also been noted in observational streams (cf. Hau et al. 2005).

7.4 Integral-Space Properties

Helmi & de Zeeuw (2000) outlined a method for identifying stellar streams within observational data sets by utilising conservation of energy, E, and angular momentum, L, (i.e. the integrals-of-motion) for spherically symmetric and time-independent potentials. In fact, this method proved to be a powerful tool for identifying streams in the Milky Way using the proper motions of solar neighbour stars (Helmi et al. 1999; Chiba & Beers 2000; Brook et al. 2003; Navarro, Helmi & Freeman 2004). We expand their analysis not only limiting ourselves to static analytical models but extending the study to include both our live and evolutionary models.

The integrals of motion, total energy $E_i = T_i + U_i$ and angular momentum $\vec{L}_i$ for

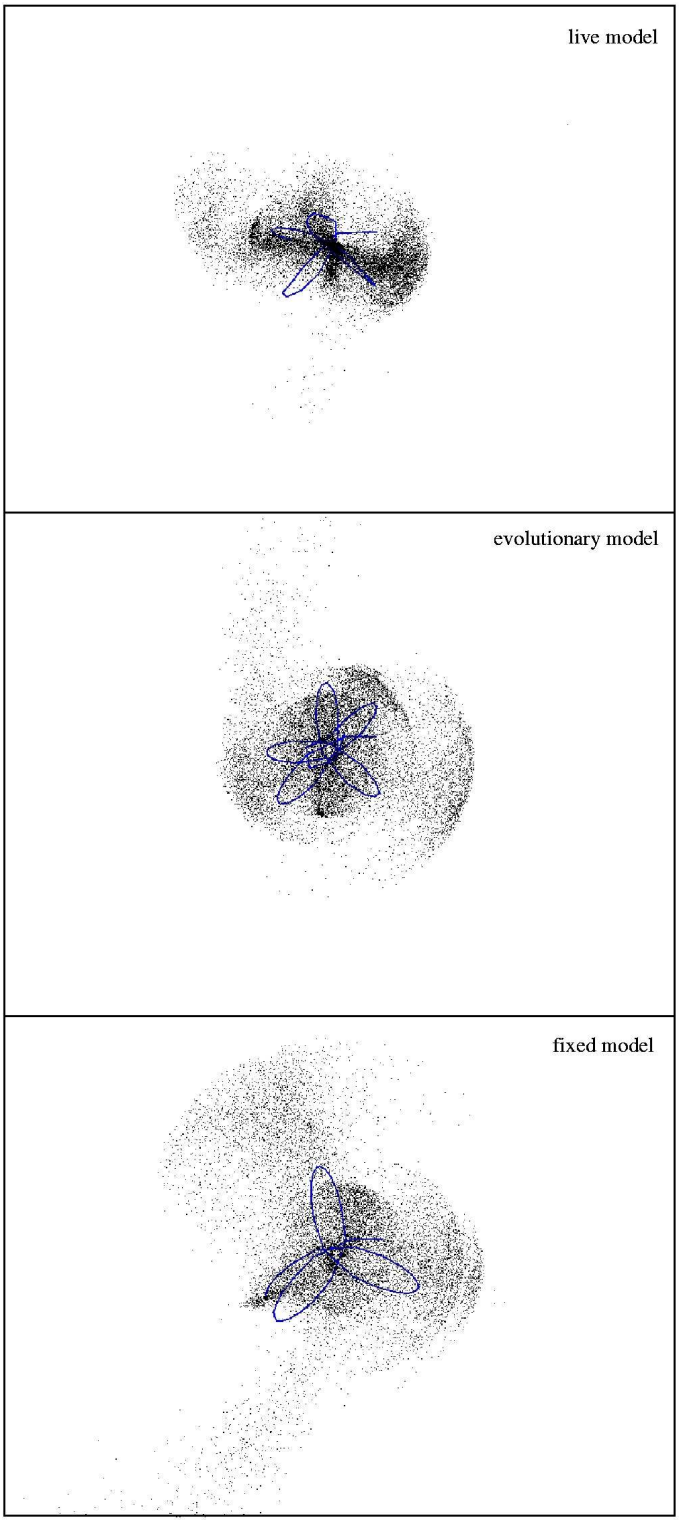

Figure 7.3: The disrupted satellite for all the models

The projected particle distribution of the disrupted satellite for all the models at $z = 0$. The lines indicate the orbital paths of the satellite of the respective model.

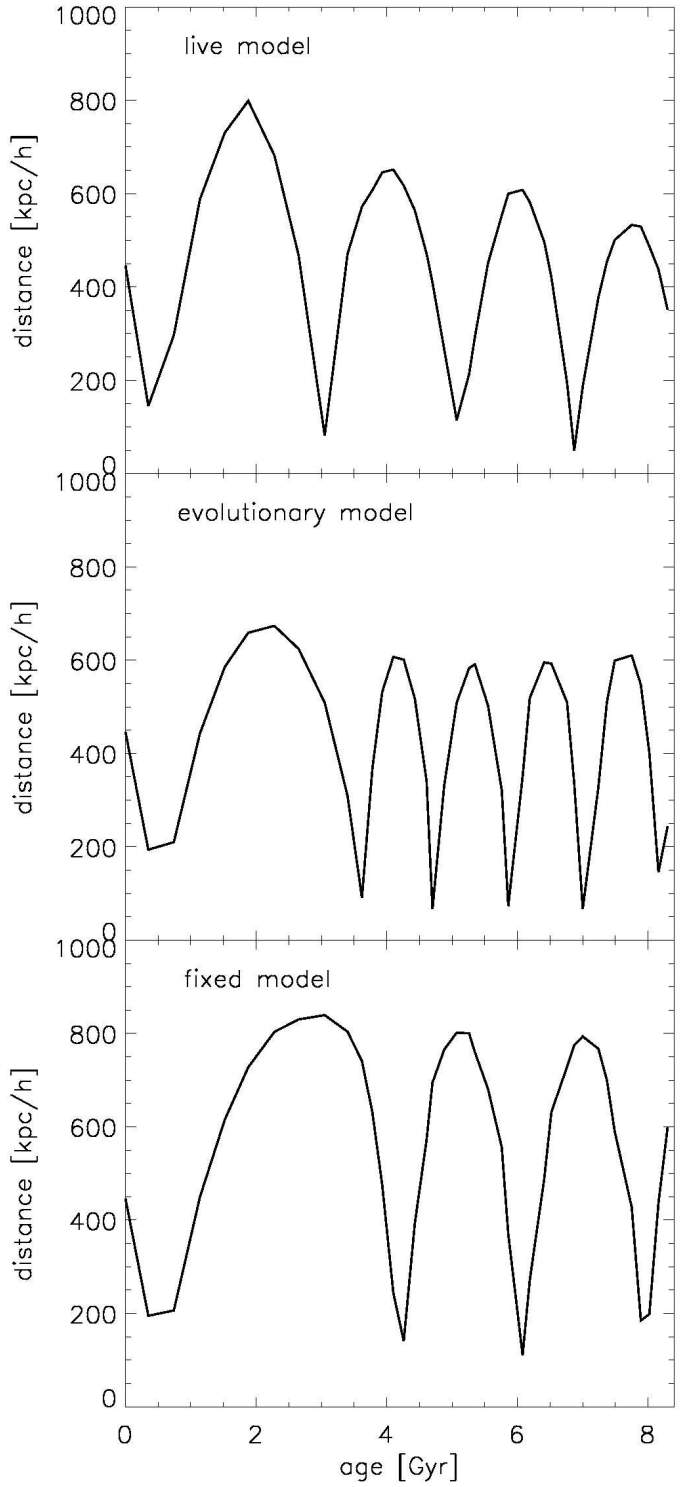

Figure 7.4: The orbit of the satellite galaxy.
The distance of the satellite galaxy to the host as a function of time.

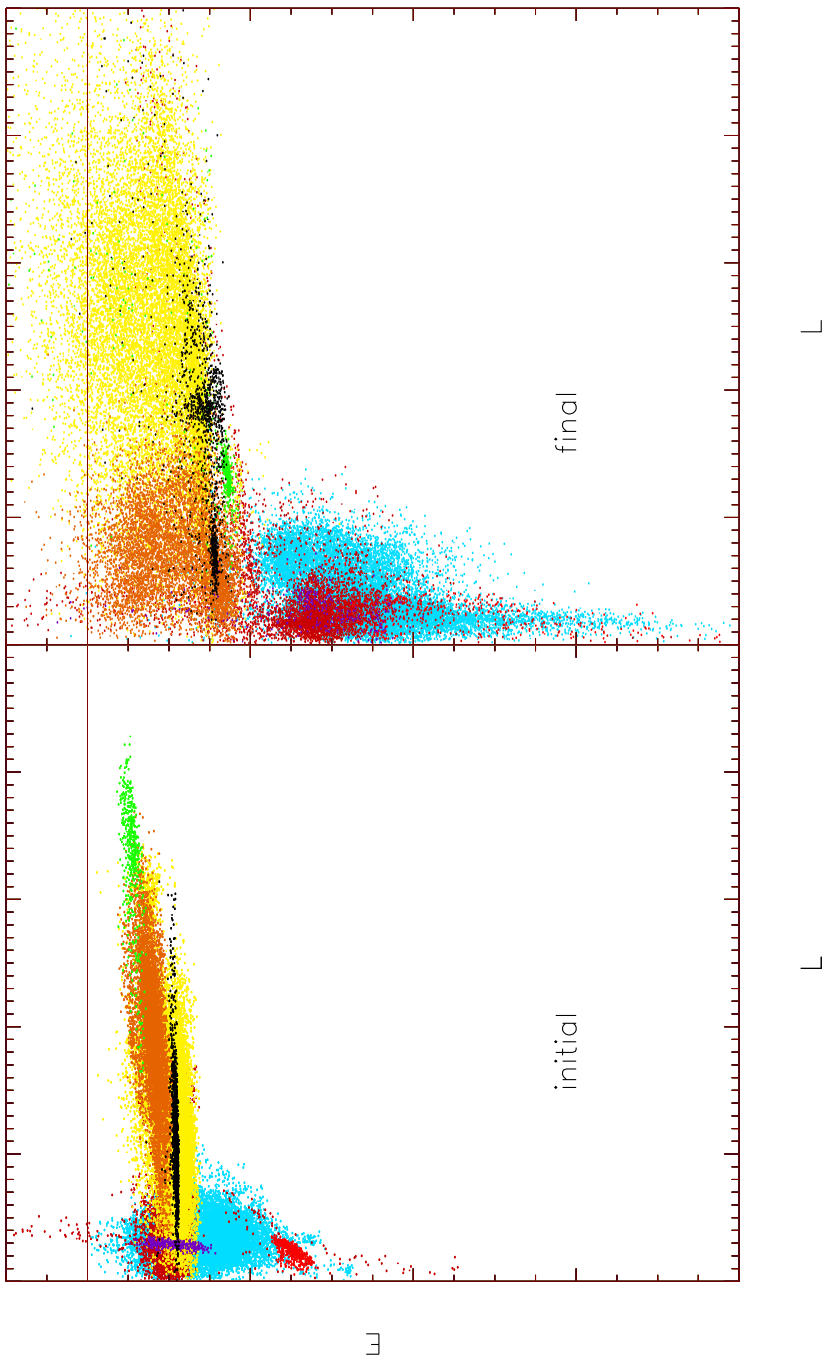

Figure 7.5: Distributed satellites in integral space for the live model
The distribution of satellite particles in the $E - L$ plane for the live model. The bottom panel shows the distributions at the time the respective satellite galaxy enters the virial radius of the host whereas the top panel presents the distributions at $z = 0$. Different colours represent particles of different satellites.

each satellite particle i with respect to the host halo is calculated as follows. For the two analytical NFW potential models, we simply use Eq. (7.4) as the contribution from the host to the potential energy U_i, but for the live model we adhere to the following:

$$\Phi_{\rm live}(r) = -G\left(\frac{M(<r)}{r} + \frac{M_{\rm vir}}{R_{\rm vir}}\frac{gc}{1+r/r_s}\right) , \tag{7.5}$$

where $g = [\log(1+c) - c/(1+c)]^{-1}$ and $c = R_{\rm vir}/r_s$ measures the concentration. This formula is also based upon the assumption that the halo is spherically symmetric but provides a reasonable approximation. The potential energy contribution from the host therefore reads

$$U_i^{\rm host} = m_i \begin{cases} \Phi_{\rm live}(r_i), & \text{for the live model} \\ \Phi_{\rm NFW}(r_i), & \text{for all other models} \end{cases} \tag{7.6}$$

This potential energy, however, is further augmented by the contribution from the self-gravity of the satellite which is derived via straight forward summation $U_I^{\rm sat}$. Thus the total potential energy of a single satellite particle is given by $U_i = U_i^{\rm host} + U_I^{\rm sat}$. The kinetic energy and angular momentum are calculated in the obvious way with respect to the host.

We like to stress that integrals of motion are associated with symmetries and cyclic coordinates in the Hamiltonian, respectively. For a static and spherically symmetric potential the Hamiltonian does not explicitly depend on time and the angles θ or ϕ which results in energy and angular momentum conservation. Yet this ideal situation is not even satisfied for the fixed model since the contribution from the self-gravity violates angular momentum conservation; we should observe energy conservation though. However, conservation of energy and/or angular momentum should not be taken for granted. If observed, it simply indicates that the self-gravity of the satellite (and the time evolution of the potential) makes an overall small contribution to the Hamiltonian.

7.4.1 The evolution in the $E - L$ plane for the live model

Before exploring the evolution in the $E - L$ plane (hereafter also called "integral-space") of our target satellite in all three models, we present the evolution for eight different satellites in the live model alone. The result can be viewed in Figure 7.5 where each satellite is represented by an individual colour with our target satellite

plotted as cyan. The satellites shown in Figure 7.5 are all taken from the self-consistent cosmological simulation and represent a fair sample of all 158 available satellites, i.e. their masses cover a range from $M \sim 5 \times 10^{10} h^{-1}\,\mathrm{M}_{\odot}$ to $M \sim 4 \times 10^{12} h^{-1}\,\mathrm{M}_{\odot}$ and they are on different orbits. The left panel of Figure 7.5 shows the distributions at the time the satellite enters the virial radius of the host, whereas the right panel displays the distributions at $z = 0$.

Figure 7.5 allows us to gauge the "drift" of satellites in integral-space. We note that, compared to Figure 4 of Helmi & de Zeeuw (2000), the integrals-of-motion are hardly conserved in the live model, neither for high or low mass streamers. The distributions rather show a large scatter, and have been significantly "re-shaped" over time. In addition, the mean values of E and L are also moved after the evolution. For instance, the "red" satellite drifts in time over to the initial position of the "cyan" satellite. Figure 7.5 further demonstrates that the drift of our target satellite (cyan dots) is comparable to the evolution of the other satellites, thus indicating that this target satellite is a "typical satellite" in that respect.

One encouraging result implied from Figure 7.5, however, is that even though the integrals-of-motion are changing over time, *satellites still appear coherent in the* $E - L$ *plane*. Hence, the integral-space analysis pioneered by Helmi & de Zeeuw (2000) still proves to be a useful diagnostic to identify streams. We further like to stress that observations only provide us with the snapshot of the distribution at today's time, i.e. the right hand panel of Figure 7.5 and hence measuring "evolution" is beyond the scope of RAVE and GAIA.

7.4.2 The evolution in the $E - L$ place for all models

Figure 7.6 now focuses on our target satellite alone, showing its particles at initial and final time in the $E - L$ plane for all three models, i.e. the live, evolutionary and fixed model. We notice that particles tend to form "stripes" in the $E - L$ plane (parallel to the L-axis) indicative of a spread in angular momentum for particles of comparable energy. These stripes form over time and have been directly linked to both apo- and peri-centre passages of the satellite. The live model deviates most prominently from the other models not only reducing total energies, but also "randomising" the angular momentum and hence lacking the prominence of these stripes. We also observe in Figure 7.6 that the fixed model is the only model to show a noticeable number of particles ($\approx 3\%$) *not* bound to the host halo, i.e. $E > 0$.

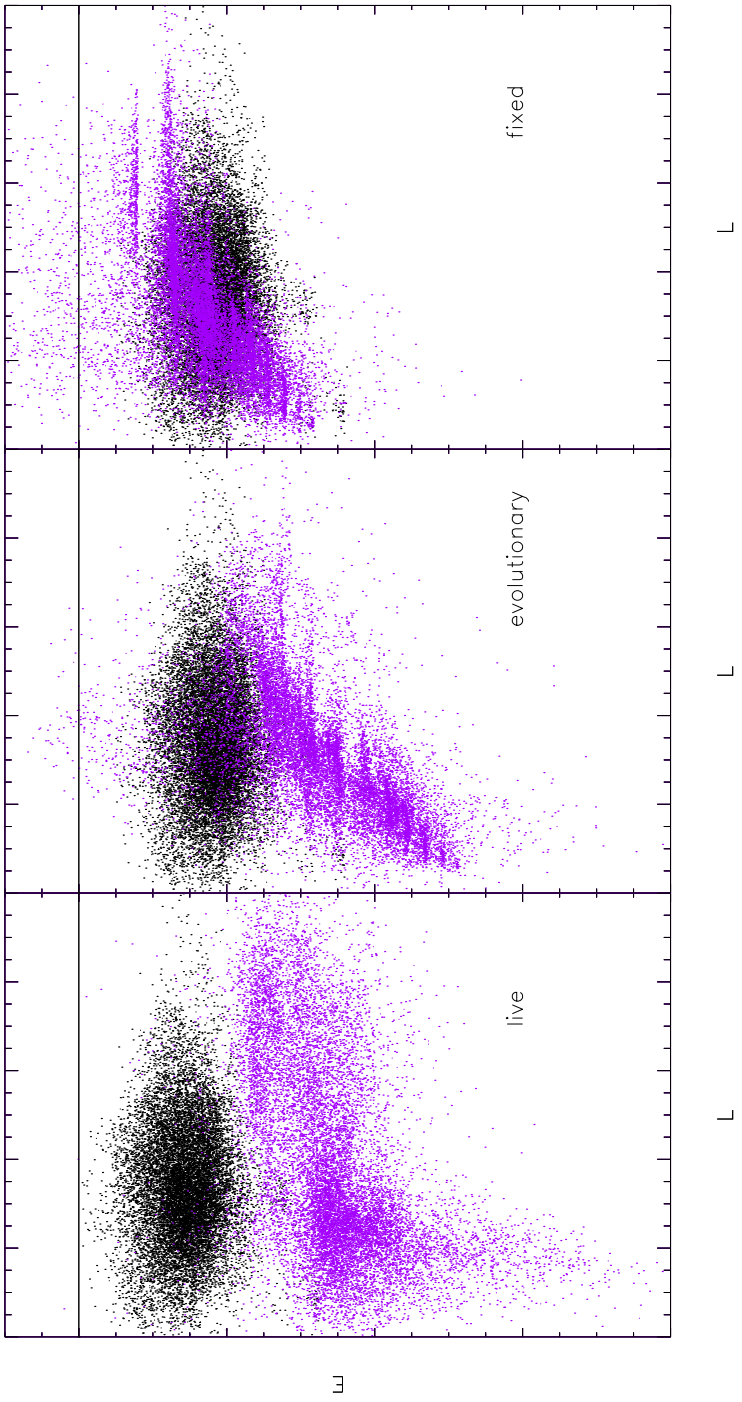

Figure 7.6: The evolution in the $E - L$ place for all models

Total energy, E, versus absolute value of the angular momentum, L, for all satellite particles within the target satellite at initial redshift $z = 1.16$ (black) and at $z = 0$ (purple) in the live (bottom), evolutionary (middle) and fixed (top) models. The horizontal line indicates $E = 0$.

This can be ascribed to the lower mass of the host halo.

Moreover, Figure 7.6 confirms the findings of Helmi & de Zeeuw (2000) that within a fixed host potential a satellite galaxies retains its identity in the $E - L$ plane and the integrals-of-motion hardly change, respectively. This statement is further strengthened by Figure 7.7 which presents the actual frequency distribution of E and L at the initial and final time.

Not surprisingly, the live model shows the largest deviations from the initial configuration (Figure 7.7). In the live model the distribution of E and L is broadened over time, and the peak of E systematically moves toward lower values, while the peak of L does not change dramatically for this particular satellite. This "drop" of E is also observed in the evolutionary model; it reflects the steady mass growth and related deepening of the host potential (cf. Figure 7.2). Since the drift in E is the most significant change, the evolutionary model displays a similar distribution to the live model in the $E - L$ plane at $z = 0$.

To further quantify the evolution of the satellite in integral-space, we calculate the centre and area of the particle distribution seen in Figure 7.6 as a function of time. The centre is defined to be the two dimensional arithmetic mean in E and L values, respectively. The area covered in the $E - L$ plane is computed using a regular 128^3 grid covering that plane from $L_{\min}$ to $L_{\max}$ and $E_{\min}$ to $E_{\max}$ in the respective model. Here, only cells containing more than three particles are taken into account. The evolution of both area and centre as a function of time since $z = 1.16$ is presented in Figure 7.8.

The top panel of Figure 7.8 (showing the change in area) demonstrates that all three halos loose coherence of the distribution in integral-space. This loss is most prominent for the live model and least for the fixed model. This phenomenon can also be seen in a comparison between Figure 4 of Helmi & de Zeeuw (2000) and the right panel of Figure 7.5. Therefore, we conclude that a fixed (and even an evolutionary) model significantly underestimates the scatter in the integral-space, and earlier predictions based on the simulation using a static (or time-varying) analytical description for the halo potential overestimate their efficiency of the detection ability of streams.

The bottom panel of Figure 7.8 (showing the drift of the distribution's centre in the $E - L$ plane with respects to its initial position) is yet another proof that the fixed model holds the best conservation of energy and angular momentum. The "live" nature of the host mass can be held responsible for not only the increased

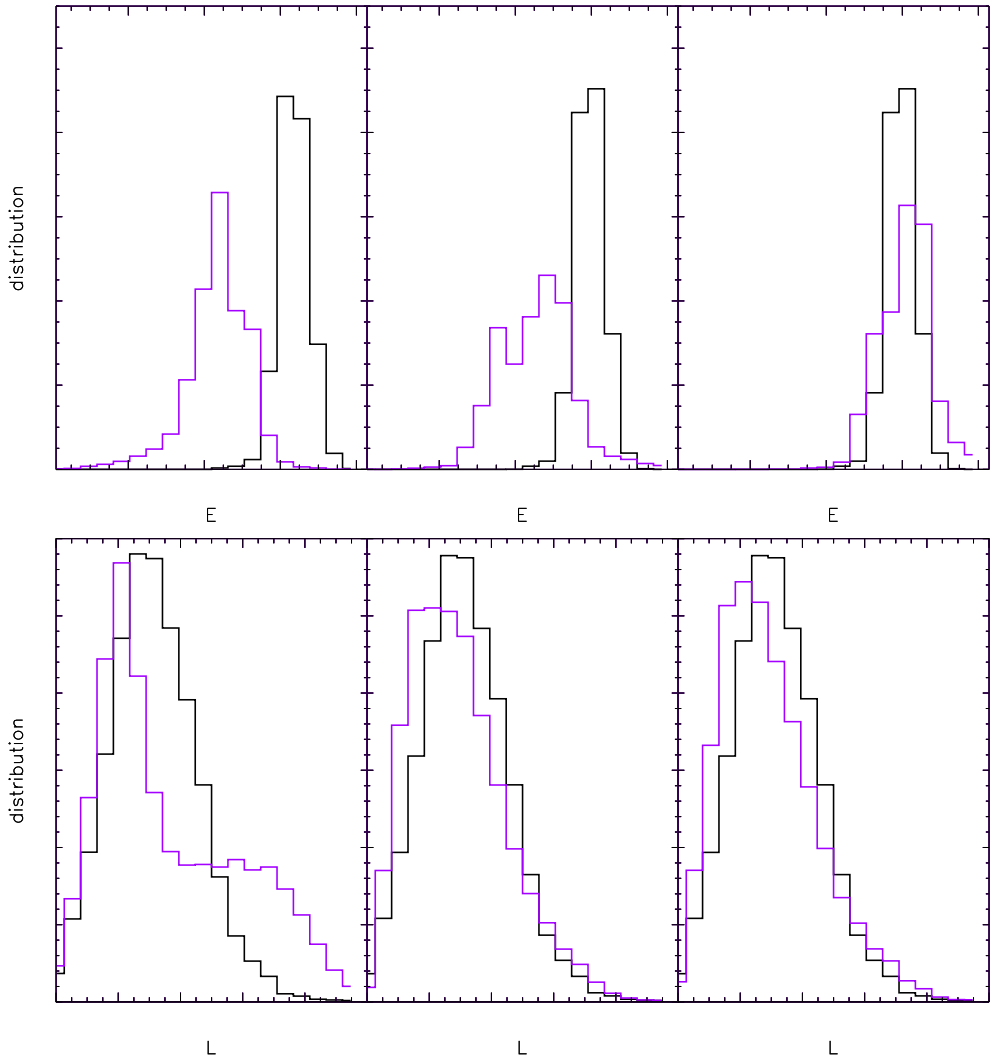

Figure 7.7: The change in energy and angular momentum distributions
The distribution of energies (upper panels) at initial (black) and final (purple) time and angular momentum (lower panels) for the three models (live, evolutionary, fixed, from left to right).

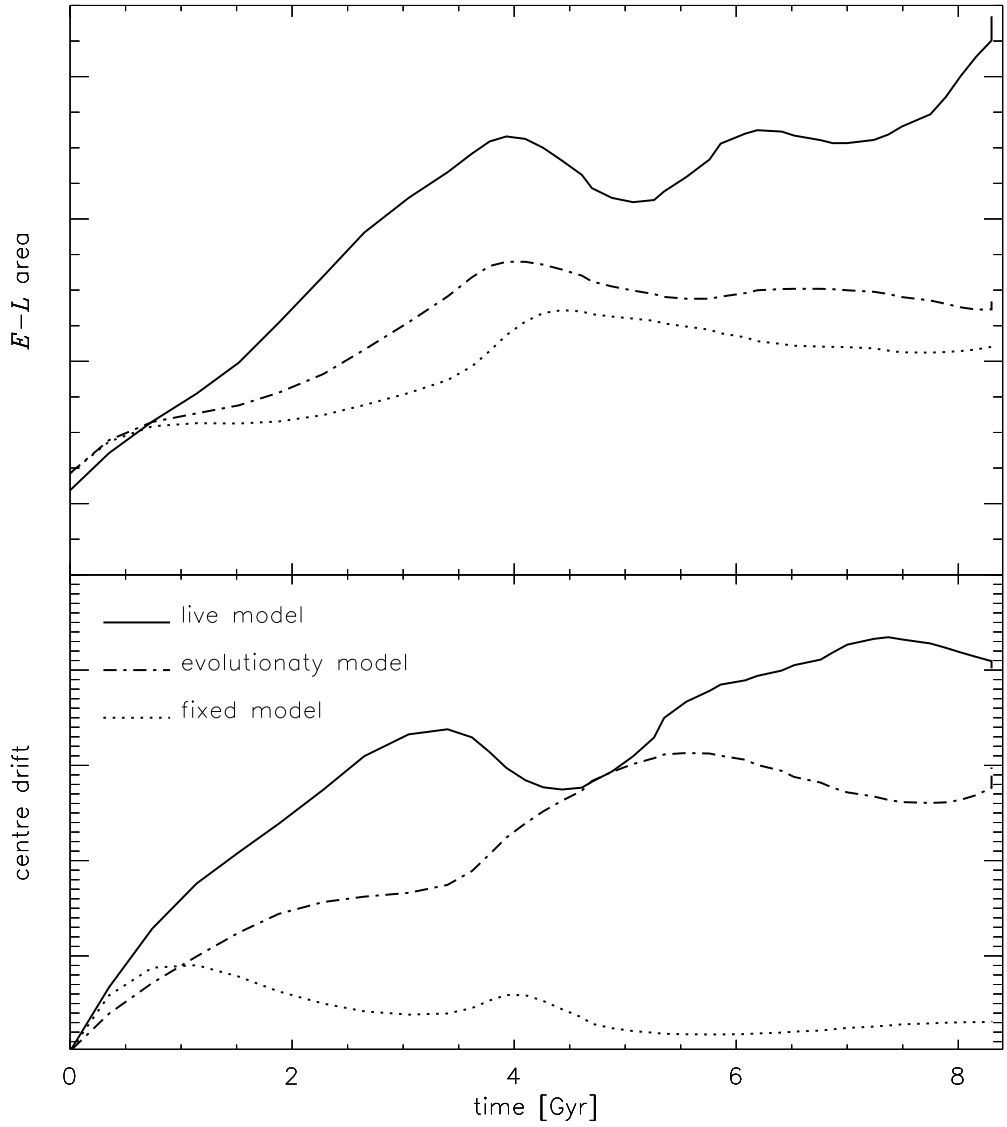

Figure 7.8: The time evolution of the disrupted satellite in integral-space
The evolution of the area (top panel) and the centre (bottom panel) in integral-space (see text for more details) as a function of time for the live (solid), evolutionary (dot-dashed) and fixed (dotted line) models.

dispersion (i.e. area) but also for the actual drift in integral-space. We further like to stress that at no time the evolutionary model matches the effects of the "live" model. There always appears to be a well pronounced discrepancy which can be ascribed to effects not considered in the evolutionary model, such as the triaxiality of the host and interactions of the debris with other substructure. This leads to the immediate conclusion that for an understanding of the formation of streams in integrals-of-motion space it appears rather crucial to take into account the full complex evolutionary effects of the host. The first such step has been taken by Zhao et al. (1999) who modelled the evolution of tidal debris in a time-varying potential. However, our study further indicates that in a "live" scenario there are additional effects at work leading to an even greater dispersion.

7.5 Conclusions

As we have seen in Chapter 1 in the hierarchical structure formation scenario Dark Matter halos continuously grow via both merger activity and steady accretion of material. Furthermore, they also contain a great deal of substructure and are far from spherical symmetry. We have investigated the development of streams due to the tidal disruption of satellite galaxies in a DM halo forming in a fully self-consistent cosmological simulation. This not only models the time-dependency of the potential (reflecting the mass growth of the host), it also accounts for other effects such as the triaxiality of the host and interactions of the debris with other satellites.

Our conclusions can be summarised as follows. (1) The distributions of (debris of) satellite galaxies in both real and integrals-of-motion space are sensitive to the evolution (and the particulars) of their host galaxy. This puts a caution on studies that investigate the shape of the halo based on satellite streams obtained via simulations with static DM halos. (2) Even in a ΛCDM "live" halo, satellites still appear to be coherent structures in the integrals-of-motion space. However, the coherency is smeared significantly in contrast to predictions from simulations using static and time-varying host potentials, respectively. Thus, earlier studies of the detection ability of streams using a static DM potentials (Helmi & de Zeeuw 2000; Harding et al. 2001) and even time-varying potentials (Zhao et al. 1999) could overestimate the efficiency of the "integrals-of-motion approach". (3) In the integrals-of-motion space, energy changes most significantly due to the mass growth of the host halo

which is inevitable in hierarchical structure formation scenarios. However, there are additional effects at work such as triaxiality of the host and interactions of the stream with other satellites. Hence, any currently observed distribution of a satellite stream in the $E - L$ plane no longer reflects its original distribution.

Chapter 8

Conclusions and Future Directions

"Between the traditional and the new, or between order and adventure, there is no real opposition; and what we call tradition today is a knit work of centuries of adventure."

- Jorge Luis Borges

8.1 Conclusion

Dark matter substructure is believed to be an integral component to galaxy and galaxy cluster formation and evolution. Throughout this thesis we have used numerical simulations to complete a number of studies that look at the evolution and fate of dark matter substructure.

Chapter 2: Simulations

`MLAPM` (Knebe, Green & Binney 2001) is an N-body solver that uses an adaptive multi grid approach to simulate the formation of structures in the Universe from collisionless dark matter. Taking advantage of `MLAPM`'s ability to efficiently and accurately simulate structure in dense environments through its adaptive grids, we produced a series of high-resolution ΛCDM cosmological simulations that focused on the formation and evolution of eight dark matter galaxy clusters, each of order a million particles within the virial radius. In addition to high mass and spatial resolution, we also have a substantial number of simulation snapshots and hence are

able to follow the evolution of the individual sub-halos as they fall into and orbit within the global potential of the cluster.

Chapter 3: Finding dark matter halos

To take advantage of data created by sophisticated N-body codes (such as MLAPM), one needs an equally sophisticated halo finder. In Chapter 3 we introduced our new "MLAPM-halo-finder" (MHF) which is based on the adaptive grid hierarchy of MLAPM.

In practice, the grid structure of MLAPM adaptively refines around high-density regions with an automated refinement algorithm. MLAPM creates a hierarchy of refinement meshes of differing resolutions closely following the complicated density distribution of simulation particles (i.e. filamentary structures, walls and, most importantly, gravitationally bound objects). The refinement is done cell-by-cell thus meshes are not constrained to have a rectangular (or any other) shape. Thus the grid structure naturally "surrounds" the dark matter halos, as they are simply manifestations of over-densities within (and exterior) to the underlying host halo.

Identifying isolated MLAPM grids we restructure the grid hierarchy into a "grid tree". Thus each of the branches of this tree is a 'dark matter halo'. Further, because of the unconstrained generation of the grids, each branch can have additional branches, thus identifying sub-sub-halos. This embedded-halo-within-halo scenario is limited only by the simulation resolution.

However, this method proved insufficient to find all sub-halos against the high background density in the innermost regions of the hosts. To overcome this obstacle we developed "MLAPM-halo-tracker" (MHT) which augmented the halo finder by incorporating information from multiple simulation timesteps. MHT allowed us to track the orbital evolution of gravitationally-bound objects through any given cosmological N-body-simulation.

Using both MHF and MHT we followed the temporal evolution of hundreds of individual satellites within their host halos. This excellent data set allowed us to perform the investigations described in Chapters 4-7.

Chapter 4: The dynamics of substructure

Our eight dark matter galaxy clusters (host halos) were chosen to sample a variety of formation histories, ages, and triaxialities. Despite their obvious differences, we have found striking similarities between their sub-halo populations.

Surprisingly, between each of the clusters the substructure populations of each host had an average eccentricity of ~ 0.6 and an average peaked pericentre of 35% of the cluster radius. We also found similar rates of sub-galaxy disruption for all galaxy clusters, which is not surprising considering the similarity in the orbital distributions. Specifically we found that the disrupted sub-galaxies were on more circular orbits, and thus that they experienced stronger tidal forces for longer periods.

Within our cluster simulations we also found that the velocity dispersion of the sub-galaxies was greater than the velocity dispersion of the actual galaxy cluster, implying that the sub-galaxies do not ideally reflect the underlying cluster. This result is significant because one popular method of measuring the mass of a cluster is based on the velocity dispersion of the sub-galaxies. However, our results found that this leads to an over-estimation of the cluster mass due to the mismatch in velocity dispersion. When we restricted the calculation of the sub-galaxy velocity dispersion to those sub-galaxies having more than one orbital period, this difference was essentially removed, and the sub-galaxies reflected the dynamics of the underlying cluster.

In summary, we found that all the properties of the sub-galaxy populations appear to be independent of the galaxy cluster and its history. We were unable to identify any trends with richness, triaxiality and/or formation time (other than the number of orbits) thus exhibiting a high level of self-similarity between the sub-galaxy populations.

Chapter 5: Anisotropy of substructure orbits

There is strong observational evidence on scales spanning from galaxy clusters down to galaxies there is a signal indicating a correlation between the alignment of substructure and the shape of the gravitational potential this substructure moves in. Using our cluster simulations we proposed a possible explanation for the controversy regarding the alignment of sub-halos orbits within dark matter halos.

Specifically we found that the apocentres of the orbits of these satellites lie preferentially within a cone of opening angle $\sim 40^\circ$ around the major axis of the host halo, in accordance with the observed anisotropy found in galaxy clusters. We do, however, note that a link to the dynamical age of the cluster is not well established as both our oldest dark matter halos show a clear anisotropy signal. Further analysis connects this distribution to the infall pattern of satellites along the filaments: the

orbits are determined by the environment of the host halo rather than by some "dynamical selection" during their life within the host's virial radius.

Chapter 6: Outskirts of dark matter halos

In addition to investigating the dynamics of sub-galaxies *within* the galaxy cluster, we also investigated galaxy populations in the outskirts of galaxy clusters.

It has been known for quite some time that galaxy properties in clusters are substantially different from galaxies in the field. However, the origin of the so-called 'morphology-density' relationships are still not fully understood, with several large and small-scale mechanisms proposed to explain their existence, including ram pressure stripping, tidal stripping/star formation, starvation, galaxy mergers and harassment and dynamics.

Using our simulations we demonstrated that a rich population of galaxies exists beyond the virial radius that at one stage had spent time near the cluster centre (i.e. "backsplash" galaxies). Hence, this needs to be appreciated when interpreting the various galaxy morphology environmental relationships and decoupling the degeneracy between nature and nurture. Specifically, we have found that approximately half of the galaxies with current cluster-centric distances in the range $1 - 2$ virial radii of the host were "backsplash" and that 90% of these had penetrated to within 50% of the virial radius. As a result they had undergone significant tidal disruption, losing on average 40% of their mass. Furthermore, we believe that these backsplash galaxies are kinematically distinct and should be observable within existing spectroscopic surveys.

Chapter 7: Mapping substructure debris

As we have seen in the introduction and Chapter 2, within the hierarchical structure formation paradigm galaxies/clusters are built by the continuous accretion of smaller objects. The disruption of these smaller galaxies within the (newly formed) larger halos results in the creation of stellar streams, the most spectacular of these in the Milky Way being the Sagittarius stream (Ibata 2001c).

Through this study we presented a detailed study of the real and integrals-of-motion space distributions of a disrupting satellite obtained from one of our fully self-consistent high-resolution cosmological simulation of a galaxy cluster. In addition, the satellite was re-simulated using various analytical halo potentials. We found

that its debris appears as a coherent structure in integrals-of-motion space in all models ("live" and analytical potential) although the distribution is significantly smeared for the live host halo. The primary mechanism for the dispersion is the mass growth of the host. However, when quantitatively comparing the effects of "live" and time-varying host potentials we conclude that not all of the dispersion can be accounted for by the steady growth of the host's mass. We ascribe the remaining discrepancies to additional effects in the "live" halo such as non-sphericity of the host and interactions with other satellites, which have not been modelled analytically.

8.2 Future Directions

Galaxy clusters are well-defined astrophysical objects that can be readily observed. However, there still remain numerous outstanding questions regarding their origins and properties. Currently, and in the future, I am interested in investigating (through numerical simulations) a number of important questions regarding the evolution of substructure and their tidal debris. A sample of these ongoing and planned investigations include:

Satellite-Satellite interaction

There are many mechanisms to transform a galaxy. Over the past decade there has been a great deal of work that aimed to quantify the effects of various transformation mechanisms, for example, the ram-pressure stripping of a galaxy's reservoir of gas by the hot intracluster medium. However, other mechanisms, such as sub-halo – sub-halo interactions or "galaxy harassment", have been paid comparatively little attention and thus their role in galaxy transformation within clusters is unclear. Are sub-halo – sub-halo interactions significant and are they sufficient to induce starbursts, thus exhausting the galaxies' reservoirs of gas that fuel their star formation? This is an outstanding question that we are ideally placed to investigate (through `MHT` and simulation data) and to which we can make a timely contribution.

Calculating the shape of the galactic potential using satellite streams

Another direction for future research that follows from my thesis (cf. Chapter 7) and has timely international recognition largely due to the European Space Agency's satellite mission GAIA and the ground based RAVE survey, is the investigation of

stellar streams from disrupting galaxies. As we have previously discussed the signatures of hierarchical galaxy formation are evident in the observed substructure seen in various phase-space projections of the Galactic halo. Ibata et al. (2001b) using the Sagittarius stream demonstrated their use in constraining the shape of the halo's gravitational potential. In the case of the Milky Way, Ibata et al. concluded that our halo was necessarily spherical (under the assumption of a static axisymmetric potential).

However, the current model of the Universe predicts that typical galaxy halos should be triaxial (Power et al. 2002). Thus, the observation that the Milky Way's halo is approximately spherical is difficult to reconcile with our current understanding. It would be interesting to extend the work in Chapter 7 on the identification of stellar streams and investigate the variance of a stream's coherence with its host halo, particularly focusing on effects of the stream in triaxial hosts. As a natural extension, we would address the question of what shape would be inferred for a cosmological halo by tracking the stellar debris, and how would it compare with the 'true' (or measured) shape?

Modelling galaxy clusters

Thus far we have studied in detail the gravitational dynamics of galaxy clusters. However, if we wish to better understand galaxy transformation in clusters, it is imperative that we relate our numerical models to the observational data. One potentially powerful way to achieve this is through the inclusion of baryonic physics in the cosmological (dark matter) simulations. There are a number of different ways to do this.

In the short term we aim to produce a modularised open source semi-numerical code. Unlike semi-analytic simulations that describe halo mass growth through analytical calculations based upon linear perturbation theory (Press & Schechter 1974), semi-numerical simulations use the dynamical information from N-body simulations. Both methods, however describe the baryonic physics through an analytic formalism. This method has many advantages, the first and foremost being that it is computationally inexpensive. This provides a user with a controlled way to investigate their research problem and explore a larger range in parameter space.

An example of the benefits of a semi-numeric approach is demonstrated in the interpretation of the anti-bias found in the sub-halo density profile, an anti-bias

that does not exist in observational data (cf. Chapter 4). Through the use of semi-numerical techniques Gao et al. (2004) were able to account for this discrepancy. Their conclusion was that tidal stripping of the dark sub-halos was very efficient in reducing their mass while having less of an effect on the tightly bound baryonic galaxy at its core. Thus, while the dark matter sub-halos in the inner regions of the cluster were being disrupted, their baryonic galaxies survived. (Note: such disrupted galaxies must be old).

Thus one natural extension of my research would be to build on the development of `MHF` and in particular `MHT` (tracker), which follows the galaxy dynamics and coupling it to a semi-analytical treatment, thus developing a semi-numerical code. Such a union would produce a powerful tool, which could be used to address questions regarding galaxy transformation, and to investigate broader questions such as the nature of various galaxy morphology relationships. For example, supplementing the kinematic information from the N-body simulations by producing colour and surface brightness distributions, thus assiting in the empirical identification of backsplash galaxies.

While these semi-numerical techniques are powerful, in the long run it is our aim to add hydrodynamics and baryonic physics into `MLAPM`. Although this problem is more computationally expensive and is more technically challenging, the gains from an ''unbiased" transformation into the observer's plane are significant.

With respects to modelling galaxy clusters, ultimately it is our aim to grow a suite of open source programmes that investigate cluster and galaxy evolution that are easy to use and take great care in transforming simulation data in to the observers plane.

"A humble peasant who serves God is much more pleasing to him than an arrogant academic who neglects his soul to consider the course of the stars"

- Thomas á Kempis

"When the Sun shrinks to a dull red dwarf, it will not be dying. It will just be starting to live and everything that has gone before will merely be a prelude to its real history."

- Arthur C. Clarke

Bibliography

[1] Aarseth S.J., MNRAS **126**, 223 (1963)

[2] Aguerri J.A.L., Iglesias-Paramo J., Vilchez J.M., Munoz-Tunon C., ApJ **127**, 1344 (2004)

[3] Arp H., PASP, **80**, 129, (1968)

[4] Bahvsar S., ApJ **246**, L5 (1981)

[5] Bailin J., Steinmetz M., Astron. J. **27**, 616 (2004)

[6] Balogh M.L., Navarro J.F., Morris S.L., ApJ **540**, 113 (2000)

[7] Barnes J.E., Hut P., Nature **324**, 446 (1986)

[8] Bekki K., Couch W.J., Drinkwater M.J., Shioya Y., MNRAS **344**, 399 (2003)

[9] Bertschinger E., Gelb J.M., Computers in Physics **5**, 164 (1991)

[10] Bingegeli B., Tammann G.A., Sandage A., Astron. J. **94**, 251 (1987)

[11] Bingelli B. 1999, in The Radio Galaxy Messier 87, ed. H.J. Roser & K. Meisenheimer (Berlin: Springer), 9

[12] Binney J., Tremaine S., *Galactic Dynamics*, Princeton: Princeton University Press, (1987)

[13] Bode P., Ostriker J.P., Turok N., ApJ **539**, 93 (2001)

[14] Bullock J., Kravtsov A., Weinberg D., ApJ **539**, 517 (2000)

[15] Bullock J., Kolatt T.S., Sigad Y., Sommervile R.S., Kravtsov A.V., Klypin A.A., Primack J.R., Dekel A., MNRAS **559**, 321 (2001)

[16] Brainerd T.G., astro-ph/0408559

[17] Brandt A., Math. Comput., **31**, 333, (1977)

[18] Brook C.B., Kawata D., Gibson B.K., Flynn C., ApJ **585**, L125 (2003)

[19] Bryan G.L., Norman M.L., ApJ **495**, 80 (1998)

[20] Butcher H., Oemler A., ApJ **226**, 559 (1978)

[21] Calcáneo-Roldán C., Moore B., Bland-Hawthorn J., Malin D., Sadler E.M. MNRAS **314**, 324 (2000)

[22] Carlberg R. G., ApJ **433**, 368 (1994)

[23] ChaboyerB., DemarqueP., KernanP.J., KraussL.M., ApJ **494**, 96 (1998)

[24] Chiba M., Beers T.C., Astron. J. **118**, 2843 (2000)

[25] Colberg J.M., White S.D.M., Jenkins A., Pearce F.R., MNRAS **593**, 308 (1999)

[26] Cole S., Lacey C., MNRAS **281**, 716 (1996)

[27] Colin P., Avila-Reese V., Valenzuela O., ApJ **542**, 662 (2000)

[28] Colin P., Klypin A., Kravtsov A., Khokhlov A., ApJ **523**, 32 (1999)

[29] Colless M., et al. VizieR On-line Data Catalog **226**, 7226, (2003)

[30] Colless M., et al. MNRAS **328**, 1039 (2001)

[31] Connors T.W., Kawata D., Maddison S.T., Gibson B.K., Pub. Astron. Soc. Aust. **D21**, 222 (2004)

[32] Dahle H., Hannestad S., Sommer-Larsen J., ApJ **588**, 25 (2003)

[33] Dalal N., Kochanek C. S., ApJ **572**, 25 (2002)

[34] Davis M., Efstathiou G., Frenk C.S., White S.D.M., ApJ **292**, 371 (1985)

[35] deBernardisP., et al. Nature **404**, 955 (2000)

[36] de Lucia G., Kauffmann G., Springel V., White S., astro-ph/0306205

[37] de Souza R.E., Capelato H.V., Arakaki L., Logullo C., ApJ **263**, 557 (1982)

[38] Dressler A., ApJ **236**, 351 (1980)

[39] Dubinski J., Carlberg R. G., ApJ **496**, 378 (1991)

[40] Efstathiou G., Davis M., Frenk C.S., White S.D.M., ApJ Suppl. **57**, 241 (1985)

[41] EkeV.R., Cole S., Frenk C.S., MNRAS **282**, 263 (1996)

[42] Evans N.W., Witt H.J., MNRAS **345**, 1351 (2003)

[43] Faltenbacher A., Gottlber S., Kerscher M., Mller V., A&A **359**, 1 (2002)

[44] Feldmeier J.J., Mihos C., Morrison H.L. Rodney S., Harding P., ApJ **575**, 779 (2002)

[45] Franx M., Illingworth G., de Zeeuw T., ApJ **383**, 112 (1991)

[46] Freeman K.C., 1996, in ASP Conf. Proc. 92, Formation of the Galactic Halo - Inside and Out, ed. H. Morrison & A. Sarajedini (San Francisco: ASP), p.3

[47] Frenk C.S., White S.D.M., Davis M., Efstathiou G., ApJ **327**, 507 (1988)

[48] Gardiner L.T., Noguchi M., MNRAS **278**, 191 (1996)

[49] GarnavichP.M., JhaS., ChallisP., ClocchiattiA., DiercksA., FilippenkoA.V., GillilandR.L., Astron. J. **509**, 74 (1998)

[50] Ghigna S., Moore B., Governato F., Lake G., Quinn T., Stadel J. MNRAS **300**, 146 (1998)

[51] Ghigna S., Moore B., Governato F., Lake G., Quinn T., Stadel J. MNRAS **544**, 616 (2000)

[52] GibsonB.K., StetsonP.B., FreedmanW.L., MouldJ.R., KennicuttR.C.Jr., HuchraJ.P., et al. ApJ **529**, 723 (2000)

[53] Gill S.P.D., Knebe A., Gibson B.K. MNRAS **351**, 399 (2004a)

[54] Gill S.P.D., Knebe A., Gibson B.K., Dopita M.A., MNRAS **351**, 410 (2004b)

[55] Gill S.P.D., Knebe A., Gibson B.K., IAU Colloquium #195 **280** (2004)

[56] Gill S.P.D., Knebe A., Gibson B.K., MNRAS **356**, 1327 (2005)

[57] Gilmore G., Wyse R.F.G., Norris J.E., ApJ Lett. **574**, 39 (2003)

[58] Gingold R.A., Monaghan J.J., MNRAS **181**, 375 (1977)

[59] Gleb J. M., Bertschinger E., ApJ **436**, 467 (1994)

[60] Goto T., Yamauchi C., Fujita Y., Okamura S., Sekiguchi M., Smail I., Bernardi M., Gomez P., MNRAS **346**, 601 (2003)

[61] Götz M., Huchra J. P., Branderberger R. H., `astro-ph/9811393`

[62] Grebel E.K., Kolatt T., Brandner W., 1999, in *The stellar content of the Local Group*, IAU 192, eds. P. Whitelock & R. Cannon, San Francisco: ASP Conf. Series

[63] Gregg M.D., West M.J. Nature **396**, 549 (1998)

[64] Groth J. E., Peebles P. J. E., ApJ **217**, 385 (1977)

[65] Gunn J.E., Gott R.J., ApJ **176**, 1 (1972)

[66] Harding P., Morrison, H.L., Olszewski E.W., Arabadjis J. Mateo M., Dohm-Palmer R.C., Freeman K.C., Norris J.E., ApJ **122**, 1397 (2001)

[67] Hartwick F.D.A. 1996, in Proc. IAU Symp. 169, Unresolved Problems of the Milky Way, ed. L. Blitz & P. Teuben (Dordrecht: Kluwer), 669

[68] Hashimoto Y., Funato Y., Makino J., ApJ **582**, 196 (2003)

[69] Hatton S., Ninin S., MNRAS **576**, 322 (2001)

[70] Hau G., Gill S.P.D., Knebe A., Gibson B.K., 2005 in preparation

[71] Hayashi E., Navarro J., Taylor J., Stadel J., Quinn T., ApJ **584**, 541 (2003)

[72] Heisler J., Tremaine S., Bahcall J., N., ApJ **298**, 8 (1985)

[73] Helmi A., White S.D.M., de Zeeuw P.T., Zhao, H., Nature **402**, 53 (1999)

[74] Helmi A., de Zeeuw P.T., MNRAS **319**, 657 (2000)

[75] Holmberg E., Ark. Astron., **5**, 305, (1969)

[76] Hubble E., Humason M.L., ApJ **74**, 43 (1931)

[77] Ibata R.A., Irwin M.J., Lewis G.F., Ferguson A.M.N., Tanvir N.R., Nature **412**, 49 (2001a)

[78] Ibata R., Lewis G.F., Irwin M., Totten E., Quinn T., ApJ **551**, 294 (2001b)

[79] Ibata R., Irwin,M., Lewis,G.F., Stolte,A., ApJ **547**, 133 (2001c)

[80] Ibata R.A., Lewis G.F., Irwin M.J., Cambrésy L., MNRAS **332**, 921 (2002)

[81] Icke V., A&A **144**, 115 (1985)

[82] Iodice E., Arnaboldi M., Bournaud F., Combes F., Sparke L. S., van Driel W., Capaccioli M., ApJ **585**, 730 (2003)

[83] Jing Y. P., Suto Y., ApJ **538**, 574 (2002)

[84] Johnston K.V., Zhao H., Spergel D.N., Hernquist L., ApJ Lett. **512**, 109 (1999)

[85] Johnston K., Hernquist L., Bolte M., ApJ **465**, 278 (1996)

[86] Katz N., Quinn T., Bertschinger E., Gelb J. M., MNRAS **270**, 71 (1994)

[87] Kawata D., Gibson B.K., MNRAS **340**, 908 (2003)

[88] Kenney J. D. P., van Gorkom J. H., Vollmer B., `astro-ph/0403103`, 2004, accepted for ApJ

[89] Kitzbichler M.G., Saurer W., ApJ Lett. **590**, 9 (2003)

[90] Klypin A.A., Shandarin, S. F., MNRAS **204**, 891 (1983)

[91] Klypin A.A., Holtzman J., `astro-ph/9712217`

[92] Klypin A. Gottlober S., Kravtsov A., Khoklov A., ApJ **516**, 530 (1999a)

[93] Klypin A., Kravtsov A., Valenzuela O., Prada, F., ApJ **522**, 82 (1999b)

[94] Kodama T., Bower R. G., MNRAS **321**, 18 (2001)

[95] Kojima M., Noguchi M., ApJ **481**, 132 (1997)

[96] Knebe A., Green A., Binney J., MNRAS **325**, 845 (2001)

[97] KnebeA., DevriendtJ.E.G., MahmoodA., SilkJ., MNRAS **329**, 813 (2002)

[98] Knebe A., Gill S.P.D., Gibson B.K., Lewis G.F., Ibata R.A., Dopita M.A., ApJ **347**, 7 (2004)

[99] Kravtsov A. V., Klypin A. A., Khokhlov A. M., ApJ Suppl. **111**, 73 (1997)

[100] Kravtsov A. V., PhD thesis, New Mexico State University, Las Cruces, (1999)

[101] Kravtsov A. V., Gnedin O. Y., Klypin A. A., ApJ submitted, `astro-ph/0401088`

[102] Kunkel W.E., Demers S., Roy. Green. Obs. Bull., **182**, 241, (1976)

[103] Lacey C., Cole S., MNRAS **271**, 676 (1994)

[104] Larson R. B., Tinsley B. M., Caldwell C. N., ApJ **237**, 692 (1980)

[105] Lee J., Kang X., `astro-ph/0505179`

[106] Lewis I., et al. MNRAS **334**, 673 (2002)

[107] Lokas L., Mamon A., MNRAS **321**, 155 (2001)

[108] Lucy L.B., Astron. J. **82**, 1013 (1977)

[109] Lynden-Bell D., Observatory, **102**, 202, (1982)

[110] Majewski S.R., Kunkel W.E., Law D.R., Patterson R.J. Polak A.A. et al., 2005 AJ in press (astro-ph/0403701)

[111] Majewski S.R., ApJ Lett. **431**, 17 (1994)

[112] Mamon G. A., Sanchis T., Salvador-Sole E., Solanes M. J., A&A **414**, 445 (2004)

[113] Matthewson D.S., Clearly M.N., Murray J.D., ApJ **190**, 291 (1974)

[114] McConnachie A., Irwin M., Lewis G., Ibata R., Chapman S., Ferguson A., Tanvir N., 2004 MNRAS in press (astro-ph/0406055)

[115] McGaughS.S., deBlokW.J.G., ApJ **499**, 41 (1998)

[116] Merritt D., ApJ **264**, 24 (1983)

[117] Merritt D., ApJ **276**, 26 (1984)

[118] Miyazaki S., et al. PASJ **54**, 833 (2002)

[119] Monaghan J.J., Ann. Rev. A & A **30**, 543 (1992)

[120] Moore B., Katz N., Lake G., Dressler A., Oemler A., Nature **379**, 613 (1996)

[121] Moore B., Katz N., Lake G., ApJ **457**, 455 (1996)

[122] Moore B., Ghigna S., Governato F., Lake G., Quinn T., Stadel J., Tozzi P., ApJ Lett. **524**, 19 (1999)

[123] Navarro J., Frenk C.S., White S.D.M., ApJ **462**, 563 (1996)

[124] Navarro J., Frenk C.S., White S.D.M., ApJ **490**, 493 (1997) (NFW)

[125] Navarro J.F., Helmi A., Freeman K.C., ApJ **601**, 43 (2004)

[126] Oemler A., ApJ **194**, 1 (1974)

[127] Okamoto T., Habe A., ApJ **516**, 591 (1999)

[128] Okamoto T., Nagashima M., ApJ **587**, 500 (2003)

[129] Olling R.P. Merrifield M.R., MNRAS **311**, 361 (2000)

[130] Onuora L.I., Thomas P.A., MNRAS **319**, 614 (2000)

[131] PeacockJ.A., et al. Nature **410**, 169 (2001)

[132] Peebles P. J. E., Astron. J. **75**, 13 (1970)

[133] Peñarubbia J., Kroupa P., Boily C., MNRAS **333**, 779 (2002)

[134] PenziasA.A., WilsonR.W., ApJ **142**, 419 (1965)

[135] Plionis M., Basilikos S., MNRAS Lett. **329**, 47 (2002)

[136] Postman M., Geller M.J., ApJ **281**, 95 (1984)

[137] Power C., Navarro J.F., Jenkins A., Frenk C.S, White S.D.M., Springel V., Stadel J., Quinn T., `astro-ph/0201544`

[138] Press W. H., Schechter P., ApJ **303**, 425 (1974)

[139] Press W.H., Teukolsky S.A., Vetterling W.T., Flannery B.P., Numerical Recipes. Cambridge Univ. Press, Cambridge, (1992)

[140] RiessA.G., FilippenkoA.V., ChallisP., ClocchiattiA., DiercksA., GarnavichP.M. et al. ApJ **116**, 1009 (1998)

[141] Sales L., Lambas D.G., MNRAS **348**, 1236 (2004)

[142] Sand D. J., Treu T., Smith G. P., Ellis R. S., `astro-ph/0310703`

[143] Schechter P.L. Wambsganss J., ApJ **580**, 685 (2002)

[144] Scholz R.-D., Irwin M.J., in IAU 161, *Wide Field Imaging*, eds. H.T. MacGillivray, (1994)

[145] Solanes J. M., Manrique A., Garcia-Gomez C., Gonzalez-Casado G., Giovanelli R., Haynes M. P., ApJ **548**, 97 (2001)

[146] Spergel D.N., Steinhardt P.J., Phys. Rev. Lett. **84**, 3760 (2000)

[147] Spergel D.N., Verde L., Peiris H.V., Komatsu E., Nolta M.R., Bennett C.L., Halpern M., Hinshaw G., Jarosik N., Kogut A., Limon M., Meyer S.S., Page L., Tucker G.S., Weiland J.L., Wollack E., Wright E.L., ApJ Suppl. **148**, 175 (2003)

[148] Splinter R.J., Melott A.L., Linn A.M., Buck C., Tinker J., ApJ **479**, 632 (1997)

[149] Springel V., White S.D.M., Tormen G., Kauffmann G., MNRAS **328**, 726 (2001)

[150] Somerville R., ApJ **572**, 23 (2002)

[151] StomporR., et al. ApJ **561**, 7 (2001)

[152] StraussM.A., WillickJ.A., Phys. Rev. **D261**, 271 (1995)

[153] Suginohara T., Suto Y., ApJ **396**, 395 (1992)

[154] Suisalu S., Saar E., MNRAS **274**, 287 (1995)

[155] Summers F., Davis M., Evrard A., ApJ **454**, 1 (1995)

[156] Suto Y., Cen R., Ostriker J., ApJ **395**, 1 (1992)

[157] Taffoni G., Mayer L., Colpi M., Governato F., MNRAS **341**, 434 (2003)

[158] Taylor J. E., Silk J., Babul A., `astro-ph/0312086`

[159] Thomas P. A. et al. MNRAS **296**, 1061 (1998)

[160] Tormen G., MNRAS **290**, 411 (1997)

[161] Tormen G., Bouchet F., White S., MNRAS **286**, 865 (1997)

[162] Tormen G., Diaferio A., Syer D., MNRAS **299**, 728 (1998)

[163] Trentham N., Mobasher B., MNRAS **293**, 53 (1998)

[164] Treu T., Ellis R., Kneib J., Dressler A., Smail I., Czoske O., ApJ **591**, 53 (2003)

[165] Tsuchiya T., Shimada M., ApJ **532**, 294 (2000)

[166] Tully B., Somerville R., Trentham N., Verheijen M., ApJ **569**, 573 (2002)

[167] van den Bosch F.C., Abel T., Crofts R.A., Hernquist L., Simon D.M., ApJ **576**, 21 (2002)

[168] van Kampen E., MNRAS **273**, 295 (1995)

[169] Villumsen J., V., ApJ Suppl. **71**, 407 (1989)

[170] Vollmer B., Braine J., Balkowski C., Cayatte V., Duschl W.J., A&A **374**, 824 (2001)

[171] Warren M.S., Quinn P.J., Salmon J.K., Zurek W.H., ApJ **399**, 405 (1992)

[172] Weinberg D., Hernquist L., Katz N., ApJ **477**, 8 (1997)

[173] West M.J., Jones C., Forman W., ApJ Lett. **451**, 5 (1995)

[174] West M.J., Blakeslee J.P., ApJ Lett. **543**, 27 (2000)

[175] White S.D.M., Rees M. MNRAS **183**, 341 (1978)

[176] WhiteS.D.M., NavarroJ.F., EvrardA.E., FrenkC.S., Nature **366**, 429 (1993)

[177] Yanny B., Newberg H.J., Grebel E.K., Kent S., Odenkirchen M. et al. ApJ **588**, 823 (2003)

[178] York D.G., et al. Astron. J. **120**, 1579 (2000)

[179] Yoshizawa A.M., Noguchi M., MNRAS **339**, 1135 (2003)

[180] Zaritsky D., Smith R., Frenk C.S., White S.D.M., ApJ **405**, 464 (1993)

[181] Zaritsky D., Smith R., Frenk C.S., White S.D.M., ApJ Lett. **478**, 53 (1997)

[182] Zaritsky D., Gonzalez A.H., PASP, **111**, 1508, (1999)

[183] ZaroubiS., ZehaviI., DekelA., HoffmanY., KolattT., ApJ **486**, 21 (1997)

[184] Zentner A.R., Kravtsov A.V., Gnedin O.Y., Klypin A.A., `astro-ph/0502496`

[185] Zhao H.S., Johnston K.V., Hernquist L., Spergel D.N., A&A **348**, L49 (1999)

Appendices

Appendix A

Circularity

We wish to establish a correlation between the circularity and eccentricity

$$\lambda = \frac{J_{\rm sat}(E)}{J_{\rm circ}(E)} \ , \tag{A.1}$$

where $J_{\rm sat}(E)$ measures the angular momentum of an individual satellite with total energy E. $J_{\rm circ}(E)$ is the corresponding angular momentum for a circular orbit with the same energy E.

The connection needs to be derived using the fact that both orbits share the same total energy, so we wish to express E as a function of J in both cases, where the general expression for E and J reads:

$$\begin{aligned} E &= \tfrac{1}{2}v^2 - \tfrac{GM}{r} \\ J &= |\vec{r} \times \vec{v}| \end{aligned} \tag{A.2}$$

Circular Orbits

For a circular orbit we know that $|\vec{r} \times \vec{v}|$ reduces to

$$J_{\rm circ} = r v_{\rm circ} \tag{A.3}$$

as both vectors are always orthogonal. Moreover, the circular velocity is given by

$$v_{\rm circ}^2 = \frac{GM}{r} \tag{A.4}$$

where M is the total mass of the host halo (assumed to be a point mass).

Combining this knowledge with Eq. (A.2) we arrive at

$$J_{\text{circ}} = GM\frac{1}{\sqrt{-2E}} \tag{A.5}$$

Keplerian Orbits

For Keplerian orbits the situation is a little more complicated. We know that the solution in spherical coordinates for closed orbits looks like

$$r = \frac{J_{\text{sat}}^2}{GM(1-\epsilon\cos\phi)}\ , \tag{A.6}$$

where ϵ is the measure for ellipticity of the orbit as given by

$$\epsilon = f/a \tag{A.7}$$

Here f is the focal length and a the major axis of the ellipse. Geometry relates ϵ to our eccentricity e as follows

$$\epsilon = \frac{2}{2-e}\ . \tag{A.8}$$

We still need an expression for the velocity which can be derived by using the first derivative of $\vec{r}$ with respect to time

$$\frac{d\vec{r}}{dt} = \frac{d(r\vec{e}_r(\phi))}{dt} = \dot{r}\vec{e}_r + r\dot{\phi}\vec{e}_\phi = \dot{r}\vec{e}_r + \frac{J_{\text{sat}}}{r}\vec{e}_\phi \tag{A.9}$$

Evaluating $\dot{r}$ and rearranging terms gives

$$v^2 = \frac{J_{\text{sat}}^2}{r^2}\frac{1-2\epsilon\cos\phi+e^2}{(1-\epsilon\cos\phi)^2} \tag{A.10}$$

Inserting this knowledge into Eq. (A.2) again leads to

$$E = \left(\frac{GM}{J_{\text{sat}}}\right)^2\frac{\epsilon^2-1}{2}\ . \tag{A.11}$$

The Relation

We know have everything necessary to write the sought-after relation between eccentricity ϵ and circularity λ; we simply need to combine Eq. (A.6) and Eq. (A.11), keeping Eq. (A.8) in mind:

$$\begin{aligned} \epsilon &= \frac{2}{2-e} \\ \lambda &= \sqrt{1-\epsilon^2} \end{aligned} \tag{A.12}$$

This relation is plotted as a solid line in Figure 4.13.

Publications

Refereed publications

[1] A. Knebe, **S.P.D. Gill**, D. Kawata, B.K. Gibson
Mapping substructure in Dark Matter Halos
Mon. Not. R. Astron. Soc. **357**, L35 (2005)

[2] **S.P.D. Gill**, A. Knebe, B.K. Gibson
The evolution of substructure III: the outskirts of clusters
Mon. Not. R. Astron. Soc. **356**, 1327 (2005)

[3] **S.P.D. Gill**, A. Knebe, B.K. Gibson
The dynamics of cluster substructure
IAU Conference Proceedings 195, **280**, (2004)

[4] A. Knebe, **S.P.D. Gill**, B.K. Gibson
Interactions of Satellite Galaxies in Cosmological Dark Matter Halos
PASA - GCDV conference proceedings **21**, 216 (2004)

[5] **S.P.D. Gill**, A. Knebe, B.K. Gibson, M. Dopita
The evolution of substructure II: linking the dynamics to environment
Mon. Not. R. Astron. Soc. **351**, 410 (2004)

[6] **S.P.D. Gill**, A. Knebe, B.K. Gibson
The evolution of substructure I: finding the substructure
Mon. Not. R. Astron. Soc. **351**, 399 (2004)

[7] A. Knebe, **S.P.D. Gill**, B.K. Gibson, R. Ibata, G. Lewis
Anisotropy in satellite distribution
Astrophys. J. Letter **603**, 7 (2004)